

**In-Situ Research  
Work of GRS  
at the Mont Terri  
Rock Laboratory and  
Related Modelling**

**Experiments HE-E,  
FE-M, DM-A, SB-A,  
DB, MB-A, Virtus**

**In-Situ Research  
Work of GRS  
at the Mont Terri  
Rock Laboratory and  
Related Modelling**

Experiments HE-E,  
FE-M, DM-A, SB-A,  
DB, MB-A, Virtus

Klaus Wieczorek  
Oliver Czaikowski  
Larissa Friedenberg  
Kyra Jantschik  
Michael Komischke  
Michael Kröhn

March 2020

**Remark:**

This report refers to the research project 02E11304 which has been funded by the German Federal Ministry for Economic affairs and Energy (BMWi).

The work was conducted by the Gesellschaft für Anlagen- und Reaktorsicherheit (GRS) gGmbH.

The authors are responsible for the content of this report.

**Keywords:**

engineered barrier, in-situ testing, numerical simulation, Opalinus clay, THM behaviour

## Zusammenfassung

Im vorliegenden Bericht werden die In-situ-Forschungsarbeit der GRS im Felslabor Mont Terri (MTRL) und die damit verbundenen Modellrechnungen im Zeitraum zwischen 2014 und 2019 dargestellt. Die Arbeiten beinhalten die Teilnahme an großmaßstäblichen Simulationsexperimenten wie dem HE-E und dem FE Experiment, aber auch die Untersuchungen zum hydromechanischen Verhalten (DM-A, SB-A und MB-A Experiment) und zur Charakterisierung des Opalinustons (DB Experiment).

HE-E und FE wurden bereits vor dem Berichtszeitraum gestartet und haben bereits eine große Menge zuverlässiger Daten produziert. Sie laufen weiterhin ohne größere Probleme, und trotz ihrer langen Dauer ist der Ausfall von Messsensoren begrenzt.

Problematisch ist beim HE-E (Erhitzerexperiment im 1:2 Maßstab) der sehr geringe Porenwasserdruck im umgebenden Gebirge, der dazu führt, dass im Inneren des bentonithaltigen Buffers bisher keine signifikante Aufsättigung durch Porenwasser aus dem Opalinuston festgestellt werden kann – stattdessen nahm die Sättigung im Buffer durch Verdampfung ab. Da sich die Porendruck-Situation nicht verändern wird, kann in den kommenden Jahren nicht mit einer Änderung des Sättigungszustandes des Buffers gerechnet werden. Daher müssen die Experimentpartner entscheiden, ob das Experiment beendet werden soll und welche Nachuntersuchungen mit welchen Zielen ggf. durchzuführen sind. Diese Entscheidung braucht einige Vorbereitung und ist für 2020 geplant.

Das FE Experiment wurde in einem neu aufgefahrenen Tunnel in einem ungestörten Bereich des Opalinustons mit ursprünglicher Porendruckverteilung aufgebaut. Wegen seines realistischen Maßstabs (die 1:1 Umsetzung eines Einlagerungstunnels nach dem Schweizer Entsorgungskonzept) ist die Bufferaufsättigung allerdings ebenfalls langsam. Porendruckmessungen im umgebenden Opalinuston zeigen abhängig vom Messort den nahezu ungestörten Druck fern vom FE-Tunnel, den gemäßigten beeinflussten Druck in der Umgebung des mit Spritzbeton ausgekleideten Tunnelbereichs und den stark gestörten Druck, wo in der Tunnelumgebung ein Stahlringausbau ohne Spritzbeton eine weitergehende Entwicklung von Gebirgsschädigung ermöglichte.

Beide großmaßstäblichen Experimente erfordern Modellsimulationen zu ihrer Interpretation. Verschiedene Modellierungsgruppen haben solche bereits durchgeführt. Allerdings fehlt bisher eine realistische Simulation, die die tatsächliche komplizierte Geometrie der Versuche abbildet. GRS nähert sich dieser Aufgabe mit der Hilfe von Virtus, dem virtuel-

len Untertagelabor. Erste orientierende Modellrechnungen wurden durchgeführt, und obwohl numerische Herausforderungen bestehen, wird ein weiterer Fortschritt erwartet. Das FE Experiment soll im Rahmen eines Decovalex Tasks simuliert werden, an dem GRS teilnehmen wird.

Das DB Experiment (Kernbohrung durch die gesamte Opalinuston-Formation) hat eine große Menge von Daten zum ungestörten Opalinuston geliefert, die sowohl in sich selbst wertvoll sind, als dass sie auch Anfangs- und Randbedingungen für Modellrechnungen liefern. Es wurden repräsentative petrophysikalische Daten sowie Temperatur- und Druckprofile der ganzen Formation ermittelt, die frühere Annahmen bestätigt haben.

Das hydromechanische Verhalten des Opalinustons wurde in den Experimenten DM-A, SB-A und MB-A untersucht. Bei DM-A wird das Langzeit-Deformationsverhalten beobachtet, und es wurde gezeigt, dass Porendruckänderungen im Gebirge nur eine untergeordnete Rolle bei der Langzeitverformung spielen. Ob tatsächliches Kriechen, also viskoses Verhalten, relevant ist oder nicht, konnte noch nicht zweifelsfrei ermittelt werden.

Das MB-A Experiment war ein Mine-by-Versuch, das einen wertvollen Datensatz zum hydromechanischen Verhalten der sandigen Fazies des Opalinustons geliefert hat. Dazu gehören Daten zur Spannungsentwicklung, zur Verformung und zur Porendruckentwicklung. Für die Interpretation dieses Versuchs sind ebenfalls Modellrechnungen erforderlich. Ein entsprechendes Experiment, die Simulation des MB-A, ist von den Partnern geplant und soll 2020 beginnen.

## Table of contents

<b>1</b>	<b>Introduction .....</b>	<b>1</b>
<b>2</b>	<b>Processes in a nuclear waste repository in claystone .....</b>	<b>3</b>
<b>3</b>	<b>Mont Terri Rock Laboratory .....</b>	<b>7</b>
<b>4</b>	<b>Overview of experiments .....</b>	<b>11</b>
<b>5</b>	<b>In-situ measurements .....</b>	<b>13</b>
5.1	Pore-water pressure measurement .....	13
5.2	Experiments in detail .....	16
5.2.1	HE-E .....	16
5.2.2	FE-M .....	27
5.2.3	DM-A .....	35
5.2.4	SB-A .....	39
5.2.5	DB .....	41
5.2.6	MB-A .....	48
<b>6</b>	<b>Model simulation .....</b>	<b>57</b>
6.1	Virtus adaptation .....	57
6.2	HE-E simulation .....	61
6.2.1	Geometrical model .....	62
6.2.2	Physical model .....	64
6.2.3	Material data and initial parameters .....	65
6.2.4	Schedule and boundary conditions .....	67
6.2.5	Results .....	68
6.3	FE-M modelling .....	71

<b>7</b>	<b>Conclusions and future work .....</b>	<b>75</b>
<b>8</b>	<b>Acknowledgements.....</b>	<b>77</b>
	<b>References.....</b>	<b>79</b>
	<b>List of figures .....</b>	<b>85</b>
	<b>List of tables .....</b>	<b>91</b>

# 1 Introduction

Operation of nuclear power plants creates heat-generating radioactive waste which, according to international consensus /OEC 08/ and to the concepts most countries using nuclear power are developing, should be disposed of in deep geological formations. In different countries, different host rocks are considered owing to their respective geological situations. In Germany, a decision on the host rock has not yet been taken – rock salt, claystone, and crystalline rocks are under investigation.

The overall objective of nuclear waste disposal in geological formations is to ensure permanent containment of the waste, concentrating and isolating it for very long time from the biosphere. Claystone has a very low permeability, and water pathways are naturally closed by plastic deformation and swelling. Although claystone in its natural state is water-saturated, transport processes are dominated by very slow diffusion processes. This makes claystone a candidate host rock for a repository, and several European countries (e. g., France, Switzerland, Belgium) have developed repository concepts in a clay environment.

In Germany, a safety concept for a repository in claystone has been developed in a joint project of the Bundesanstalt für Geowissenschaften und Rohstoffe (BGR), the DBE TECHNOLOGY GmbH and the GRS /RUE 14/. Among others, integrity criteria for the clay rock had to be concretized, since the safety case requires a statement on long-term integrity of the geological and engineered barriers /BMU 10/.

For constructing a repository and for ensuring that the safety criteria are met over very long time periods, profound knowledge about the material behaviour of the coupled system of waste containers, engineered barriers (EBS), and the rock is indispensable. In addition to theoretical and laboratory-scale work, some countries run underground research laboratories (URLs) in order to obtain this knowledge, following the guidelines of OECD-NEA /OEC 01/.

The Mont Terri Rock Laboratory (MTRL) is a unique facility where repository research is performed in a clay rock environment. It is run by an international consortium which GRS is a member of, with the motivation of

- Gaining profound understanding of the safety-relevant coupled thermal-hydraulic-mechanical (THM) processes running in a repository in clay rock,

- Developing appropriate process models which are needed for long-term prediction of the system evolution, by comparison of simulation results with representative laboratory and in-situ experiments,
- Obtaining reliable data for qualification of process models (including development and improvement of measuring techniques),
- Gaining knowledge by international co-operation,
- Know-how transfer to German clay formations.

The Opalinus clay at the MTRL is of special interest for Germany, since potential German host formations are either the southern German Opalinus clay or northern German lower cretaceous clays which, when compared to claystones accessible in underground laboratories, seem to be closest to the sandy facies of the Opalinus clay /HOT 07/.

This report summarizes the GRS in-situ work at the MTRL and related model simulations performed in the frame of various experiments between July 2014 and June 2019. Additional extensive laboratory work addressing the sandy facies of the Opalinus clay is presented in a separate report /ZHA 19/. Some of the in-situ experiments were started before 2014 and intermediate results have been published earlier /WIE 14a, ZHA 14/. Some will also continue in the future. For these this report describes an interim state.

## 2 Processes in a nuclear waste repository in claystone

In addition to the geological barrier, engineered barriers are required in a repository in order to account for the disturbance introduced by mining and waste emplacement. Repository concepts have to include provisions to emplace the waste containers, back-fill remaining voids and seal galleries and shafts.

Many concepts involve a clay-bearing “buffer” which surrounds the waste containers and fills the void between them and the host rock. The buffer generally consists of bentonite or bentonite-bearing material and is re-saturated over time by water from the host rock. This results in an increasing swelling pressure and thermal conductivity and decreasing hydraulic conductivity. Thus, the buffer provides containment of the waste, limits advective flow, and enables heat dissipation into the rock. It also provides chemical buffering and long-term retardation of radionuclides.

Figure 2.1 shows the Swiss repository concept as an example. The waste containers are placed on highly compacted bentonite blocks in horizontal galleries, and the remaining voids are filled with granular bentonite buffer material.

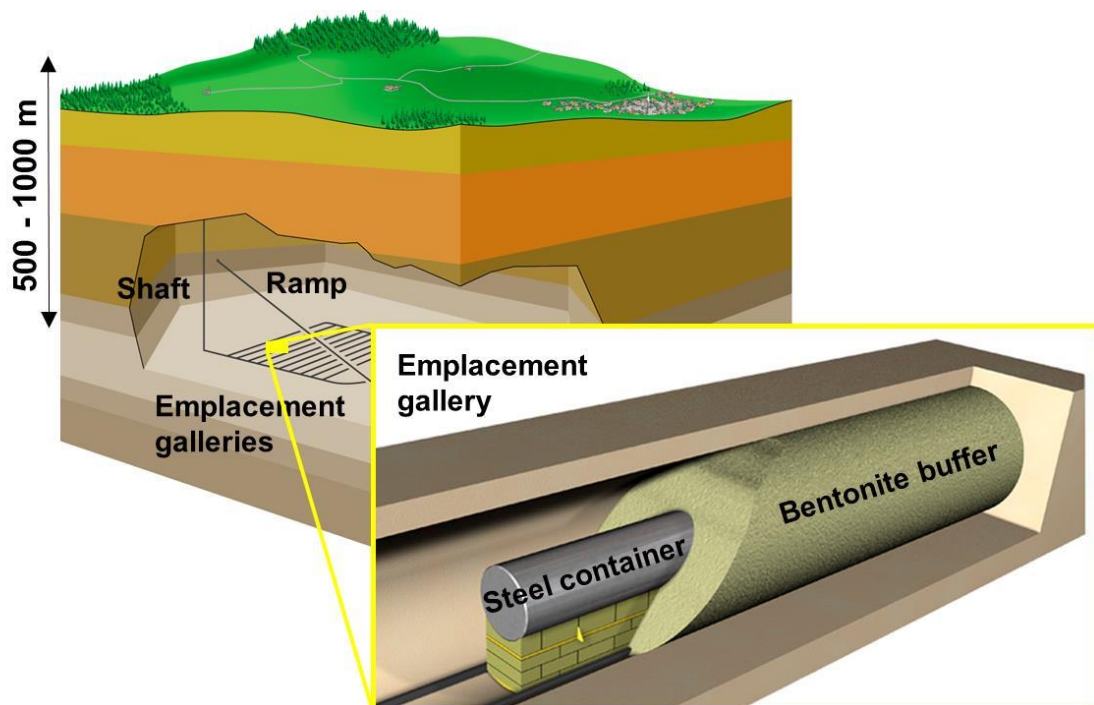


**Fig. 2.1** The Swiss repository concept for clay rock /JAE 11/

In Germany, both horizontal disposal in galleries and waste emplacement in vertical boreholes drilled from access galleries are considered as possibilities. Both concepts will also involve bentonite-bearing buffer.

Many physicochemical processes which affect system evolution will run in a repository during the phases of excavation, waste emplacement, and post-closure. These can be divided into mechanical, hydraulic, thermal, chemical and possibly biological (microbial) processes which are generally coupled among one another. Figure 2.2 gives an overview of the most important processes and the phase in which they are relevant.

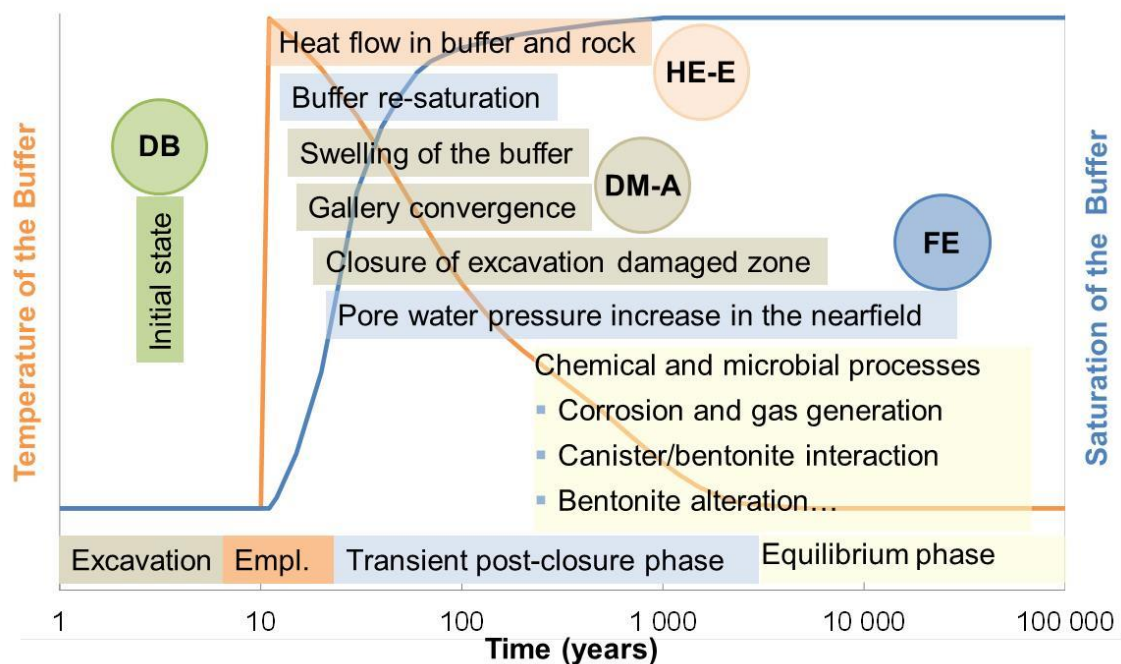


**Fig. 2.2** Processes in a repository in clay (red: thermal, blue: hydraulic, grey: mechanical, yellow: chemical/biological). DB, HE-E, DM-A, FE: selected Mont Terri experiments addressing different processes

During excavation, the mechanical state of the rock is changed, an excavation-damaged zone (EDZ) evolves, and ventilation of the openings may lead to desaturation of the adjacent rock. Emplacement leads to substantial temperature increase in the nearfield of the waste, resulting in an increase in pore water pressure due to thermal strain. During the transient post-closure phase, temperature gradually decreases, while the buffer is re-saturated by pore water from the surrounding rock which leads to swelling of the bentonite. Buffer swelling and gallery convergence driven by the rock stress lead to re-compaction and closure of the EDZ.

When, after a few thousand years, the thermal pulse has passed and the pore pressure in the system has equilibrated, there are practically no more driving forces for thermal-hydraulic-mechanical processes. Chemical and microbial processes however, like corrosion and related gas generation, chemical interaction between steel containers and buffer, and alteration processes in the bentonite, will remain active.

All the phases of repository evolution and the related coupled processes relevant in each phase are addressed by experiments performed by differently grouped partners at the MTRL.



### 3 Mont Terri Rock Laboratory

The Mont Terri Rock Laboratory /MON 20/ is situated in the north-western part of Switzerland in the Kanton of Jura, where it has been excavated parallel to the security gallery of the Mont Terri motorway tunnel on the south-western slope of the Mont Terri anticline (Figures 3.1 and 3.2). It is run by a consortium of 21 international partners under the directorate of the Swiss geological survey (Swisstopo). The partners are Swisstopo, Nagra, ENSI, ETH (Switzerland), ANDRA, IRSN, Total (France), BGR, GRS, Helmholtz, BASE (Germany), SCK-CEN, FANC (Belgium), Enresa (Spain), RWM (UK), JAEA, CRIEPI, Obayashi (Japan), NWMO (Canada), DOE and CHEVRON (USA). GRS has performed experimental work at the MTRL since 1998.

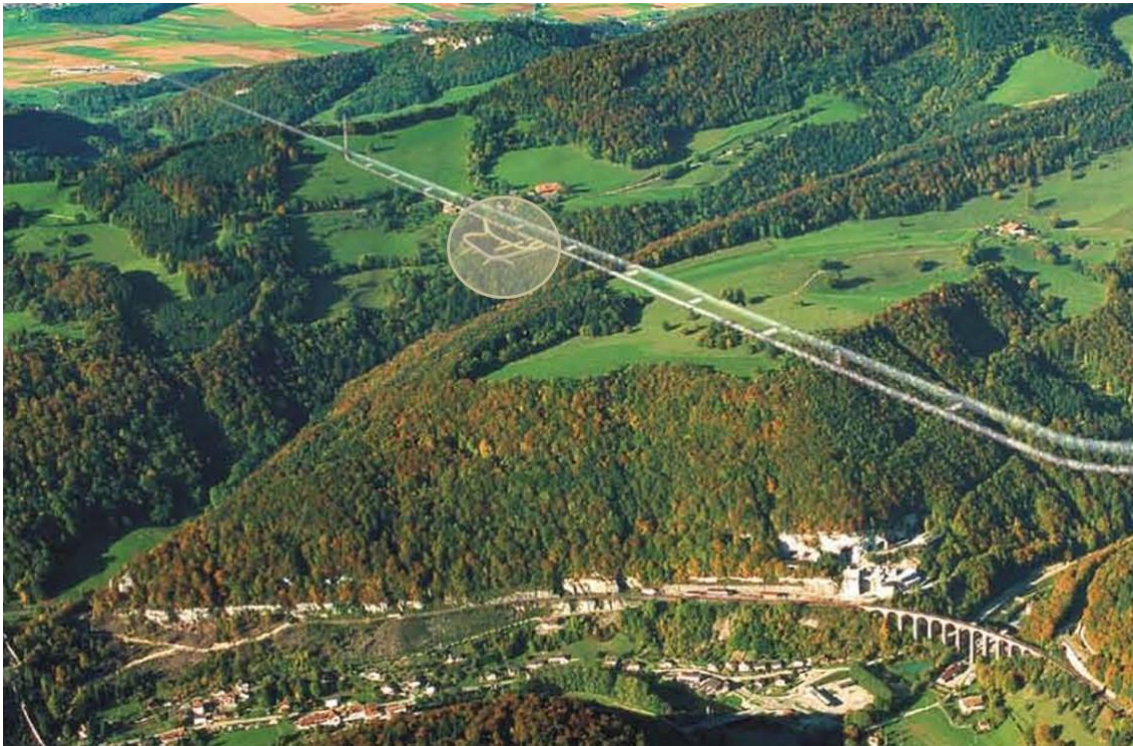


**Fig. 3.1** The Mont Terri Rock Laboratory in the Swiss Jura

The MTRL is located in the Opalinus clay formation consisting of three main facies: the sandy facies, the shaly facies, and the sandy carbonate-rich facies (Fig. 3.3). The bedding planes plunge towards the south-east with an azimuth of  $140^{\circ} - 150^{\circ}$  (Fig. 3.4). The apparent thickness of the Opalinus clay is about 160 m. Its current overlay varies between 250 and 320 m, while it is estimated to have reached at least 1000 m in the past. The clay rock is saturated with water, but water circulations are practically negligible due to its very low permeability and pressure gradient.

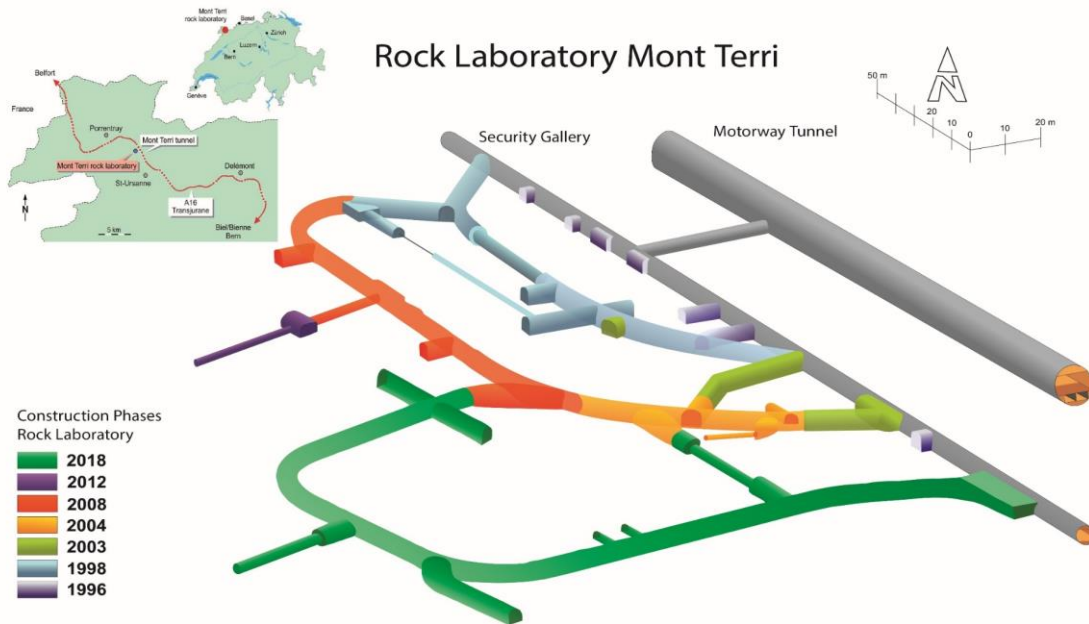


**Fig. 3.2** The MTRL tunnel system. Different colours of the tunnel system mark the respective year of excavation

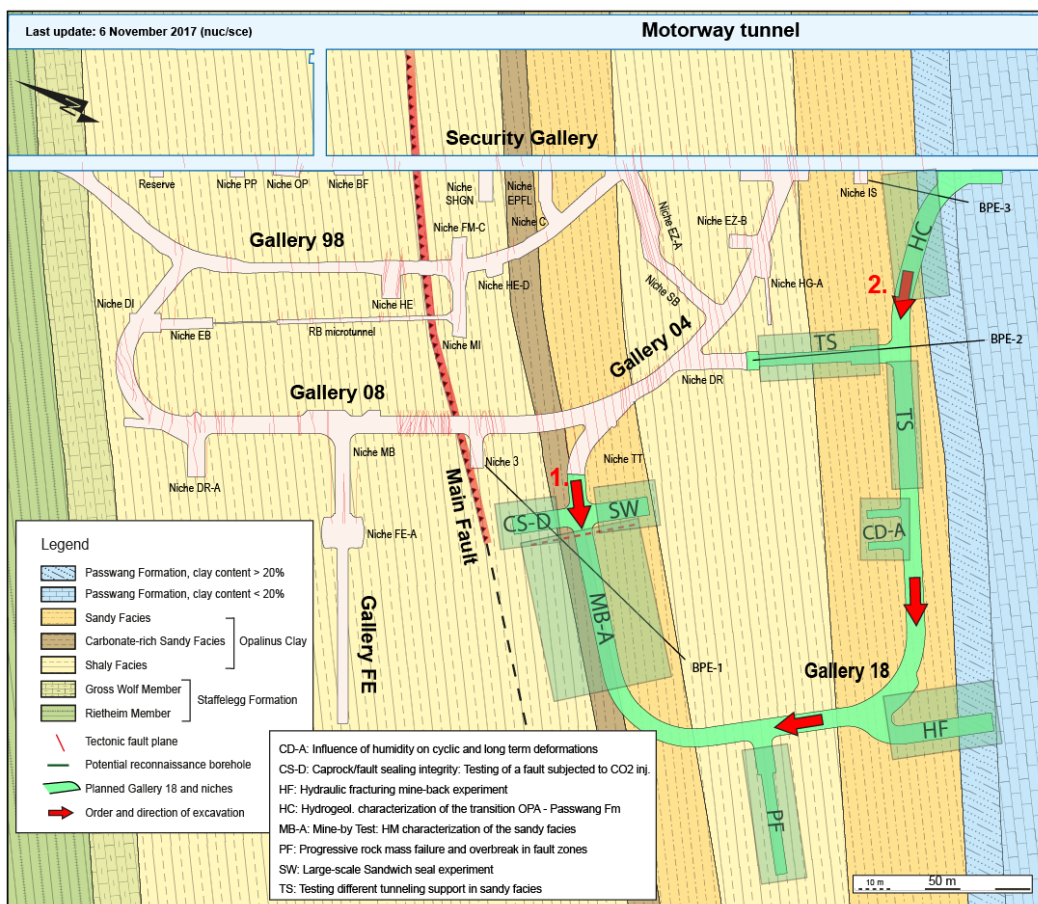


**Fig. 3.3** Plan view of the Mont Terri rock laboratory showing the geology (green: recently excavated lab extension with the locations of new experiments)

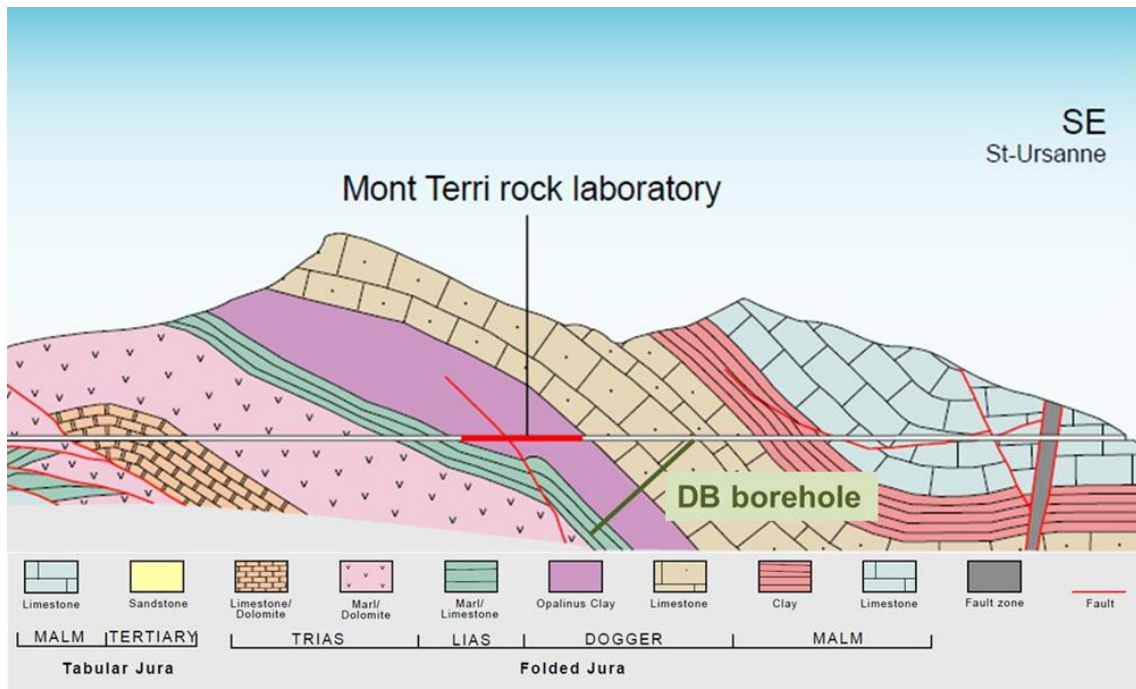


**Fig. 3.4** Geological section along the Mont Terri motorway tunnel showing the location of the rock laboratory (DB borehole: see Section 5.2.5)

More information on the MTRL is given in /BOS 17/ and on the Mont Terri website /MON 20/.



## 4 Overview of experiments

GRS' involvement in the MTRL focuses on the thermo-hydro-mechanical (THM) behaviour of the Opalinus clay or of the combined system of clay and engineered barrier. The locations of the experiments reported here are shown in Fig. 4.1. The experiments are presented in detail in Section 5.2. Specific measurement methods, especially pore-water pressure measurement using GRS' in-house developed minipiezometers, are used in several of the experiments (Section 5.1).

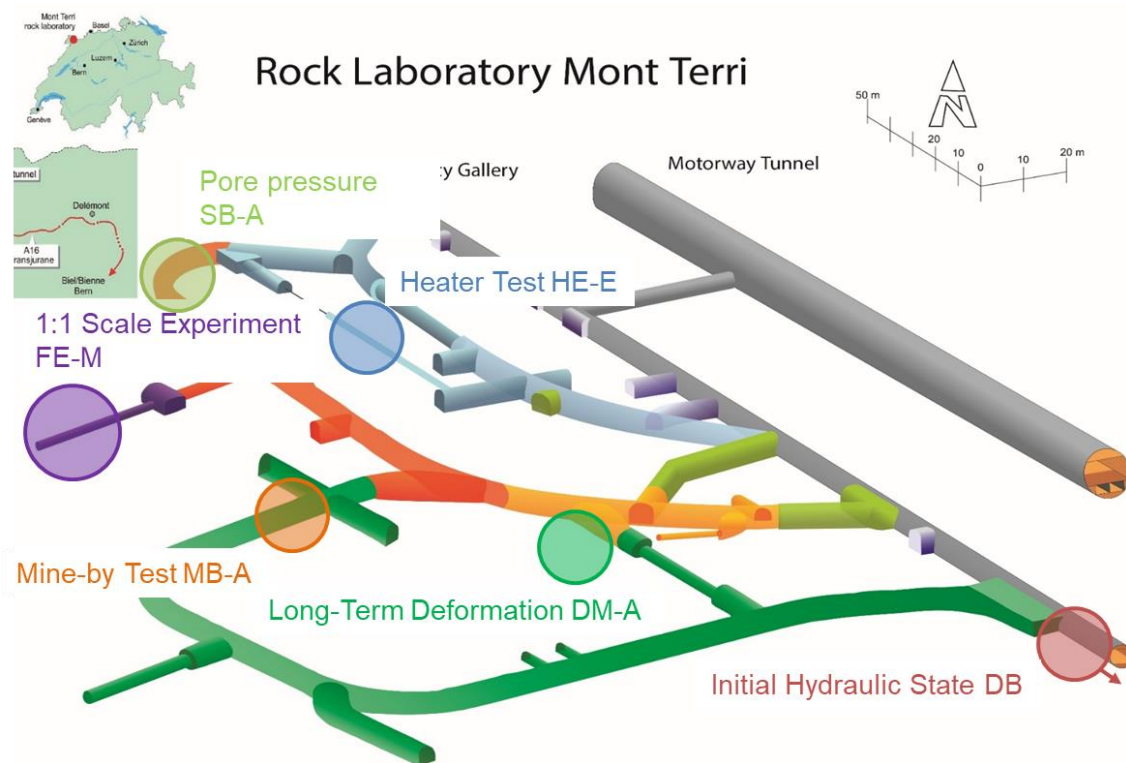


**Fig. 4.1** Experiment locations HE-E, FE-M, DM-A, SB-A, DB, and MB-A

The **HE-E** heater experiment was started in 2011 as part of the 7<sup>th</sup> Framework EURATOM project “Long-term Performance of Engineered Barrier Systems” (PEBS). The main objective of the HE-E is to gain insight in the early non-isothermal re-saturation period of the buffer and its impact on the THM behaviour. It has been the first near real-scale in-situ experiment involving granular buffer at high temperature.

In 2012, Nagra together with some of the Mont Terri partners including GRS started construction of an emplacement experiment following the Swiss concept at 1:1 scale, involving a realistic temperature evolution and natural buffer re-saturation. The objective of the experiment is to study the THM-coupled processes in the clay rock and buff-

er induced by waste emplacement. The monitoring part of this experiment, in which GRS is involved with the study of pore pressure evolution in the Opalinus clay, is abbreviated **FE-M**.

The **DM-A** experiment performed by GRS addresses long-term deformation mechanisms of the clay rock. In the frame of this experiment, a borehole dilatometer probe measures deformation in a horizontal borehole since June 2009. Additional measurements comprise temperature, humidity, and pore pressure in the rock.

In BGR's **SB-A** experiment on borehole sealing performance and stability of sealing material and methods, GRS participated with pore pressure measurements around a borehole.

The **DB** experiment addressed the initial (undisturbed) hydraulic state of the rock. A 250 m long inclined borehole was drilled through the Opalinus clay and the neighbouring formations from outside the laboratory. Samples were taken and the borehole was equipped with a multi-point probe for hydraulic conductivity and pore pressure measurement.

While a wide database on the hydraulic and mechanical (short-term) behaviour is available for the shaly facies, characterization of the sandy facies is less advanced. In the **MB-A** experiment performed by BGR, GRS, and Swisstopo, the rock mass response to excavation of Gallery 18 in the sandy facies and the sandy carbonate-rich facies was investigated (Fig. 2.3).

A part of GRS' work in the frame of the Mont Terri project was not connected to in-situ experimentation. The virtual underground laboratory **Virtus** which had been developed for a URL in rock salt was adapted for use with the MTRL.

GRS is also involved in an experiment that concentrates on laboratory investigations of the sandy facies of the Opalinus clay (LT-A) which is not presented here, but in a separate report /ZHA 19/.

## **5 In-situ measurements**

The first section of this chapter describes the GRS minipiezometers used for pore-water pressure measurements in nearly all the experiments reported here. In the second section the various experiments are described in detail.

### **5.1 Pore-water pressure measurement**

The fluid pressure inside the undisturbed pore space of the Opalinus clay can be quite different from the theoretical hydraulic head (e.g., due to osmosis, diffusional or mechanical processes). The pore-water pressure is highly important for the hydro-mechanical behaviour of the rock, but also for the re-saturation of areas bordering excavations, which can be de-saturated due to the excavation process and to ventilation. It is also important for the re-saturation of clay-bearing backfill and sealing materials. Therefore, pore pressure measurements are performed in all experiments where the hydro-mechanical behavior of the claystone is involved.

Conventional pore pressure measurements involve multi-packer probes installed in boreholes. The sealing elements (pressurized rubber cylinders) seal off test intervals inside the borehole which are filled with (possibly artificial) pore-water. With time the pressure measured in the interval equilibrates with the surrounding pore pressure.

The conventional method has several drawbacks: Drilling of the packer boreholes disturbs the pore pressure field in the vicinity, not only as a consequence of the mechanical load change, but also due to air flushing. The disturbance is related to the borehole diameter – large diameter boreholes cause large disturbance. A second drawback is the fact that packer pressure needs to be considerably higher than the pore pressure to be measured, in order to avoid packer bypass flow. The packer probe therefore influences the pressure field itself.

To reduce these effects as much as possible, GRS has developed a minipiezometer system which is installed in small-diameter boreholes (typically 20 mm) and dispenses with active pressurization.

The system is made up of the following components:

- A single mechanical minipacker with a crown head to be installed at the bottom of a small-diameter borehole (Fig. 5.1)
- A coaxial double tubing of stainless steel (outer tube) and polyamide (inner tube) to connect the test interval at the borehole bottom with the transducer rack outside the borehole (Fig. 5.2, left)
- A rack with valves, pressure gauge, and pressure transducer to which the tubes are connected (Fig. 5.2, right)

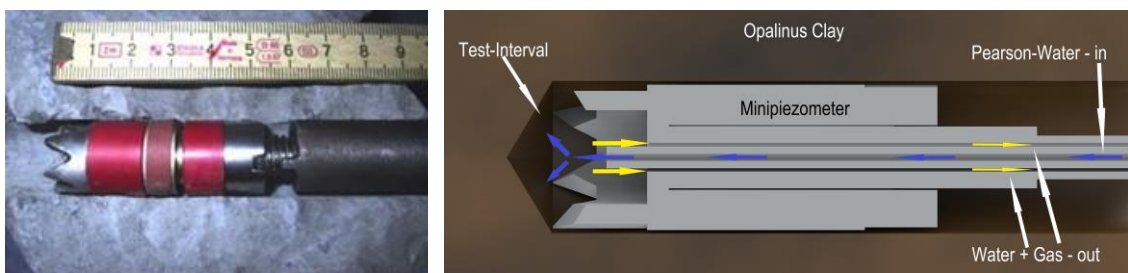


**Fig. 5.1** GRS minipiezometer – photo (left) and sketch (right)

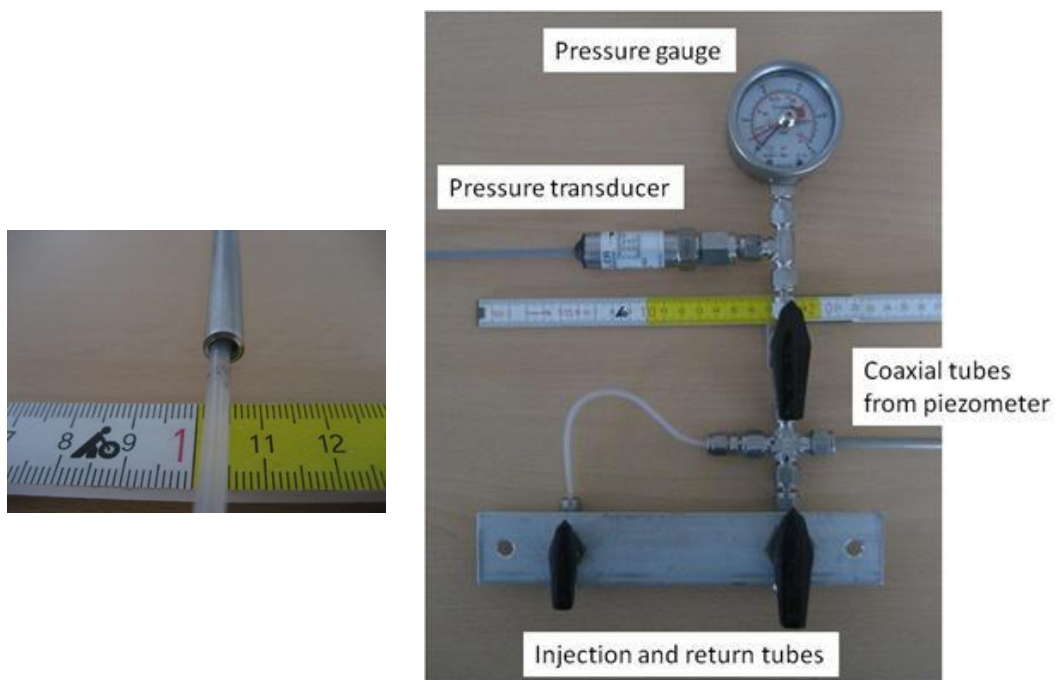


**Fig. 5.2** Coaxial tubing (left) and transducer rack (right)

For installation the minipiezometer probe is pushed into the borehole until the teeth at the front end reach the borehole bottom. The setting tool (right side in the photo of

Fig. 5.1) is then used to load the rubber packer (red in the photo) so that good contact between the borehole wall and the packer is reached. Afterwards the setting tool is removed and all the void of the borehole above the packer is filled with synthetic resin for sealing.

The test interval at the borehole bottom is connected to the transducer rack via the coaxial double tubing allowing for injection and extraction of fluids. After installation, the test interval is flushed with synthetic pore-water (Pearson water) and then pressurized to a low overpressure. With time, the pressure in the test interval equilibrates with the surrounding pore pressure.

The advantages of the minipiezometer system are

- The small borehole diameter reducing the influence of drilling
- No active pressurization of sealing elements
- Sealing of the complete remaining borehole, which avoids pore pressure loss
- Low cost

The system was originally developed for use in crystalline rock at Äspö. It was first used in Opalinus clay at the MTRL in 2002 /KUL 02/. Since then, it has been successfully used in many experiments /ZHA 07, MIE 10, ZHA 14, WIE 14a/.

A drawback of the system is the fact that one borehole can only take one minipiezometer. Also, the borehole length is limited due to the installation procedure. Boreholes up to 15 m length are feasible and have been used. For such borehole lengths, however, the 20 mm drill rods are not stable enough. Therefore, longer boreholes are drilled in 42 mm diameter, and only the last 36 mm are drilled with 20 mm diameter. This facilitates drilling and installation while keeping the influence of drilling in the vicinity of the minipiezometer low.

The system described here was installed in the HE-E, FE-M, DM-A, SB-A, and MB-A experiments reported in the next section.

## 5.2 Experiments in detail

### 5.2.1 HE-E

The HE-E experiment was started in 2011 as part of the 7th Framework EURATOM project “Long-term Performance of Engineered Barrier Systems” (PEBS). The idea of PEBS was to evaluate the sealing and barrier performance of the EBS with time, through development of a comprehensive approach, involving experiments, model development, and consideration of the potential impact on safety functions /SCH 14/. The main objective of the HE-E was to gain insight in the early non-isothermal re-saturation period of the buffer and its impact on the THM behaviour. Particular objectives were to provide the experimental database required for the calibration and validation of existing thermo-hydro-mechanical models of the early re-saturation phase and to verify upscaling of the thermal conductivity of the partially saturated buffer from laboratory to field scale for two types of candidate buffer materials: pure bentonite and sand-bentonite mixture /GAU 14/. The HE-E experiment has been the first near-real scale in-situ experiment involving granular buffer at high temperature. Detailed information about the first years of the HE-E can be found in the following PEBS deliverables:

- Design and predictive modelling of the HE-E test (Deliverable D3.2-1) /CZA 12/
- Report on the construction of the HE-E experiment (Deliverable D2.2-3) /TEO 12/
- The HE-E Experiment: Lay-out, Interpretation and THM Modelling (the HE-E final report, Deliverable D2.2-11 and D3.2-2) /GAU 14/

An overview is also found in /WIE 14a/.

After completion of the PEBS project in 2014, the experiment partners Nagra, Enresa, BGR, and GRS decided to continue the HE-E experiment with national funding. In 2016, Obayashi joined in as a fifth partner.

### 5.2.1.1 Experiment design and construction

The experiment was set up in a microtunnel of 1.3 m diameter which had been used earlier for the Mont Terri ventilation experiment VE /MAY 07/. Until 2006, the VE experiment was performed in the micro-tunnel. Advantage could be taken of the extensive instrumentation of the VE section. Only a few additions were needed to complete rock instrumentation for the HE-E.

The location of the microtunnel in the Mont Terri rock laboratory is marked in Fig. 4.1. The HE-E experiment (Figs. 5.3 and 5.4) consists of two independently heated sections, each 4 metres long, separated by a concrete plug. Both sections are equipped with an electrical heater bedded on highly compacted bentonite blocks. The remaining void is backfilled with granular bentonite buffer (Section 1) or 65/35 sand/bentonite mixture (Section 2). Especially Section 1 represents Nagra's emplacement concept in a near 1:2 scale. The sand/bentonite mixture was chosen as an alternative potential buffer material after the experiences of the SB experiment /ROT 12/. In the HE-E experiment, the bentonite used for all buffer types was sodium bentonite (Wyoming bentonite).

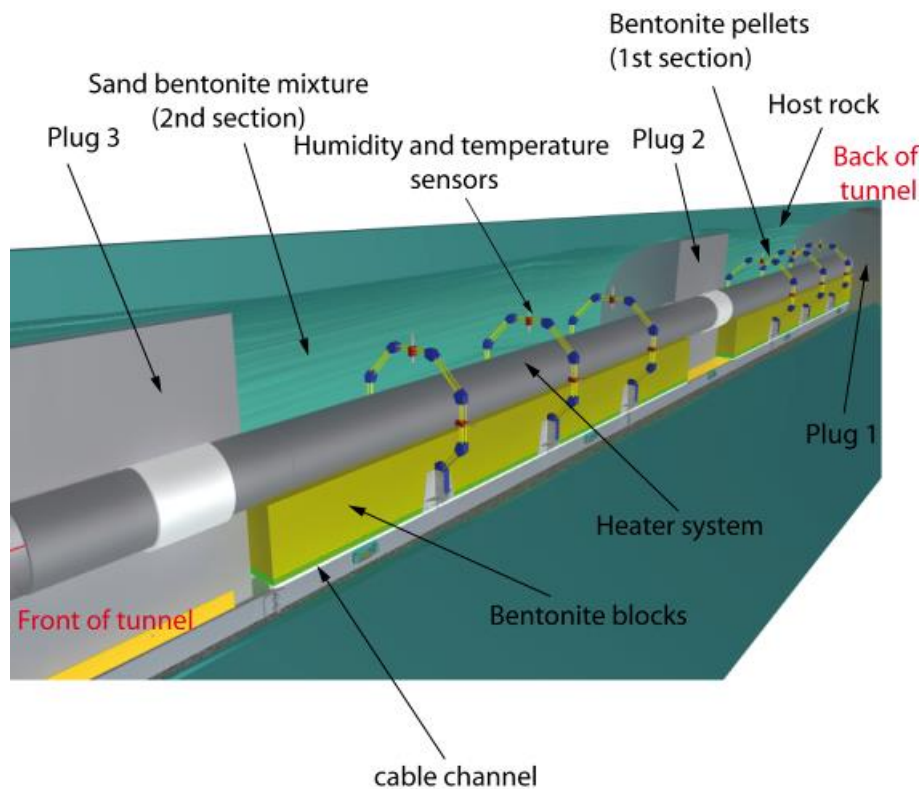


**Fig. 5.3** Overview of the HE-E experiment layout /TEO 12/

The Opalinus Clay around the microtunnel had already been instrumented for the VE experiment; sensors had been installed in different cross sections (Fig. 5.4): temperature and pore pressure sensors (SA and SD), temperature and humidity sensors (SB), and extensometers (SD). In 2010/11, the rock instrumentation was completed by additional temperature and pore pressure sensors (both minipiezometers installed from inside the microtunnel and multipacker probes) and a seismic array.

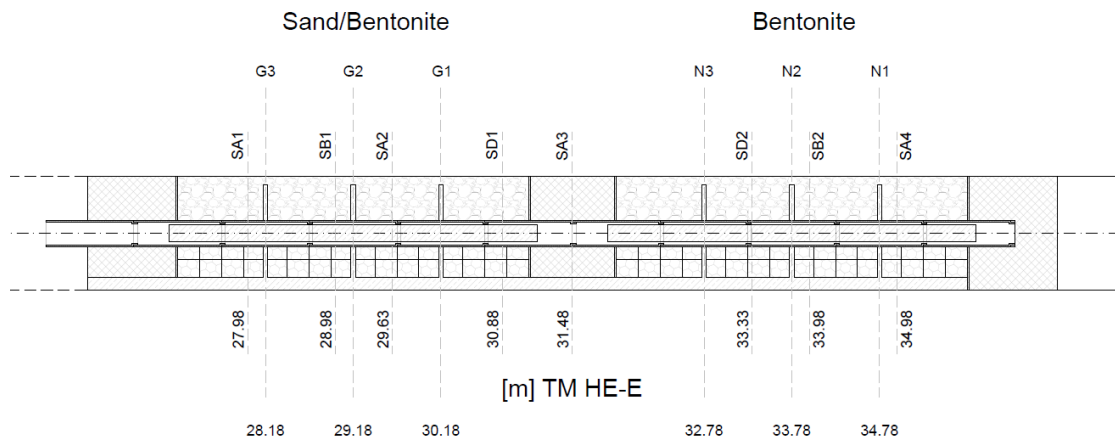


**Fig. 5.4** Longitudinal section of the microtunnel showing the instrumentation cross sections /GAU 14/. Sections SA, SB, SD denote rock instrumentation, sections N1–N3 and G1–G3 denote buffer instrumentation

The spatial restrictions of the microtunnel proved a challenge for the installation of heaters, buffer, and instrumentation. The solution was to construct a unit of bentonite block support, heater liner, and sensor carrier outside the microtunnel which was then inserted into the tunnel as one package (Fig. 5.5). The sensor carriers support temperature and humidity sensors at defined radial distances from the heater liner in six cross sections (Fig. 5.4). A total of 18 humidity/temperature sensors were emplaced at the tunnel wall and an additional 60 humidity/temperature sensors were emplaced within the sand/bentonite or bentonite section. The position of the sensors is shown in Figs. 5.5 and 5.6. The sensors closest to the heater (first layer) have a distance of 250 mm to the centre of the tube or 100 mm to the surface of the liner. The second layer of sensors has a distance of 400 mm to the centre or 250 mm to the liner surface. The third layer of sensors is attached to the wall; the distance to the centre varies with the roughness of the wall /GAU 14/.

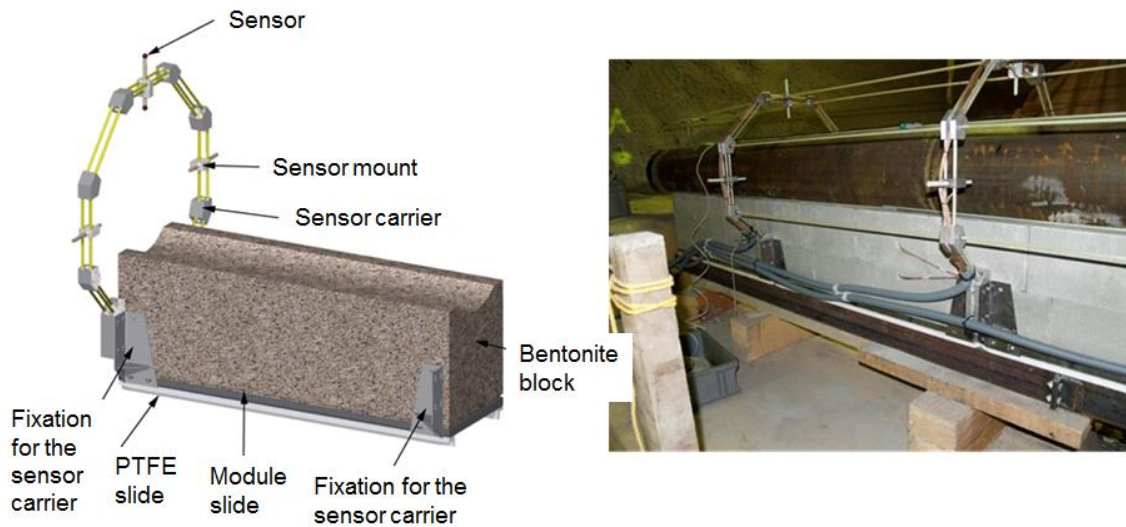


**Fig. 5.5** Integrated buffer installation and instrumentation. Left: design of a buffer instrumentation module, right: complete bentonite block/liner/sensor carrier module before insertion into the microtunnel /GAU 14/

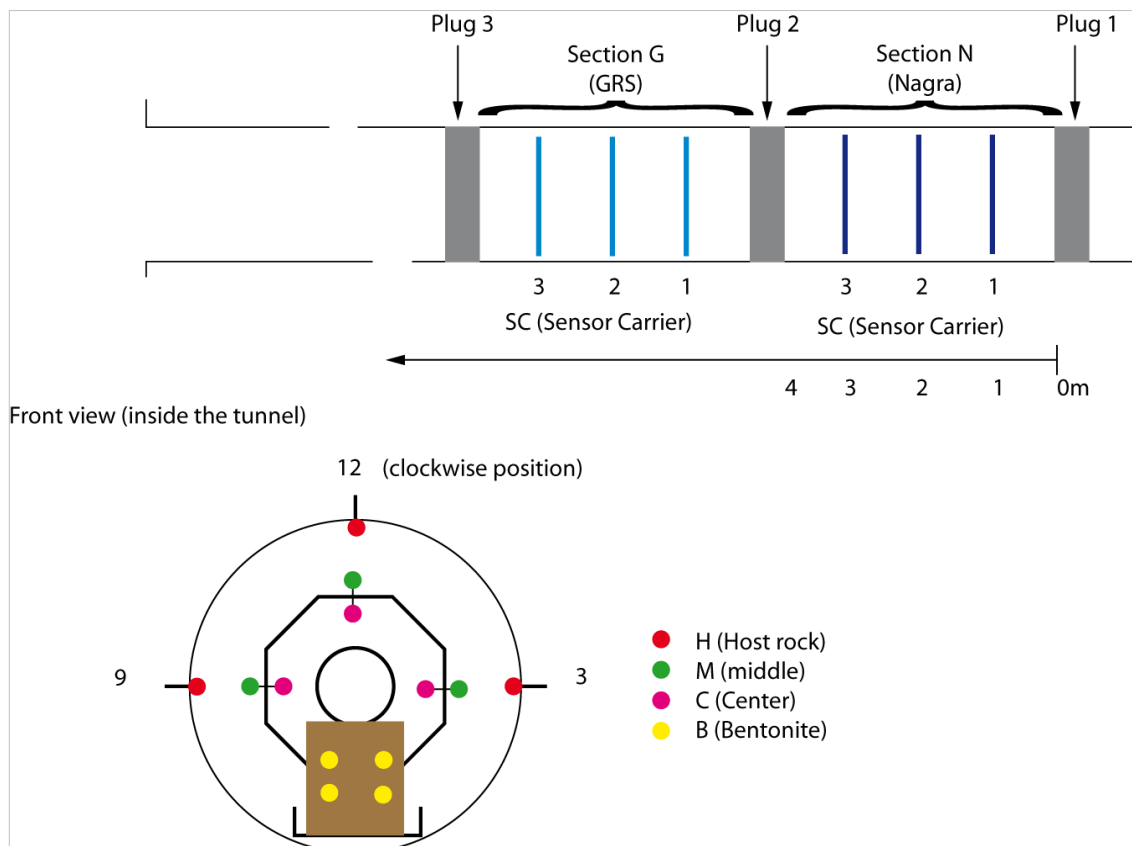


**Fig. 5.6** Position of sensors in the buffer and on the microtunnel wall /GAU 14/

After installation of each block/liner/carrier package the heater was inserted and the remaining void backfilled with granular buffer material using an auger system (Fig. 5.7, left). An additional compaction of the buffer was not possible. The three buffer materials (blocks, granular bentonite, and sand/bentonite) were characterized in the laboratory in terms of their petrophysical, thermal and hydraulic properties. Table 5.1 summarizes the basic properties. On-site measurements gave slightly different values for the granular materials. Emplacement density was estimated by comparison to the total emplaced buffer mass and the microtunnel volume obtained from a 3D scan of the microtunnel geometry (Fig. 5.7, right).

Two 4 m long electrical heaters (providing each a maximum power of 2400 W) were installed in the central steel liner (Figs. 5.4 and 5.5, right). Heaters were designed to be operated by either power or temperature control, and they function independently for the two sections. 24 thermocouples (12 for each section), placed on 6 radial planes at the inner part of the 8 mm thick heater liner allow for monitoring of the heater surface temperature in four radial directions. Heat transmission between the sections and through the front and back plug of the test section is limited by the thermal insulation of the plugs.



**Fig. 5.7** Left: Granular buffer emplacement using an auger system, right: 3D image of the microtunnel test section before installation for volume calculation /GAU 14/

**Table 5.1** Basic properties of HE-E buffer materials

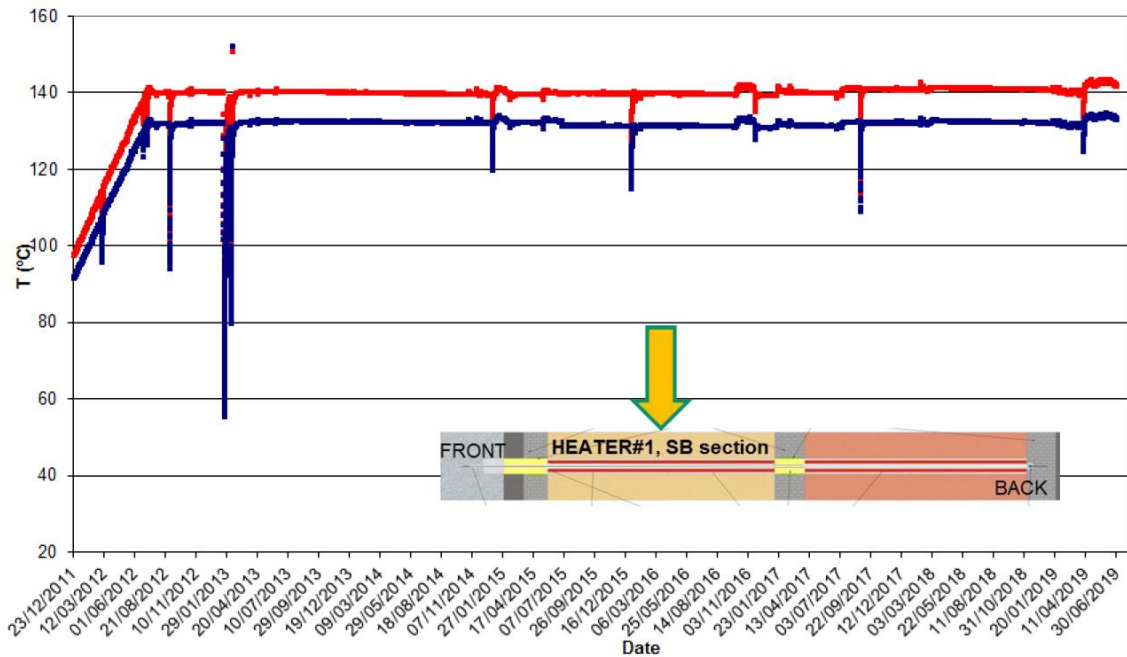
	<b>Bentonite Blocks</b>	<b>Granular Bentonite</b>	<b>Sand/Bentonite</b>
Water content (% by mass)	10.34	5.4	4.1
Bulk density (kg/m <sup>3</sup> ), preceding laboratory measurement	1993	1595	1440
Dry density (kg/m <sup>3</sup> ), preceding laboratory measurement	1806	1513	1383
Bulk density (kg/m <sup>3</sup> ), samples prepared as during emplacement		1543	1500

Installation of the HE-E was finished by mid 2011, and on June 30, 2011 the heaters were started. Since then, the experiment has been running without major problems. Three main heating phases can be distinguished: A first phase of 3 months with a linear liner temperature increase to 80 – 90 °C, a second phase with linear temperature increase of another 9 months to reach 140 °C on the liner, followed by the third phase with a constant liner temperature which has been maintained to date.

#### **5.2.1.2 Monitoring results**

Since start-up of heating in 2011, a vast amount of data has been recorded. In this report, only the most important results can be shown. More details about the data accumulated until 2014 can be found in the PEBS reports /GAU 14, WIE 14a/. Since then, the system showed very little evolution.

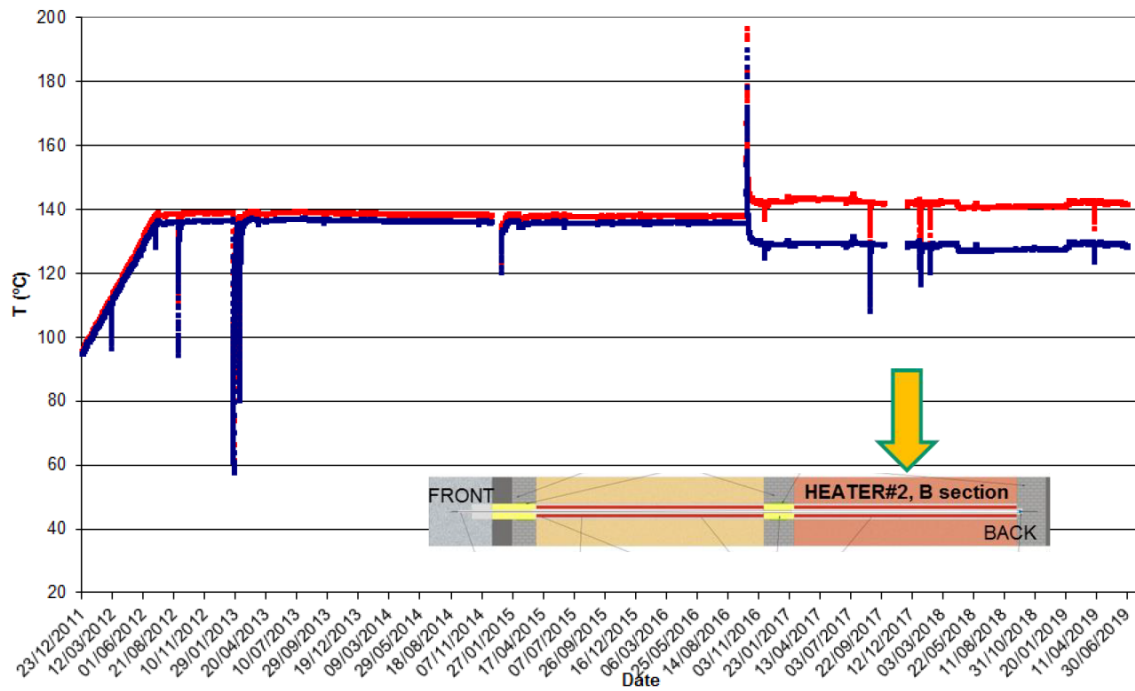
As planned, external temperature at the heater liner reached 80 °C on day 95 day of the heating phase for the sand/bentonite heater (Heater HE-E SB) and on day 93 for the bentonite heater (Heater HE-E B). The maximal temperature of 140 °C was reached on day 368 and 390, respectively. Since then the heaters have been run at constant temperature. The liner temperature in the center of the sand-bentonite section is shown in Fig. 5.8.



**Fig. 5.8** Heater liner temperature in the central part of the sand-bentonite section. Red: top of liner, blue: bottom of liner /AMB 19/

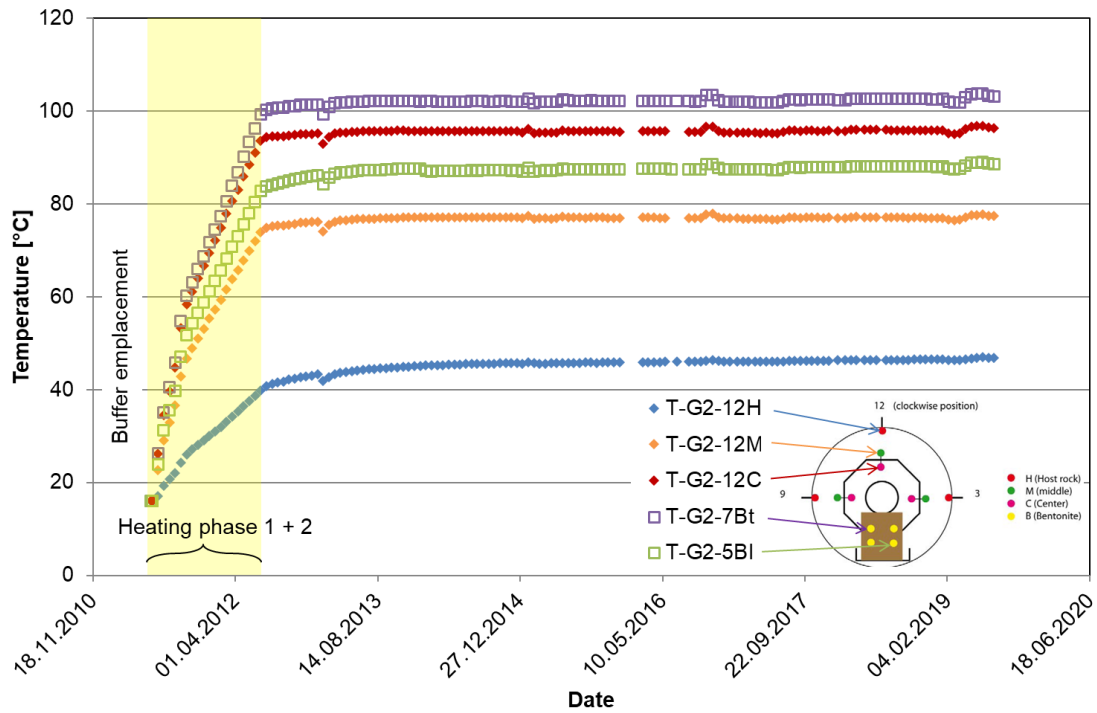
A few electricity supply incidents caused short-term disruptions of the heating, otherwise the system ran without major problems. Note that the temperature at the top of the liner is slightly higher than at the bottom. This is due to the higher thermal conductivity of the bentonite blocks below the liner in comparison to the granular buffer material – heat is conducted away from the heater more easily at the liner bottom.

Figure 5.9 shows the liner temperature in the center of the pure bentonite section. The picture is similar to Fig. 5.8, however, the power needed to maintain the constant temperature of 140 °C is slightly different in the two sections of the experiment, as a consequence of a slight difference in thermal conductivity of the various buffer materials. From October 1 – 3, 2016, an accidental overheating happened in the bentonite section, recognizable by the temperature peak up to 200 °C. While the overall effect of this incident was very small, the difference between top and bottom liner temperature was larger afterwards. A possible explanation could be an extra drying of the immediate liner vicinity, impairing the contact especially to the granular bentonite.



**Fig. 5.9** Heater liner temperature in the central part of the bentonite section. Red: top of liner, blue: bottom of liner /AMB 19/

Examples of the temperature evolution in the buffer are shown in Figs. 5.10 and 5.11. The results shown have been measured in the heater midplane of the sand-bentonite and the pure bentonite section. Temperature evolution in both sections is very similar due to similar thermal properties of the two granular materials (the overheating incident in the bentonite section is not visible in the buffer temperature measurements, Fig. 5.11). The temperatures in the bentonite blocks (7Bt and 5BI) are slightly higher than those at comparable distance from the heater in the sand-bentonite buffer (12C and 12M, Fig. 5.10) because of the higher thermal conductivity of the blocks. This is less pronounced in the pure bentonite section due to a slightly higher thermal conductivity of granular bentonite in comparison to the sand-bentonite. Due to the overall low thermal conductivity of the dry buffer the thermal gradient is quite high in both sections (from 140 °C on the heater surface to 45 °C on the microtunnel surface, 12H).



**Fig. 5.10** Temperature evolution at selected points in the central part of the sand-bentonite section

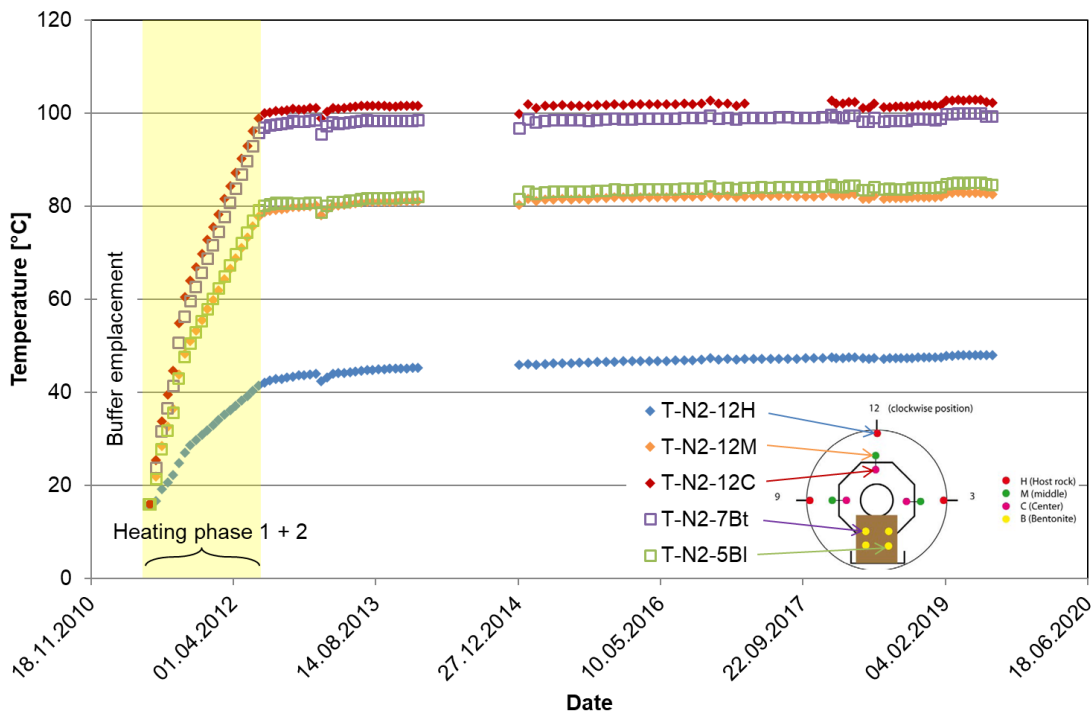


**Fig. 5.11** Temperature evolution at selected points in the central part of the pure bentonite section

Relative humidity measurements inside the EBS show a similar behaviour in both heated sections: a fast increase in the relative humidity close to the rock, with almost all sensors at that location showing a relative humidity of 100 % before the end of the second year of heating and a strong reduction in the relative humidity for those sensors located near the heaters. Figure 5.12 shows this for the sand-bentonite section.

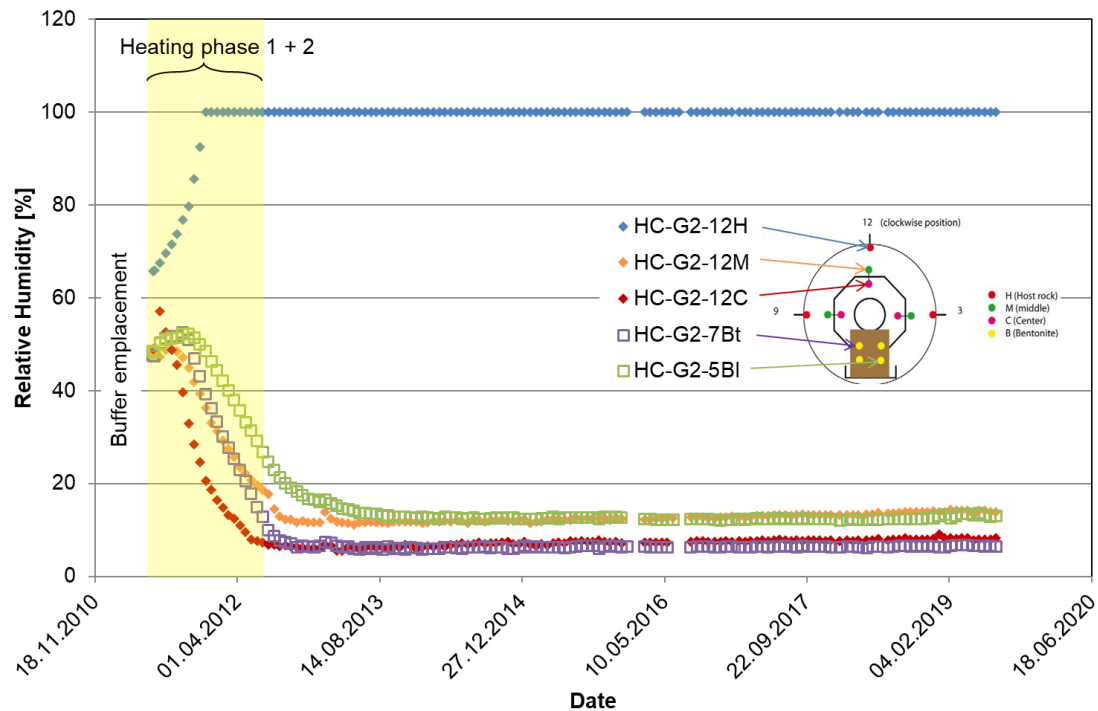


**Fig. 5.12** Relative humidity evolution at selected points in the central part of the sand-bentonite section

Water vapour is expelled to the outer and cooler parts of the buffer, where full saturation and 100 % relative humidity are reached after 5 months of heating. Similar results are obtained for the pure bentonite buffer (Fig. 5.13), although it takes about one year to reach 100 % humidity, due to the higher bentonite content.

Re-saturation of the inner buffer is slow, as it is governed by pore-water supply from the surrounding clay. As mentioned earlier, the microtunnel was not excavated for the HE-E, but had undergone a complex de-saturation/re-saturation history during the preceding ventilation test. Pore pressure measurements in the rock close to the microtunnel show that the near-field was and still is in suction, and only at distances over 1 m from the tunnel surface positive pore-water pressures are observed. Therefore, considerably more time will be needed until a significant re-saturation inside the buffer can be

expected. Since no significant changes in the buffer evolution can be expected during the next few years, different options of continuing or shutting down the experiment are currently discussed between the partners.

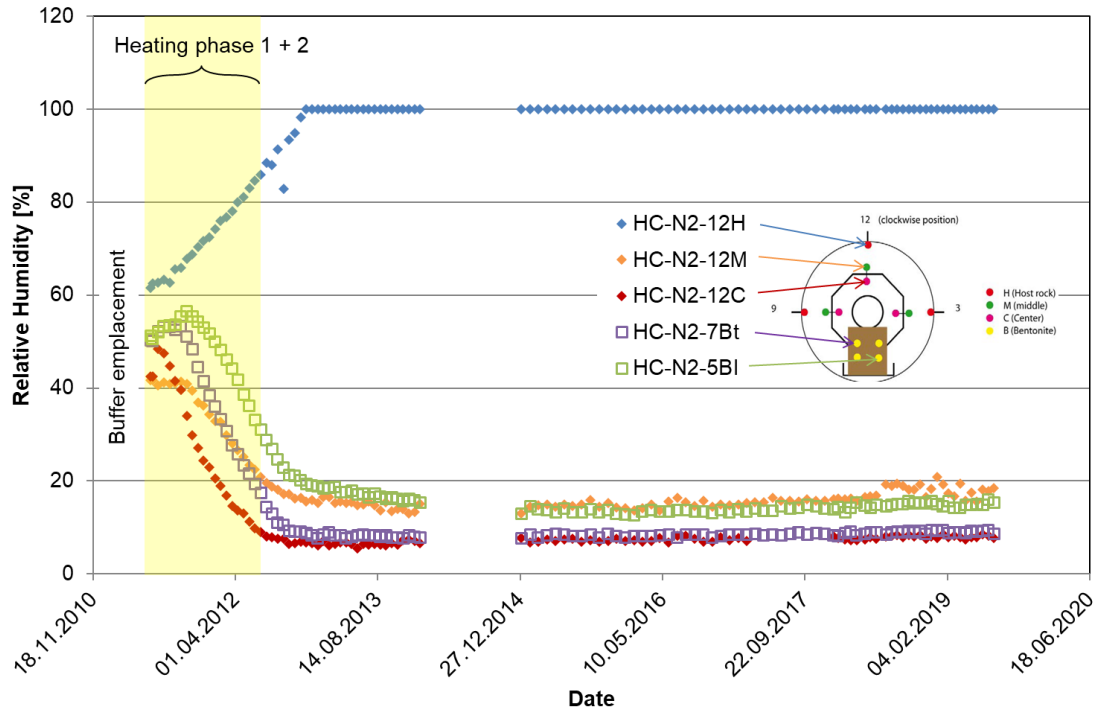


**Fig. 5.13** Relative humidity evolution at selected points in the central part of the pure bentonite section

The hydraulic conductivity and swelling pressure of the buffer materials cannot be evaluated in the in-situ test, since the buffer is still very dry. The pure granular bentonite buffer could be installed with a density of more than  $1500 \text{ kg/m}^3$ , which makes acceptable hydro-mechanical (HM) properties after re-saturation probable. The emplacement density of the sand/bentonite buffer, however, is very poor ( $1383 \text{ kg/m}^3$ ). This is a result of the narrow grain distribution of the material which was chosen to avoid segregation during the emplacement, and of the impossibility of additional compaction after emplacement. Consequently, laboratory measurements showed insufficiently low permeability [WIE 13] and too low swelling pressure [VIL 14] of this material at the density achieved on site, making modifications necessary.

## 5.2.2 FE-M

The Swiss repository concept for spent fuel or vitrified high-level waste foresees the sequential emplacement of self-shielding waste containers in several hundred-metre-long horizontals in Opalinus clay /MUE 17/. The containers are to be emplaced in the centre of the tunnel section, resting on highly compacted bentonite blocks. The remaining void is backfilled with granular bentonite (compare the setup of the HE-E, Section 5.2.1.1). The bentonite buffer (blocks and granular bentonite) is an important part of the engineered barrier system.

The FE (Full-scale Emplacement) experiment was designed by Nagra to realistically simulate the conditions in a single emplacement tunnel at the MTRL. It involves a realistic geometry and temperature evolution and natural buffer re-saturation. The main aim is the investigation of high-level waste repository induced THM coupled effects on the host rock and validation of respective models. Further objectives are the technical feasibility of disposal tunnel construction, the optimisation of buffer material production, and the investigation of emplacement procedures /MUE 17/. Nagra's partners in the FE are Andra, BGR, DOE, FANC, NWMO, and RWM. GRS is taking part in the FE monitoring (FE-M), with pore pressure monitoring near the front and rear ends of the gallery using minipiezometers (Section 5.1). An overview of the FE layout is shown in Fig. 5.14.

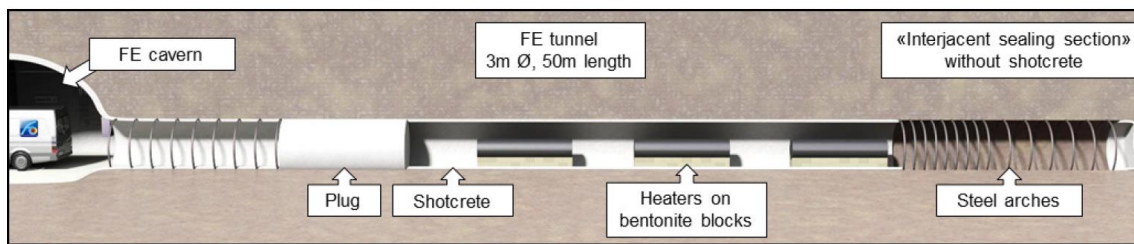


**Fig. 5.14** General experiment layout of the Full-scale Emplacement (FE) experiment at MTRL; sensors and granular backfill are not displayed /MUE 15/

### 5.2.2.1 Construction and instrumentation

The 50 m long FE tunnel was excavated between April and July 2012. Excavation steps were limited to 1.5 m/day to allow early rock support to be installed on the same day /MUE 17/. The rear 12 m of the tunnel are equipped with steel sets and reinforce-

ment mesh (Fig. 5.14). The rest of the tunnel is supported by mesh-reinforced shotcrete.

Rock instrumentation started already prior to tunnel construction, using boreholes drilled from the FE cavern (Fig. 5.14). More sensor boreholes were drilled radially from the tunnel after its construction. Rock sensors include more than 600 temperature sensors, relative humidity and water content sensors, deformation sensors, total pressure and pore-water pressure sensors. An overview of the instrumentation boreholes is given in Fig. 5.15. Four GRS minipiezometers were installed around the shotcrete-lined front part of the tunnel in 6 m deep boreholes drilled from the FE cavern in March 2013. Another four minipiezometers were placed in 3 m deep radial boreholes around the rear part of the FE tunnel, plus one piezometer in a borehole of 10 m depth drilled axially into the heading face, in September 2013. All minipiezometers are equipped with RTDs (resistance temperature detectors) for additional temperature measurement.

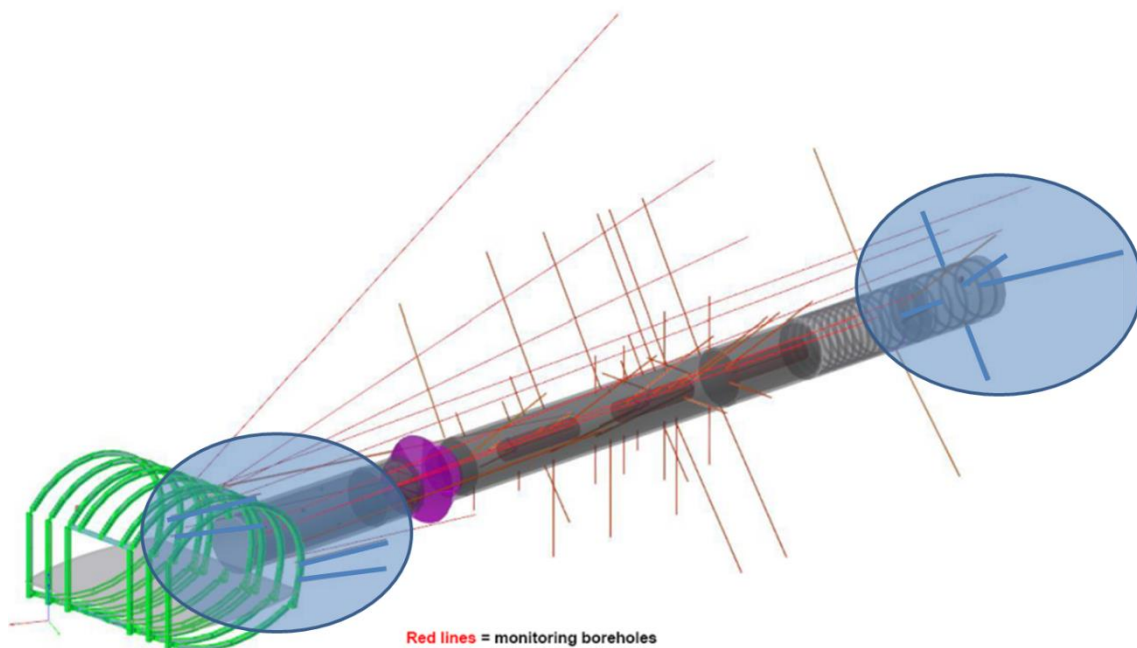


**Fig. 5.15** Sketch of the FE monitoring boreholes (red lines). GRS minipiezometers are located around the plug (blue area on the left) and at the tunnel rear end (blue area on the right)

Figure 5.16 shows impressions from the drilling of the minipiezometer boreholes. For the minipiezometers at the tunnel rear, the transducer racks had to be installed in water-tight boxes (Fig. 5.17) and are no longer accessible because of the tunnel backfill.



**Fig. 5.16** Drilling of the minipiezometer boreholes: tunnel front (left), radial borehole at the tunnel rear (right)



**Fig. 5.17** Installation of the transducer racks in the rear part of the tunnel

The positions of the minipiezometers are shown in more detail in Figs. 5.18 and 5.19.

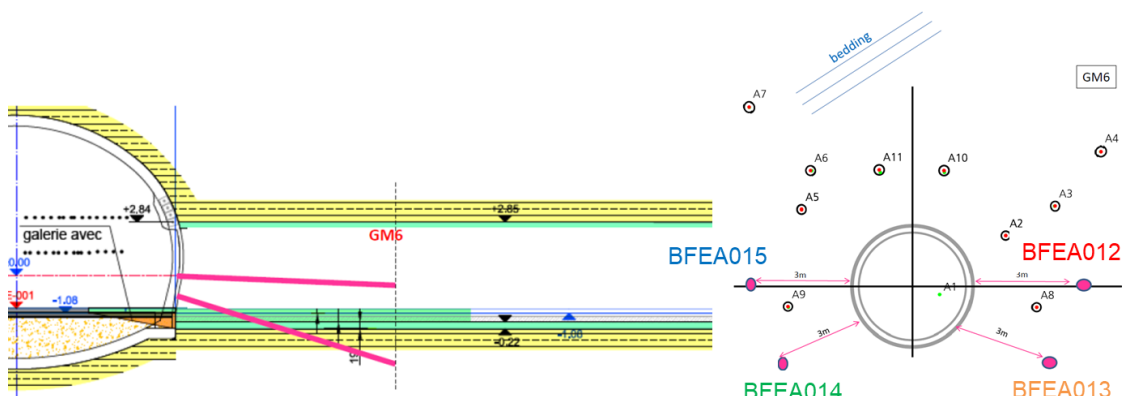


**Fig. 5.18** Location of minipiezometers 6 m from the tunnel front

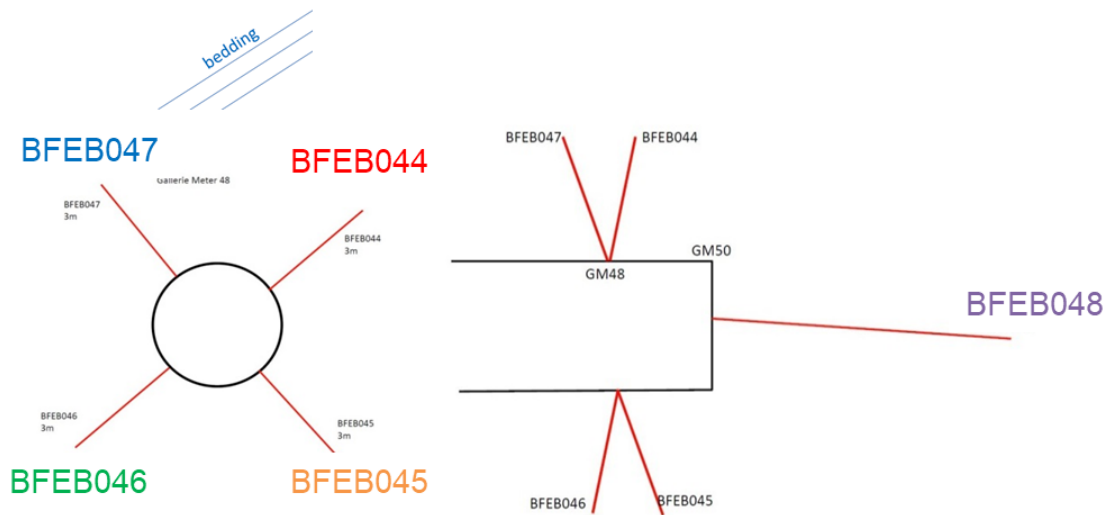


**Fig. 5.19** Location of minipiezometers close to the rear part of the tunnel

After completion of rock instrumentation and instrumentation of the tunnel wall, the granular buffer, bentonite blocks, and three mock-up containers equipped with electrical heaters were emplaced between July 2014 and March 2015 (Fig. 5.20).

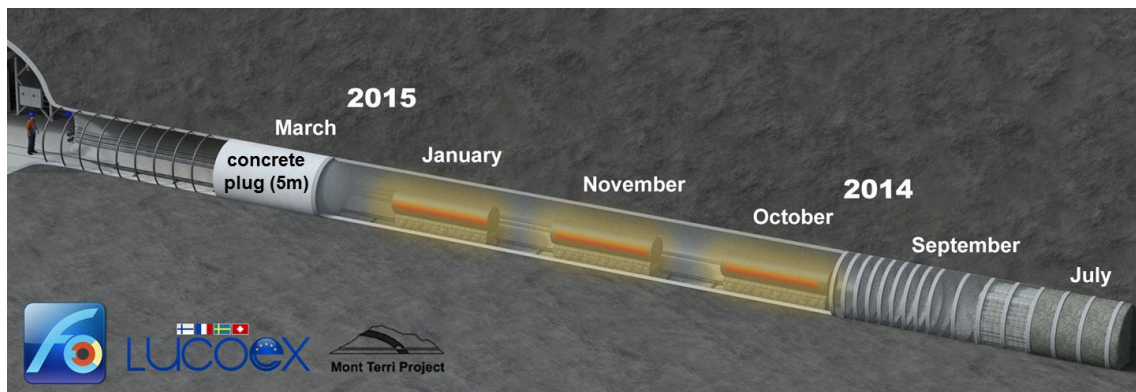


**Fig. 5.20** Sketch of the emplacement and backfilling sequence in the FE tunnel at Mont Terri /MUE 15/

Heating was started in December 2014 with the “deepest” heater. In February 2015, the central heater and the heater closest to the plug were switched on. The heaters are power-controlled. For the first heater, power was increased in three steps to the design value of 1350 W, the other heaters were run at 1350 W from the beginning. Maximum temperatures on the containers between 130 °C and 150 °C were expected. Figure 5.21 shows the temperature on the central heater at different locations. The maximum temperature (on top the heater, compare Section 5.2.1.2) is 131 °C and has remained nearly constant since 2017.

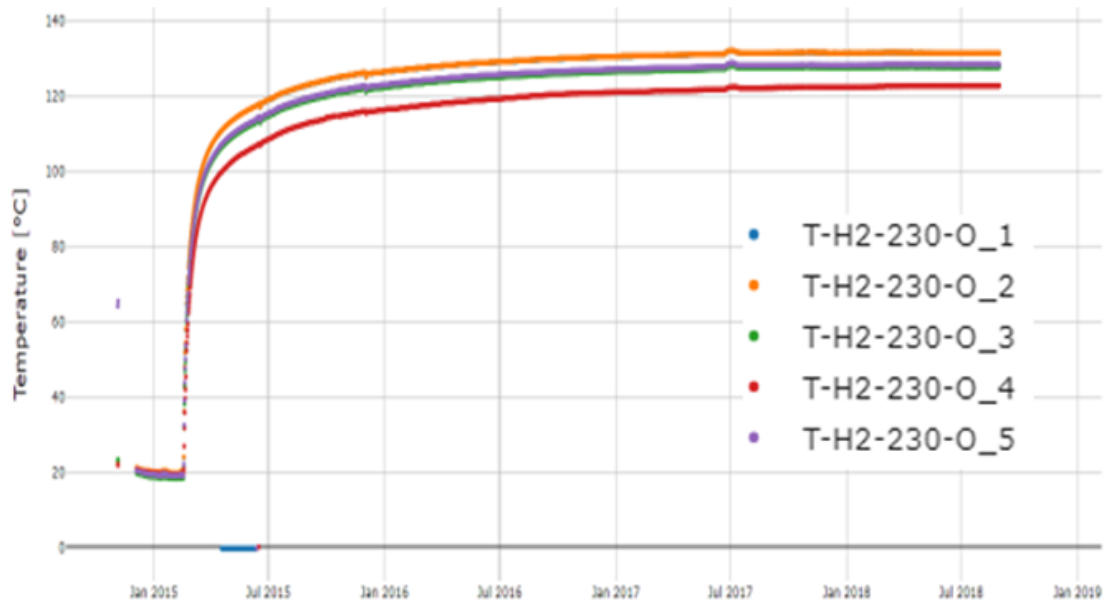


**Fig. 5.21** FE central heater temperature evolution at different locations on the container /FIR 19/

#### 5.2.2.2 Pore pressure and related temperature monitoring results

The temperature measured at the minipiezometers located 6 m from the tunnel front is shown in Fig. 5.22. Start-up of heating leads to a very moderate temperature increase by about 2.5 °C in more than four years, a consequence of the large distance to the heaters. Superimposed is a seasonal change in temperature, since the transducers are only 6 m from the ventilated FE cavern.

Figure 5.23 shows the pore-water pressure measured at the four minipiezometers near the tunnel front. After a transient period during the ongoing works in the tunnel the measured pressures stabilized between 0.6 MPa and 1.2 MPa. This is in the range of what was expected. Seasonal changes are visible also in the pressure curves and can be correlated to the temperatures. Since 2018 the pressure values seem to increase steadily, at the same time the rate of temperature rise accelerated (Fig. 5.22).

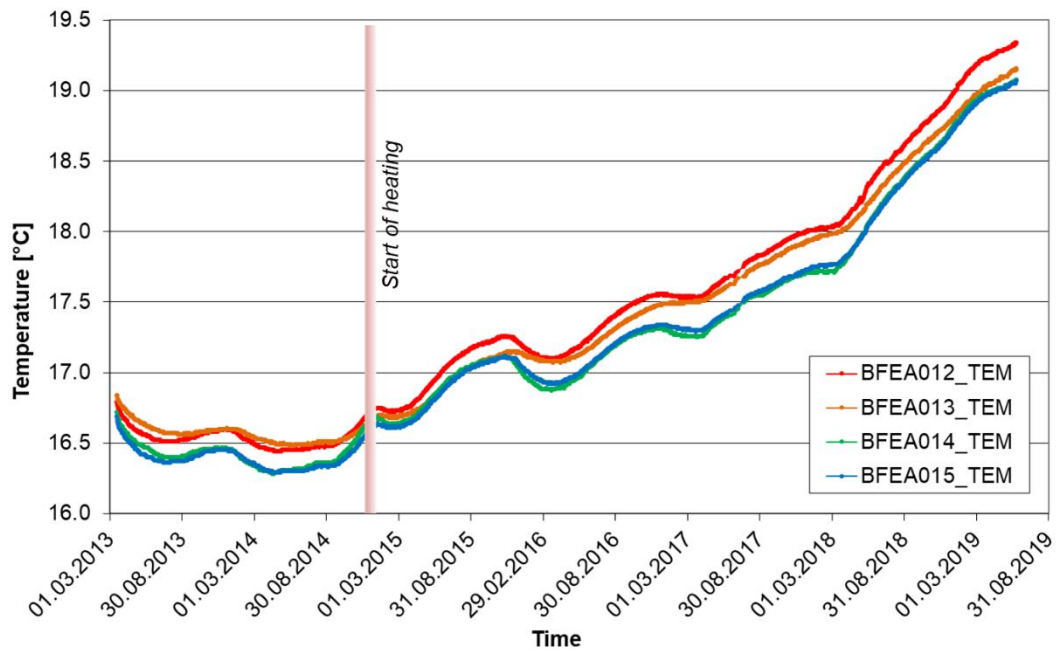


**Fig. 5.22** Temperature measured at the minipiezometers located 6 m from the tunnel front

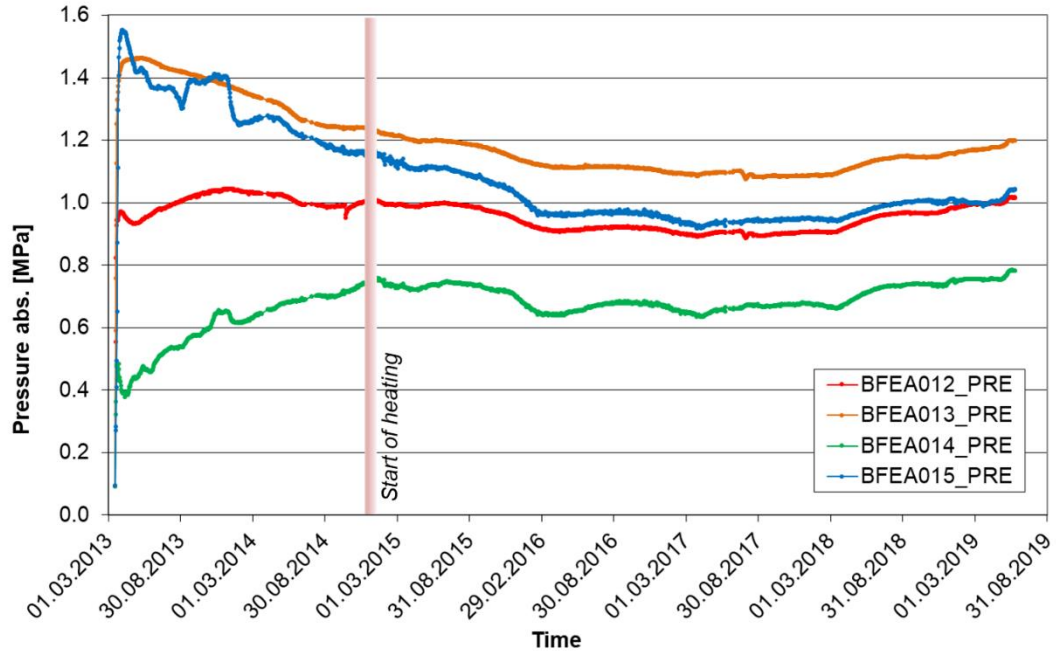


**Fig. 5.23** Pore-water pressure measured at the minipiezometers located 6 m from the tunnel front

The temperature measured at the minipiezometers located in the rear part of the tunnel is shown in Fig. 5.24. There is an early and very significant temperature peak in July 2014. The reason is the installation of a concrete wall in the rear part of the tunnel, after backfilling the last few tunnel metres. The hydration heat of the concrete causes the temperature peak. With some delay after start-up of heating, temperature rises again at all measuring points. At the minipiezometers arranged radially around the FE tunnel, the temperature rise in four years is slightly above 2 °C. At the minipiezometer located 10 m behind the tunnel face (BFEB048, see Fig. 5.19), the temperature rises only by about 1 °C, because this measuring point is much farther away from the heaters.

Seasonal changes of temperature are not observed, because the minipiezometers in the rear part of the FE tunnel are far away from any ventilated part of the MTRL.

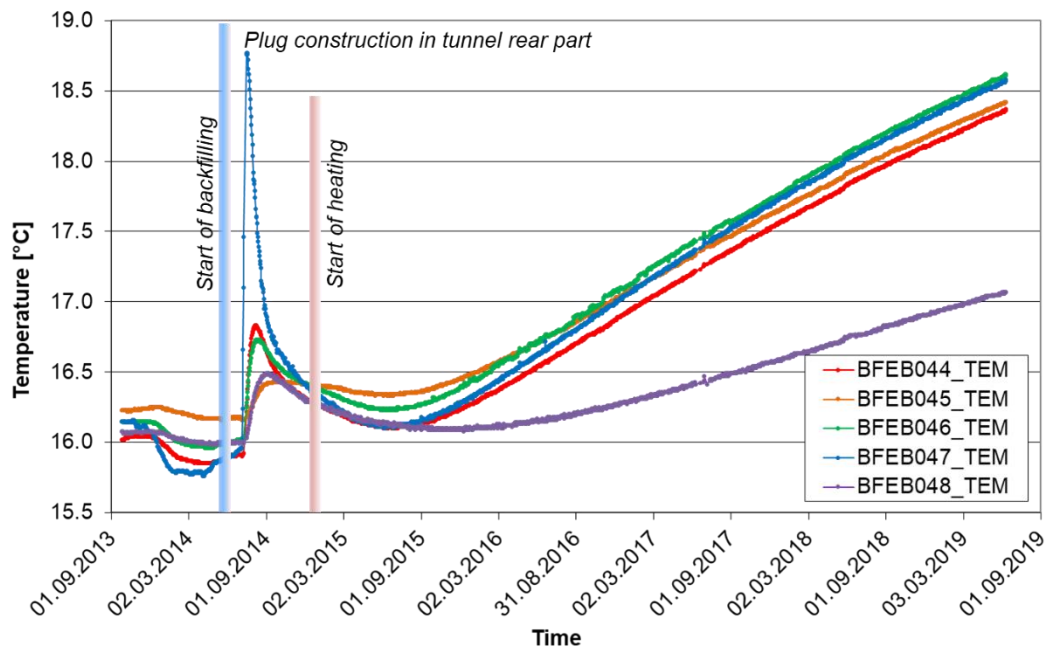


**Fig. 5.24** Temperature measured at the minipiezometers located in the rear part of the tunnel

Measured pore-water pressures around the rear part of the FE tunnel (Fig. 5.25) are rather different from those near the tunnel front. Due to the missing shotcrete lining the rock is more damaged, which was already detected during drilling of the instrumentation boreholes. Especially the minipiezometers located in the inclined upward boreholes (BFEB044 and BFEB047, see Fig. 5.19) show little more than ambient pressure. In the inclined downward boreholes (BFEB045 and BFEB046), pressures consolidated

and rise more or less significantly with heating, although they are still lower than the pressures measured in the front part of the tunnel.

The minipiezometer installed 10 m behind the FE tunnel face (BFEB048 in Fig. 5.25, left scale) showed a pressure of more than 2.1 MPa shortly after installation, which is probably higher than the pore pressure in the undisturbed rock, due to increased stresses in the course of tunnel excavation. Pore pressure diminished slightly with time due to stress redistribution around the tunnel and has stabilized at 1.8 MPa, which seems in good agreement with the undisturbed pore pressure (compare Section 5.2.5).

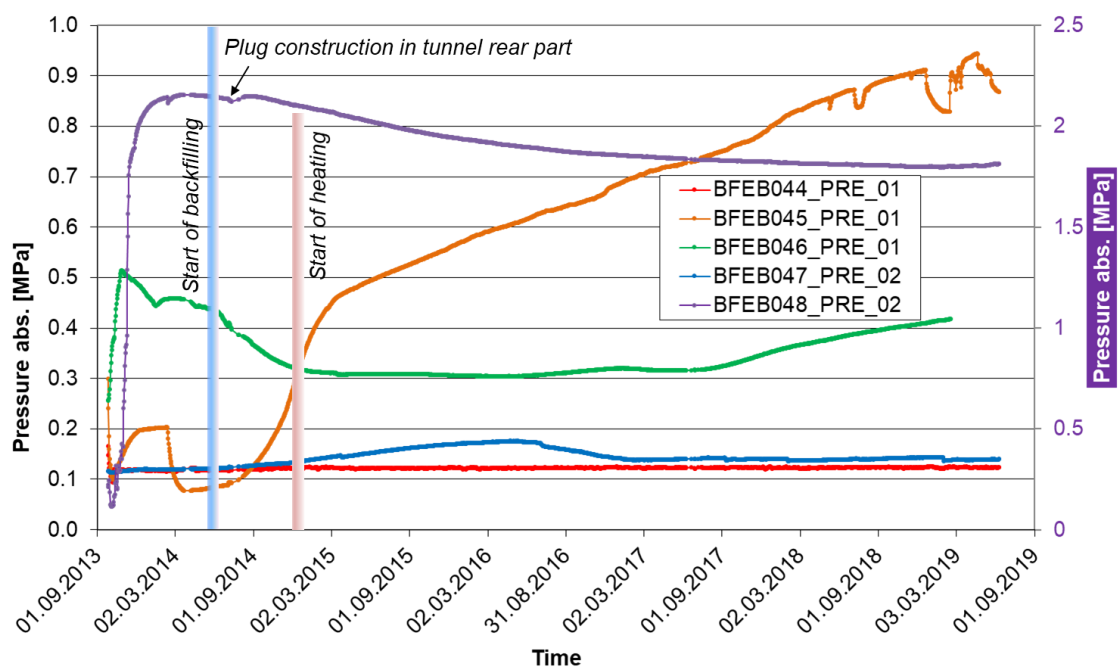


**Fig. 5.25** Pore-water pressure measured at the minipiezometers located in the rear part of the tunnel (BFEB048: scale on the right)

### 5.2.3 DM-A

The DM-A experiment addresses long-term deformation mechanisms of the clay rock. In the frame of this experiment, a borehole dilatometer probe was installed in a horizontal borehole of 18 m depth drilled in June 2009 parallel to the bedding. The first four years of deformation monitoring were already reported /ZHA 14/.

The probe (Fig. 5.26) consists of a packer inflated with water at low pressure (0.5 MPa). Differently oriented deformation sensors integrated in the packer are thus coupled to the borehole wall. Borehole wall convergence has been recorded since installation, as well as temperature and relative humidity in the borehole. When the deformation sensors seemed to approach the end of the measurement range, a second load level with increased packer pressure (1 MPa) was started in November 2011.

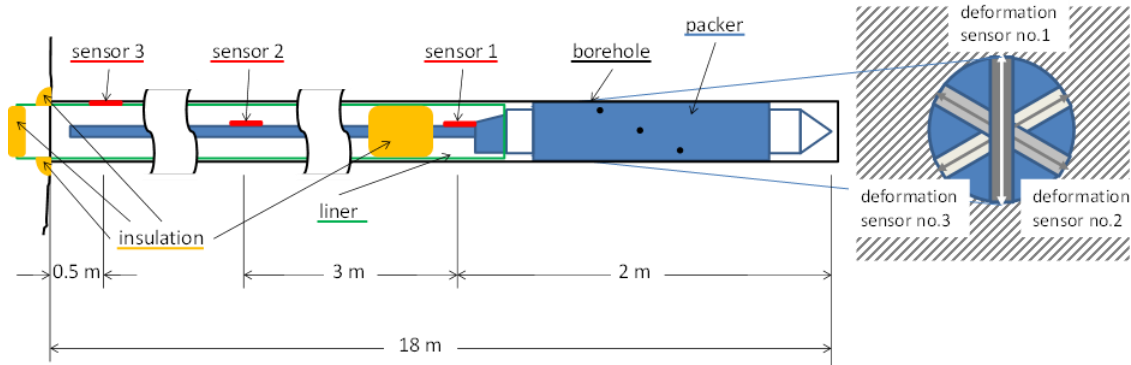


**Fig. 5.26** Dilatometer probe for borehole deformation monitoring (sensor 1 – 3: temperature/relative humidity sensors)

100 % relative humidity was reached at sensor 3 on the borehole wall shortly after installation. While sensor 2 failed after 18 months, sensor 1 reached 100 % relative humidity about three years after installation. Temperature at sensor 3 (0.5 m from the tunnel surface) shows the typical seasonal variations, while sensor 1 (16 m in the borehole) measured a constant temperature of about 14 °C. Before mid of 2017, however, all coupled temperature/relative humidity sensors had failed.

Figure 5.27 shows the readings of the deformation sensors. At first, only the sensors no. 2 and 3 worked, and it was assumed that sensor no. 1 had been broken during the installation. The other two sensor showed different deformation rates at first, but after the packer pressure increase the curves were nearly parallel, with a deformation rate in the range of  $10^{-8} \text{ s}^{-1}$ . Towards the end of 2015, the vertically oriented deformation sen-

sor no. 1 started measuring. It is assumed that, due to the installation procedure, the sensor had become stuck and had no contact to the borehole wall. Later this contact was established and the sensor started measuring.

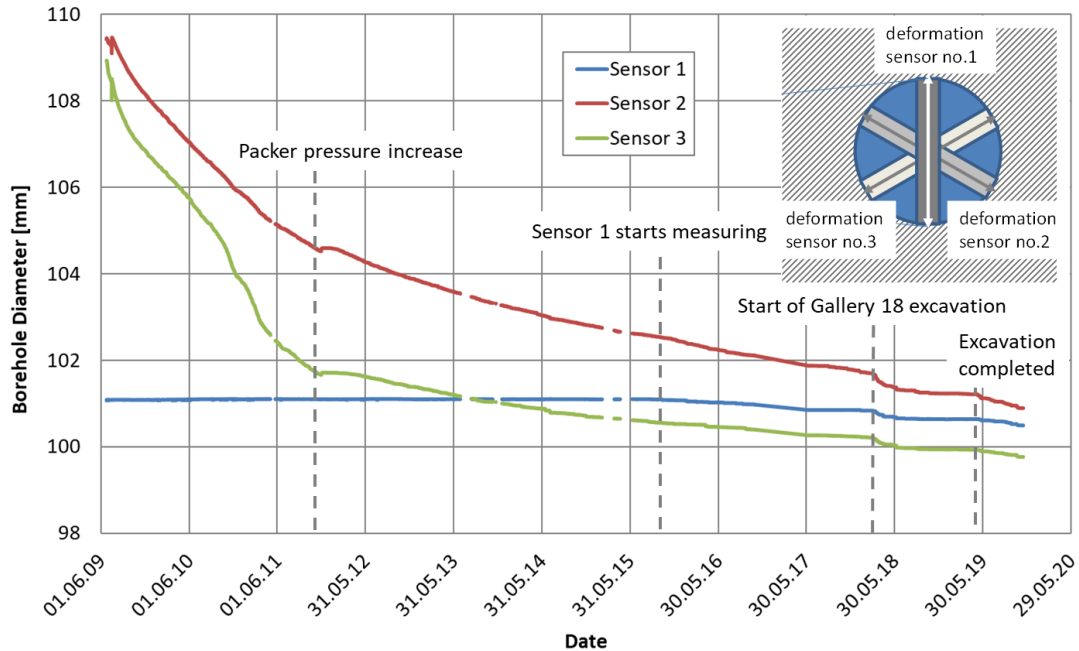


**Fig. 5.27** Deformation sensor readings of the dilatometer probe

With the start of the excavation work of Gallery 18 in March 2018, the deformation rates of all sensors increased temporarily by 1 – 2 orders of magnitude. At this time, the SW and CS-D niches were excavated (Figs. 3.3 and 4.1) at a distance between 30 m and 50 m to the dilatometer borehole. The excavation work had a significant effect on both the air temperature in the MTRL and the rock temperature as shown in Fig. 5.28 (air and rock temperature are measured about 20 m away from dilatometer borehole – in a direction away from the excavation). The rock temperature increase by 2 °C is clearly out of the range of the seasonal changes.

After completion of the excavation in the middle of 2019 the deformation rate (Fig. 5.27) seems to increase again. The reason for this behaviour is not clear yet.

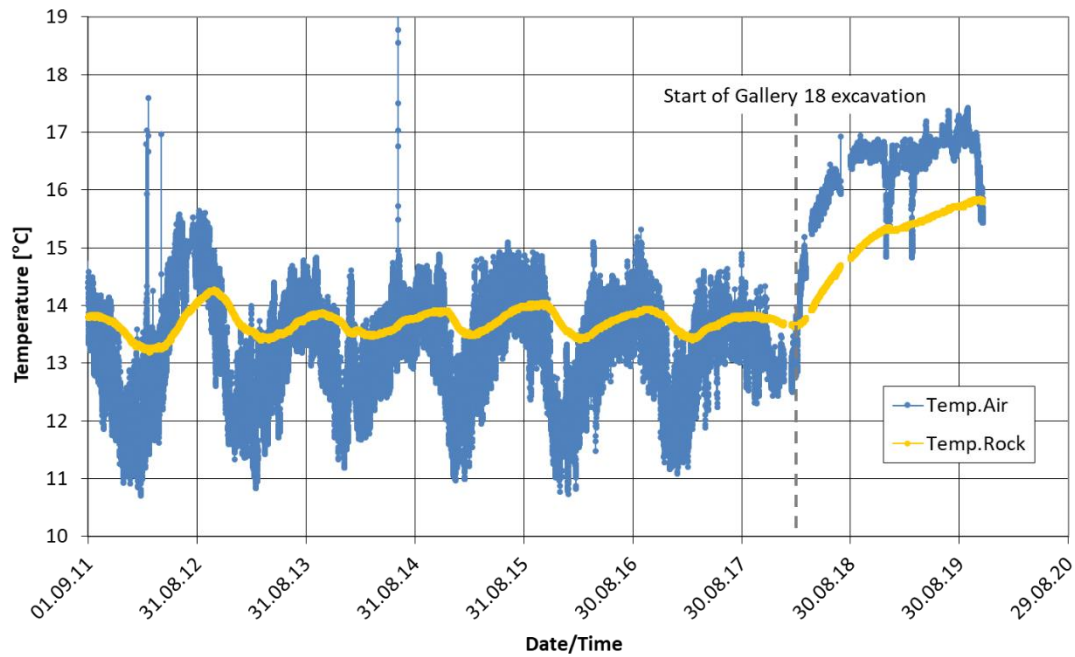


**Fig. 5.28** Air and rock temperature measured in the SB niche, about 20 m from the dilatometer borehole

An important aspect of the long-term deformation monitoring is the characterization of deformation mechanisms. Time-dependent deformation can occur as a consequence of stress and pore pressure changes, swelling/shrinking processes, or damage. It is not yet clearly proven whether creep, as it is known from rock salt, is relevant. To determine whether pore pressure changes play a role in the long-term deformation measured in the dilatometer borehole, a set of minipiezometers had been installed in the vicinity in 2011. Figure 5.29 shows their location in relation to the dilatometer probe. Two minipiezometers (DM-B01 and DM-B02) are located at about 1 m distance to the probe, roughly in direction of the bedding and perpendicular to it, respectively. A third reference minipiezometer (DM-B03) is located about 4 m below the dilatometer, in a region that is expected not to be influenced by the dilatometer borehole.

The measured pore-water pressure is shown in Fig. 5.30. The reference minipiezometer equilibrates with the surrounding pressure very quickly and shows a stable pressure of 1.4 MPa, which is increasing very slowly. For the other two minipiezometers, equilibration takes much longer, and the measured pressures are much lower: 0.3 MPa parallel to the bedding and 1.0 MPa perpendicular (in relation to the dilatometer probe).

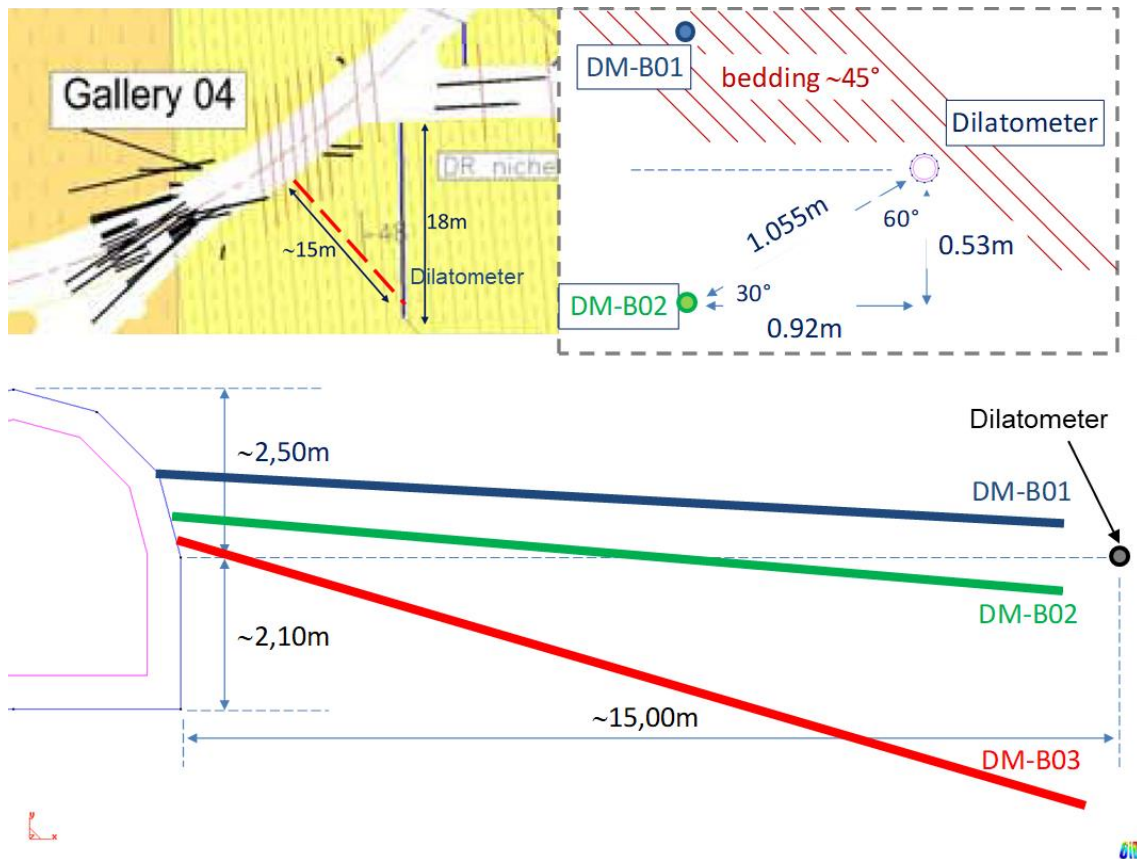


Fig. 5.29 Location of minipiezometer boreholes near the dilatometer probe

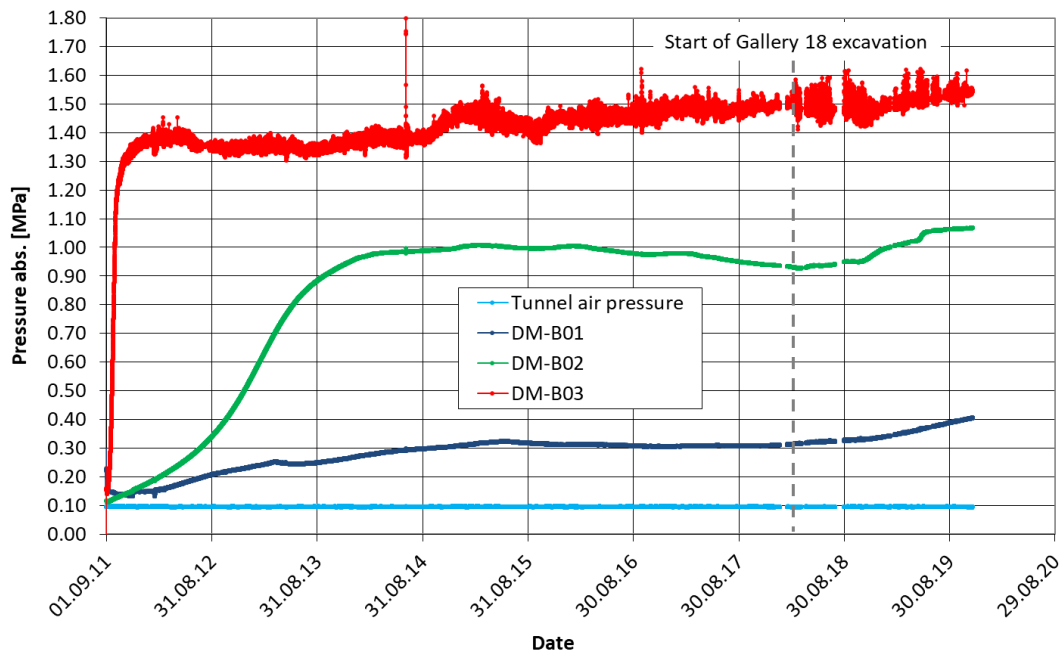


Fig. 5.30 Measured pore-water pressure at the minipiezometers in the vicinity of the dilatometer probe

Between 2015 and 2017 there is no significant change in pore pressure close to the dilatometer borehole while deformation continues. This is a clear hint that pore pressure change alone cannot be the reason for time-dependent deformation of the Opalinus clay. This was also confirmed by earlier model simulations /ZHA 14/. Whether still-ongoing swelling processes or actual creep are the cause of the borehole wall deformation cannot be decided at the present stage.

With the start of Gallery 18 excavation, the pore pressure near the dilatometer probe starts increasing (Fig. 5.30), the increase, however, is more gradual than those of temperature and borehole deformation. Pore pressure seems again to play a minor role in time-dependent deformation.

#### **5.2.4 SB-A**

The SB-A experiment was initiated by BGR in 2013 with the aim of testing borehole sealing materials and methods. Several boreholes (Fig. 5.31) were sealed and tested in terms of in-situ permeability changes of the total system of sealing material and borehole EDZ.

In September 2014, GRS drilled and instrumented two minipiezometer boreholes parallel to the test borehole SB-A3 (Fig. 5.32) before the latter was drilled. The idea was to monitor pore-water pressure prior, during and after drilling of the test borehole.

Figure 5.33 shows the pressure evolution in the two minipiezometers SB-A6 and SB-A7. After a short equilibration time of three weeks, SB-A6 showed the expected pressure of about 1.5 MPa, while the pressure at SB-A7 was significantly lower (0.7 MPa), which is possibly due to a near-borehole damage.

The test borehole SB-A3, 0.5 m away from each of the two piezometer boreholes, was drilled between March 8 and 10, 2016. Both piezometers show an instant reaction: a pressure increase at SB-A6 and a slight pressure decrease at SB-A7. Afterwards, pressure at SB-A6 decreases in the long term and stabilises at values comparable to those of SB-A7. Obviously, the vicinity of SB-A6 was unloaded by the drilling of SB-A3, so that conditions comparable to SB-A7 were created. The further evolution of the measured pressures shows, however, that there is no hydraulic shortcut between the two boreholes, so damage induced by drilling is very limited.

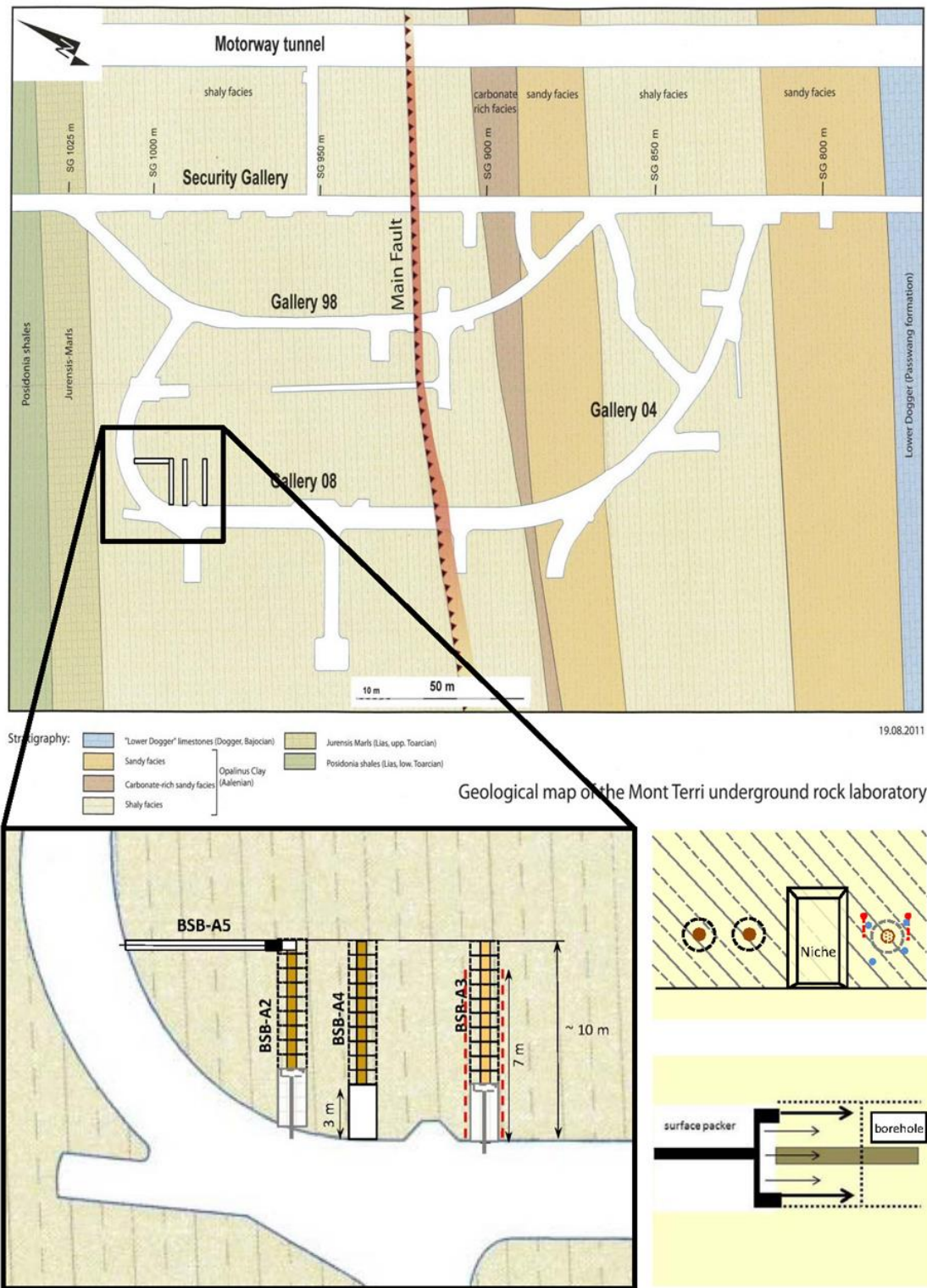
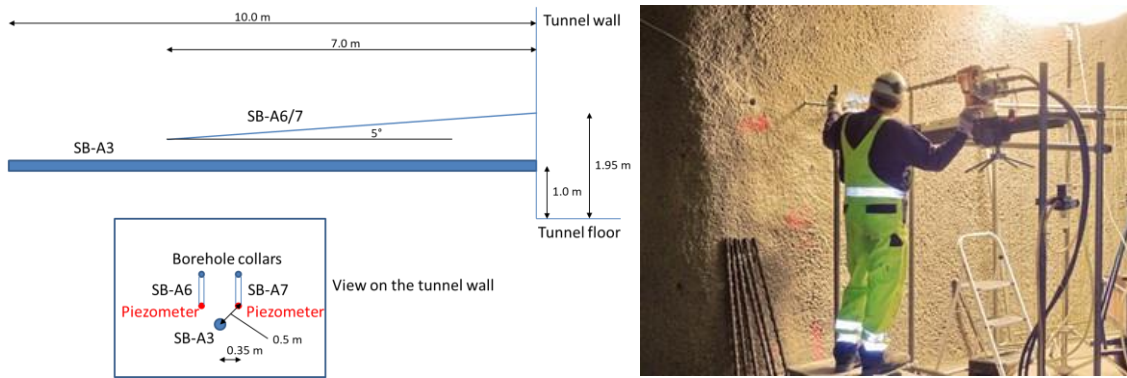
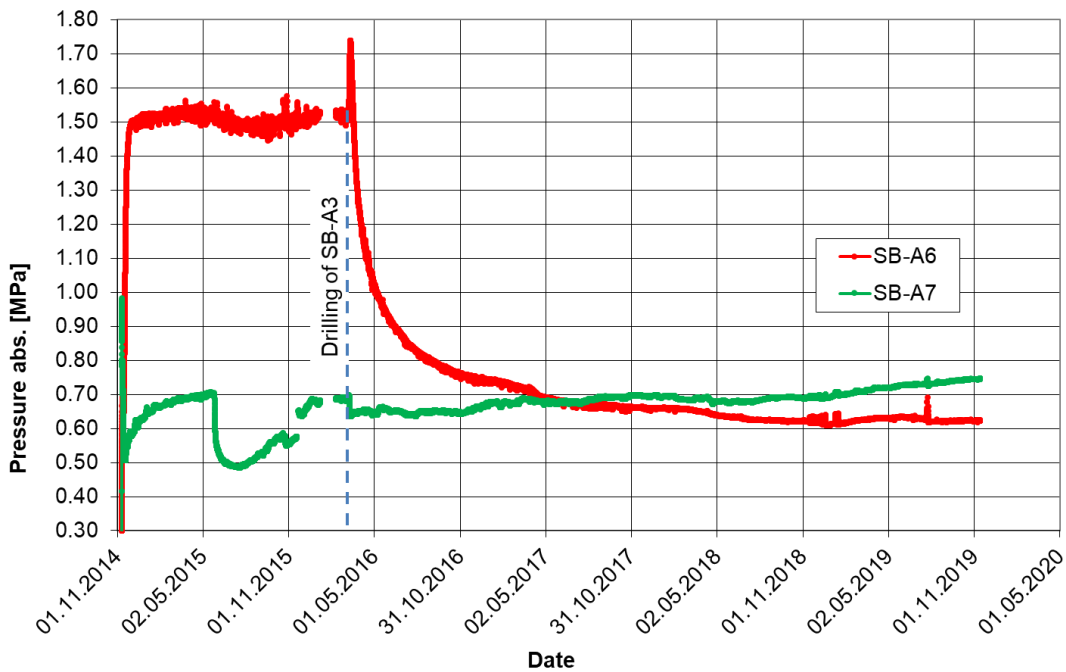


Fig. 5.31 SB-A experiment location and boreholes /HES 16/



**Fig. 5.32** Location of minipiezometer boreholes (SB-A6 and SB-A7) in relation to the experiment borehole SB-A3 (left), piezometer borehole drilling (right)



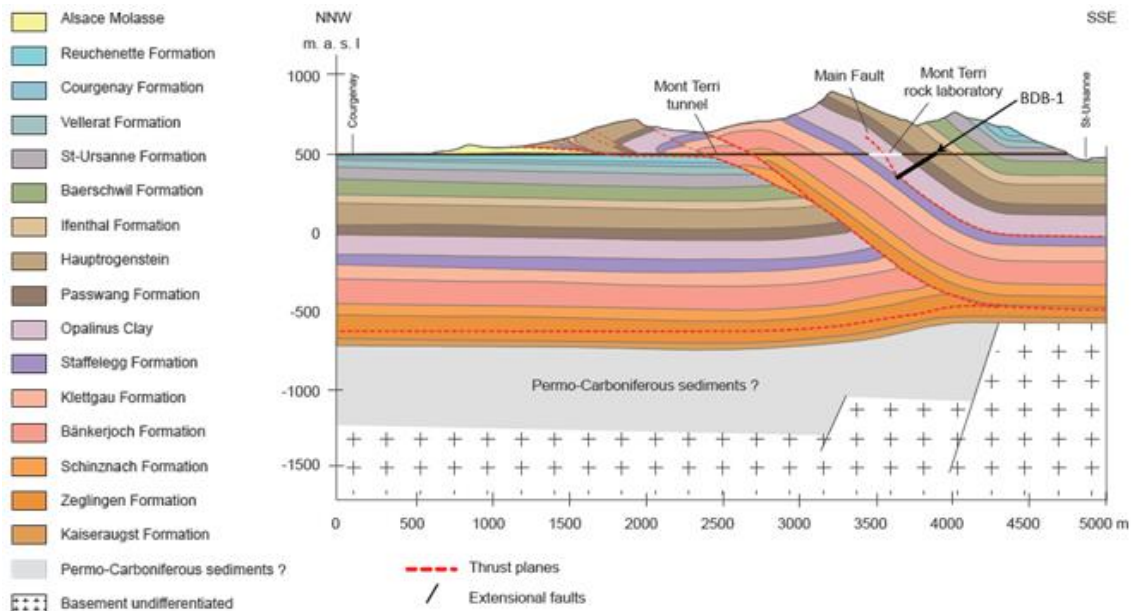
**Fig. 5.33** Pore-water pressure measured at minipiezometers SB-A6 and SB-A7

## 5.2.5 DB

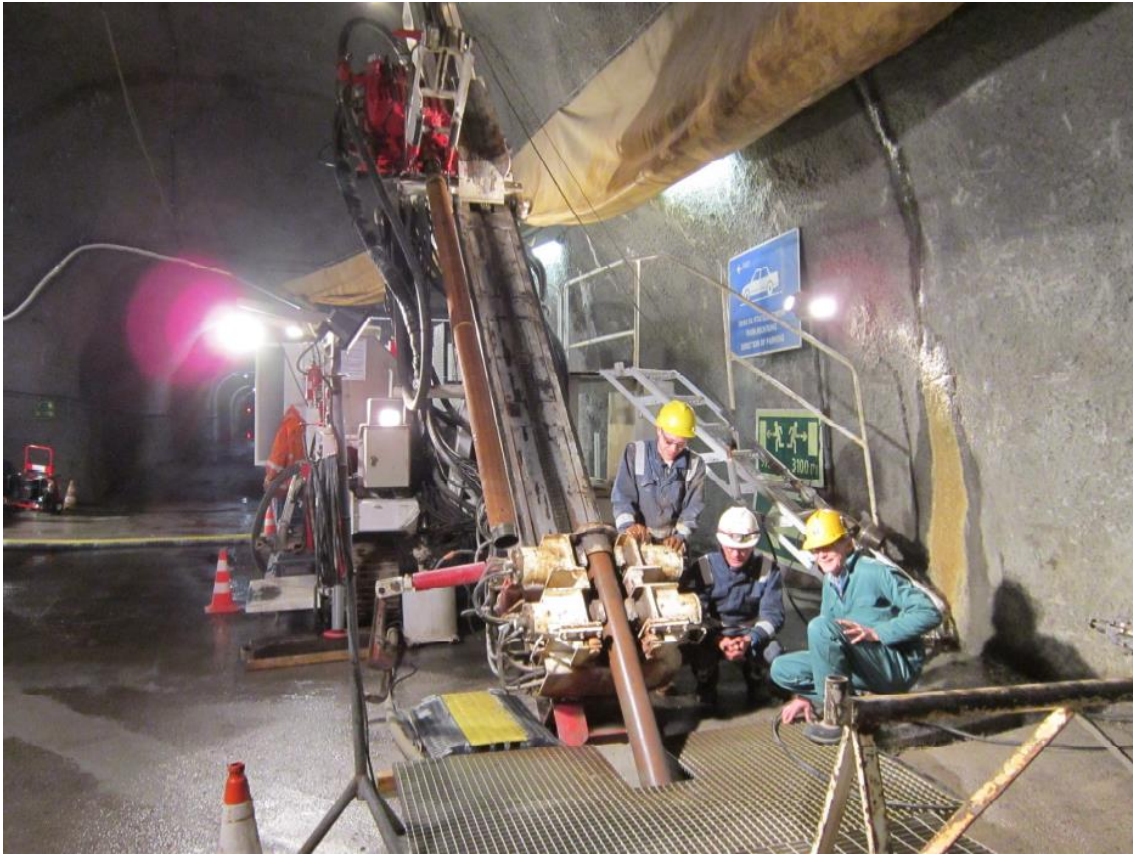
For evaluation and prediction of rock performance in the various in-situ experiments knowledge of the initial mechanical and hydraulic conditions is of special importance. Measurement of these, however, is not easy, since the original state is disturbed in the vicinity of the MTRL by the many existing excavations which, by unloading and ventilation, may have a large effect especially on the pore pressure distribution. Pore pres-

sure, on the other hand, is extremely important since it provides the driving force for buffer re-saturation and is also an indicator for rock saturation.

In order to gain knowledge on the pore pressure distribution in the undisturbed rock, as well as on hydraulic conductivity and thermal and chemical potentials, a 247.5 m long inclined borehole was drilled through the Opalinus clay and the neighbouring formations from the access gallery to the laboratory (BDB-1, Figs. 5.34 and 5.35). Samples were taken and the borehole was equipped with a multi-point probe for hydraulic conductivity and pore pressure measurement. This project was run as a joint effort of Swisstopo, IRSN, Nagra, NWMO, BGR, and GRS. Several detailed reports are available /YUC 15, YUC 16, YUC 17/.

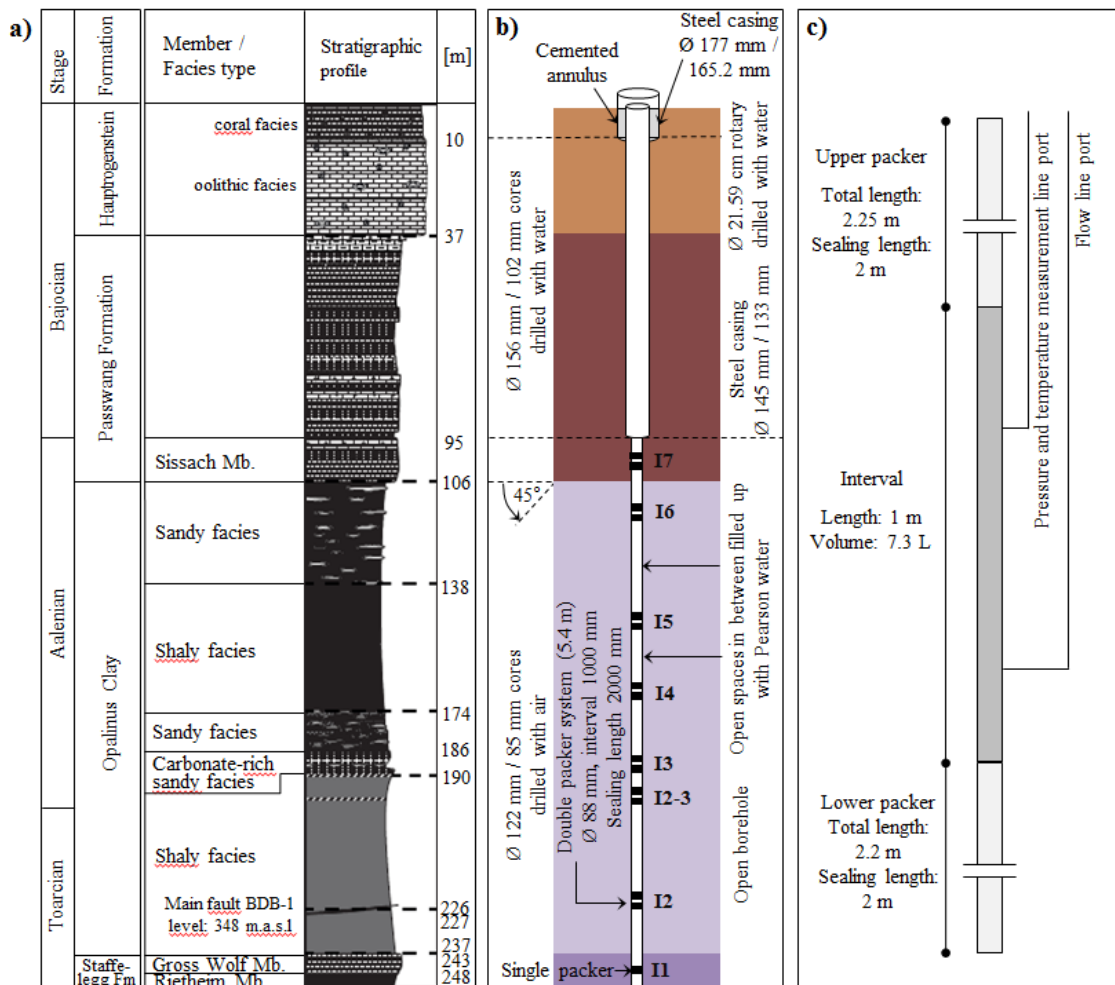


**Fig. 5.34** Geological cross section of the Mont Terri anticline, showing the location of the MTRL (white line) and of the borehole BDB-1 (heavy black line), crossing the lower art of the Dogger aquifer, the entire Opalinus clay formation and the upper part of the Liassic marls /YUC 17/



**Fig. 5.35** Drilling of the 250-m-borehole BDB-1

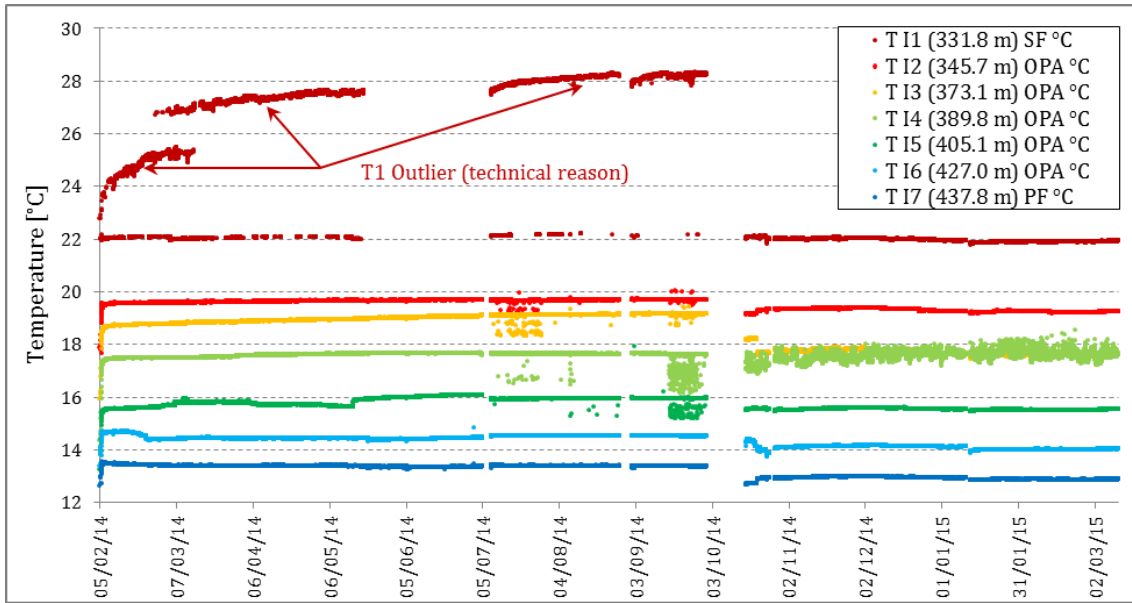
The borehole was drilled with a diameter of 156 mm and an inclination of 45° in December 2013 and January 2014. At the end of January, a multipacker probe (Solexperts, CH) was installed. Figure 5.36 shows the stratigraphic sequence along the borehole, an overview showing the packer measuring interval locations, and a blow-up of a single interval. The probe features five double packer testing intervals and an interval port in the Opalinus clay, a single packer in the Staffelegg formation at the borehole bottom, and a double packer interval in the lowermost zone of the Passwang formation above the Opalinus clay /YUC 17/. Intervals were equipped with downhole temperature sensors and connected to pressure sensors at the borehole collar via stainless steel lines. Both the test intervals as well as the open borehole spaces between the packers were filled with Pearson water.



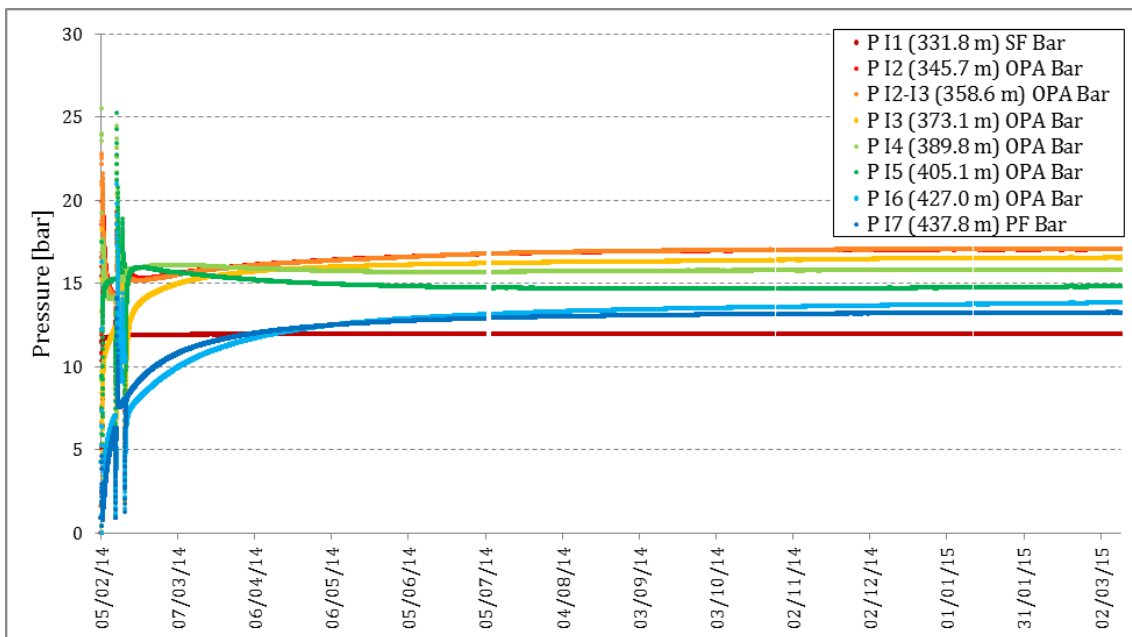
**Fig. 5.36** a) Stratigraphic sequence along the BDB-1 borehole, b) borehole configuration with packer intervals, c) packer interval detail /YUC 17/

Figure 5.37 shows the temperature evolution at the test intervals during the first year of monitoring. The respective pore pressure readings are shown in Fig. 5.38. After an equilibration time of 2 – 7 months depending on the test interval the readings are quite stable. From the measurements, depth profiles of temperature and pore pressure can be derived, as shown in Fig. 5.39.

The temperature varies between 21.9 °C at the Passwang formation / Opalinus clay boundary to 12.9 °C in the Staffelegg formation (Fig. 5.39 left). This corresponds to a mean geothermal gradient of 8.5 °C per 100 m which is considerably higher than the average geothermal gradient of 3.3 °C per 100 m found in the Swiss Molasse Basin /YUC 15/. This is explained by the relatively low thermal conductivity of the Opalinus clay, leading to heat accumulation and increased temperature.



**Fig. 5.37** DB first year monitoring results: temperature /YUC 15/



**Fig. 5.38** DB first year monitoring results: pore-water pressure /YUC 15/

Pressure monitoring in the BDB-1 borehole revealed anomalous overpressures up to 5.7 bar (0.57 MPa) in the Opalinus Clay (Fig. 5.39 right). These can be explained as residues from the maximum burial (Opalinus clay is overconsolidated), or they may result from an ongoing lateral thrust /YUC 15/. Due to the very low permeability of the Opalinus clay, an equilibrium of pore-water pressure with the surrounding strata has not been reached.

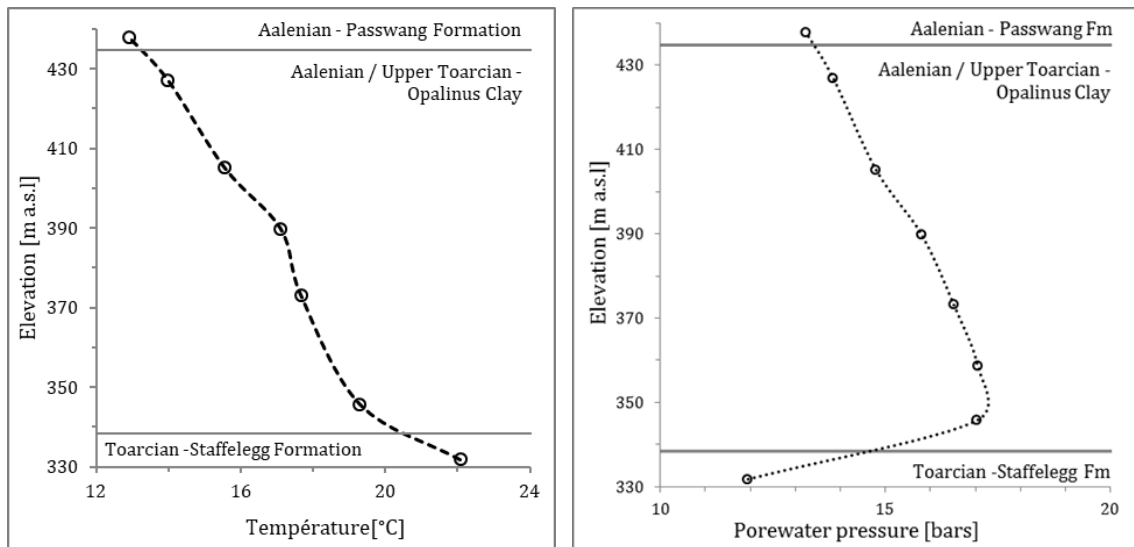


**Fig. 5.39** Depth profiles of temperature (left) and pore pressure (right) /YUC 15/

Figure 5.39 implies a pore pressure in the undisturbed Opalinus clay between 1.5 MPa and 1.8 MPa depending on the location, which is in good agreement with the measurements in the face of the FE tunnel (Fig. 5.25), the DM-A reference minipiezometer (Fig. 5.30), and the SB-A6 minipiezometer (Fig. 5.33).

Petrophysical parameters were determined in the laboratory using core samples from the borehole. The investigations included determination of water content (by oven-drying at 105 °C), bulk density and saturation (by immersion), grain density (by helium pycnometry of dried samples), and pore size distribution and specific surface (by nitrogen adsorption/desorption). A compilation of the results is given in Fig. 5.40 /YUC 15/.

The results show that for most parameters there is no clear distinction between the different facies of the Opalinus clay, except for the specific surface and the porosity, which are considerably higher in the shaly facies compared to the other facies. The mean porosities are 13.5 % in the shaly facies and 12 % in the sandy facies /YUC 17/. These values are rather in line with the water loss porosities measured in previous studies (13 % – 21 % for the shaly facies and 4.9 % – 17.5 % of the sandy facies) /BOS 17/, although on the low side for the shaly facies.

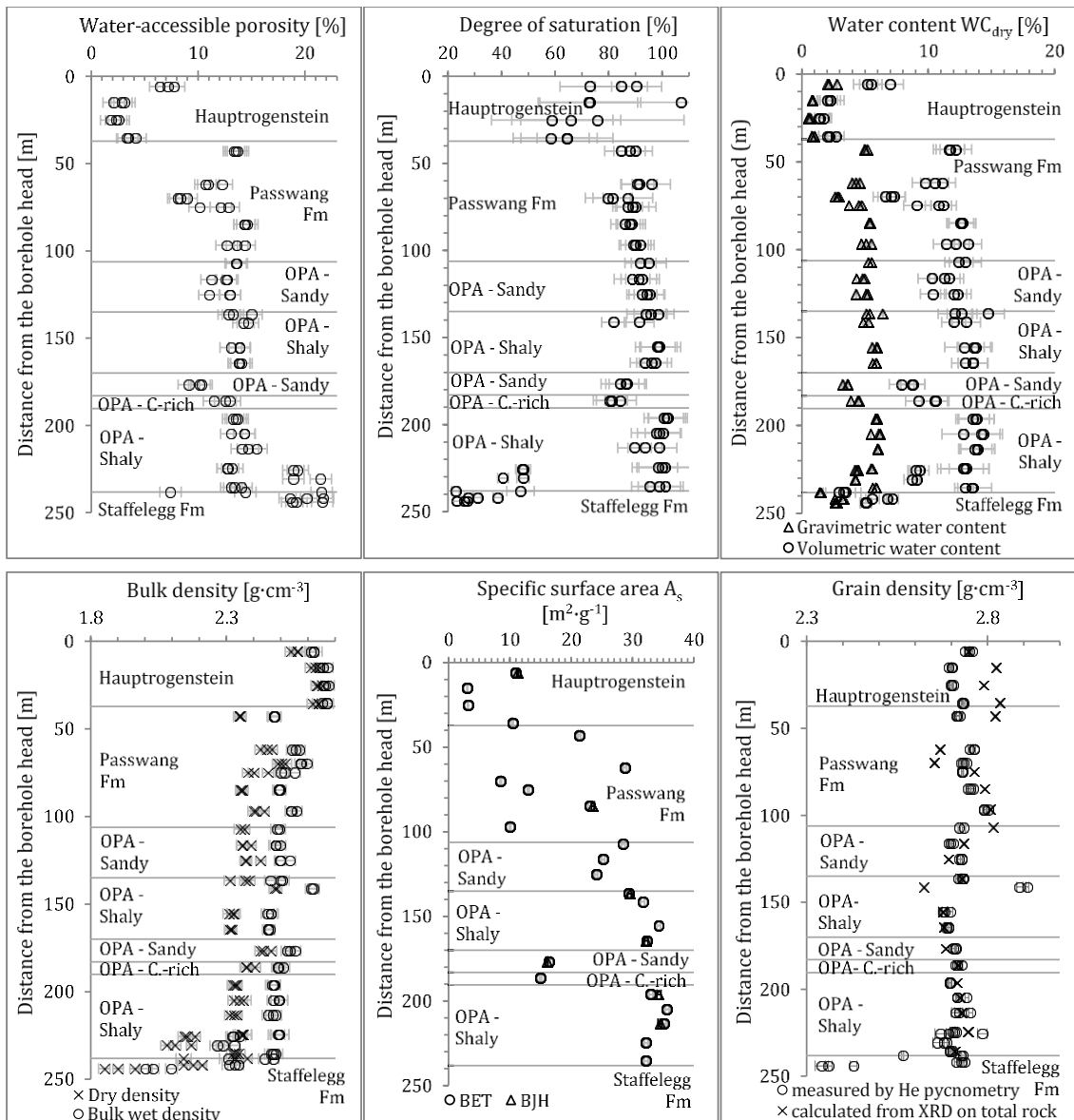


**Fig. 5.40** Profiles of petrophysical parameters (water loss porosity, degree of saturation, dry mass based water content, bulk density, specific surface area, grain density), determined on BDB-1 core samples /YUC 15/

For determination of hydraulic conductivity, pulse withdrawal tests (March/April 2015) and constant flowrate withdrawal tests (May – October 2015) were performed in all of the test intervals. Both test types resulted in comparable hydraulic conductivities, with a slight vertical variability ( $1 \times 10^{-13}$  m/s –  $7 \times 10^{-12}$  m/s). The results for the shaly facies (in the order of  $10^{-12}$  m/s) are somewhat higher than for the sandy facies (in the order of  $10^{-13}$  m/s) /YUC 17/.

## 5.2.6 MB-A

Between March 2018 and May 2019, the MTRL was enlarged by mining of the Gallery 18 (see Figs. 3.2 and 3.3) which is located mainly in the sandy facies of the Opalinus clay. Since, in comparison to data about the shaly facies, sandy facies data are still scarce, it was decided to perform a mine-by test during tunnel excavation, with the objective to observe and to capture coupled hydro-mechanical processes induced by the excavation. This experiment was performed by BGR with the participation of Swisstopo and GRS. A joint report on the experiment is planned. Since not all the partners' results are published yet, this report concentrates on GRS' results.

The idea was to mine the niches CS-D and SW first and use them for the installation of sensors in the rock around the future Gallery 18 (Fig. 3.3). Afterwards, the Gallery 18 would be excavated from the other side, as indicated by the red arrows in Fig. 3.3. Figure 5.41 is an enlarged sketch of the MB-A area.

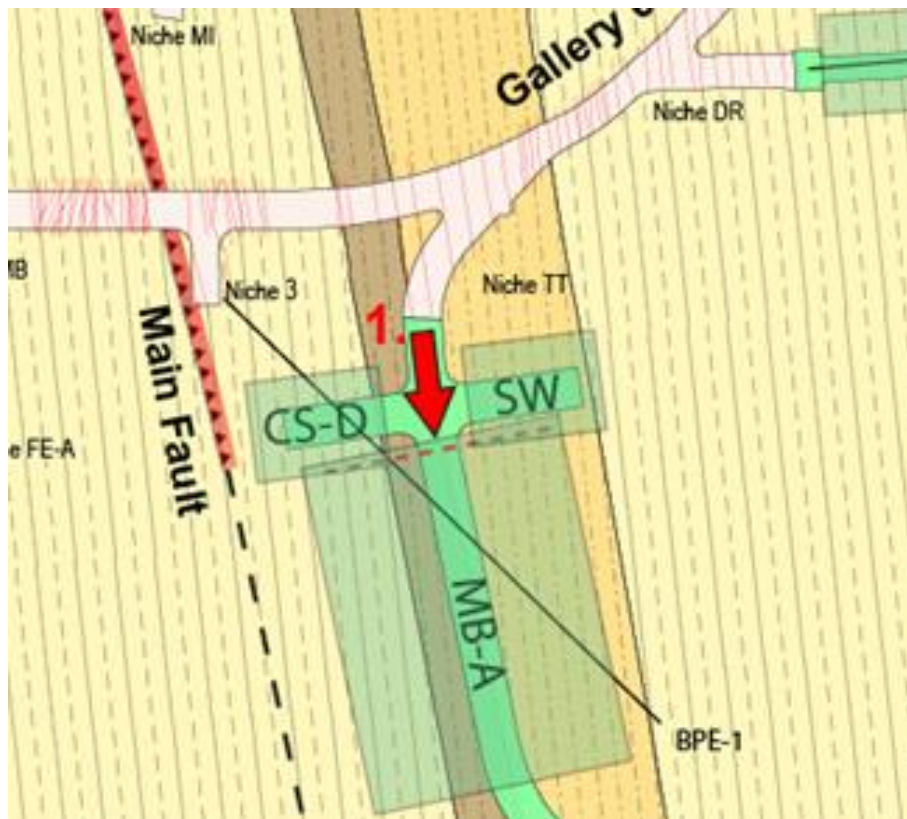


**Fig. 5.41** Sketch of the MB-A experiment area. Excavation stopped at the red dashed line, and instrumentation boreholes were drilled from the two niches CS-D and SW

### 5.2.6.1 Instrumentation

The niches CS-D and SW (Fig. 5.41) were excavated from March to May 2018. Excavation stopped at the red dashed line. Afterwards, instrumentation boreholes were drilled, and the MB-A region was instrumented with stress monitoring cells, inclinometer chains, and extensometer by BGR. GRS installed minipiezometers for pore pressure measurement. The main measuring cross section was located 15 m ahead of the excavation front. A plan view showing all planned instrumentation boreholes is shown in Fig. 5.42.

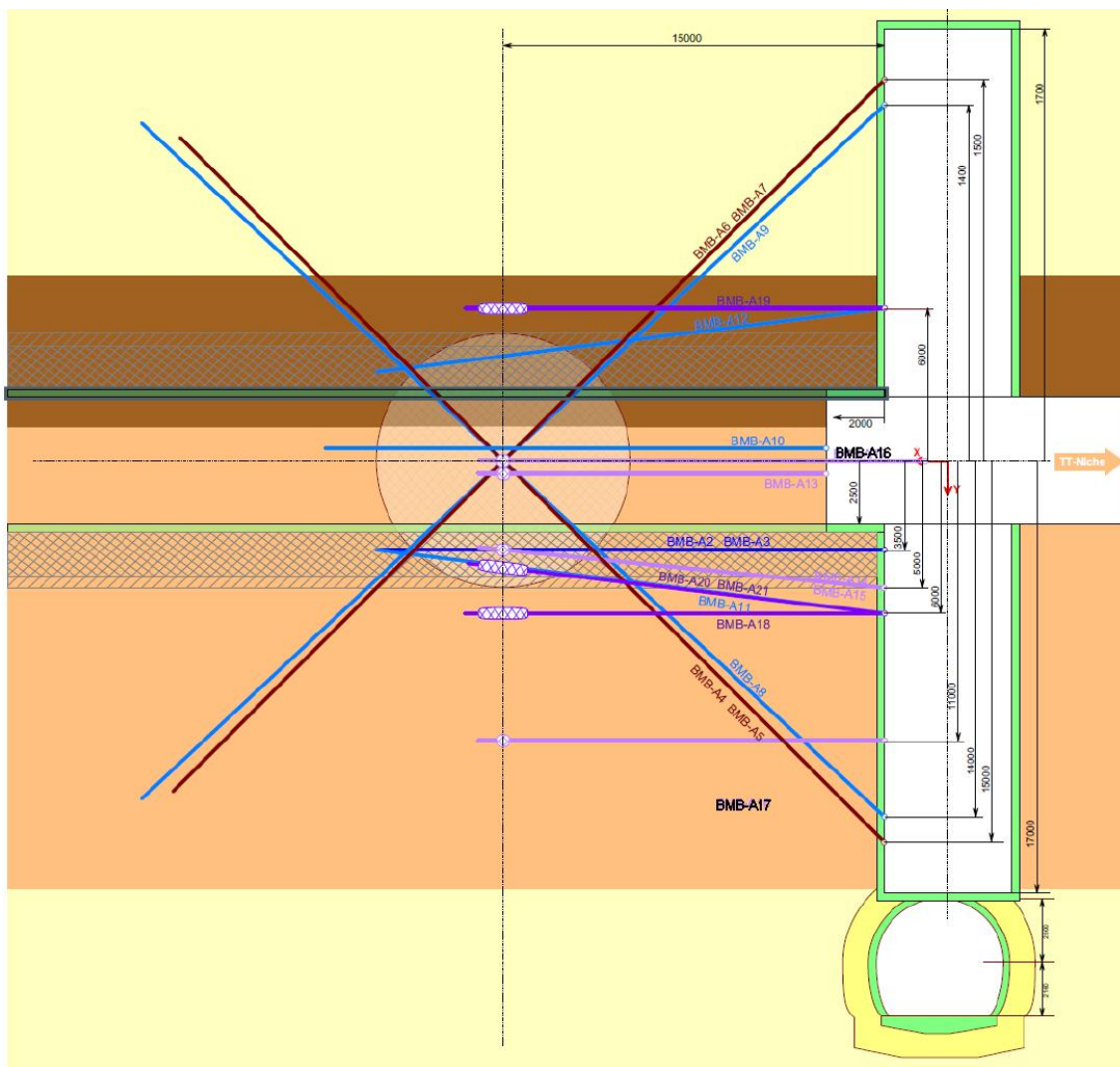
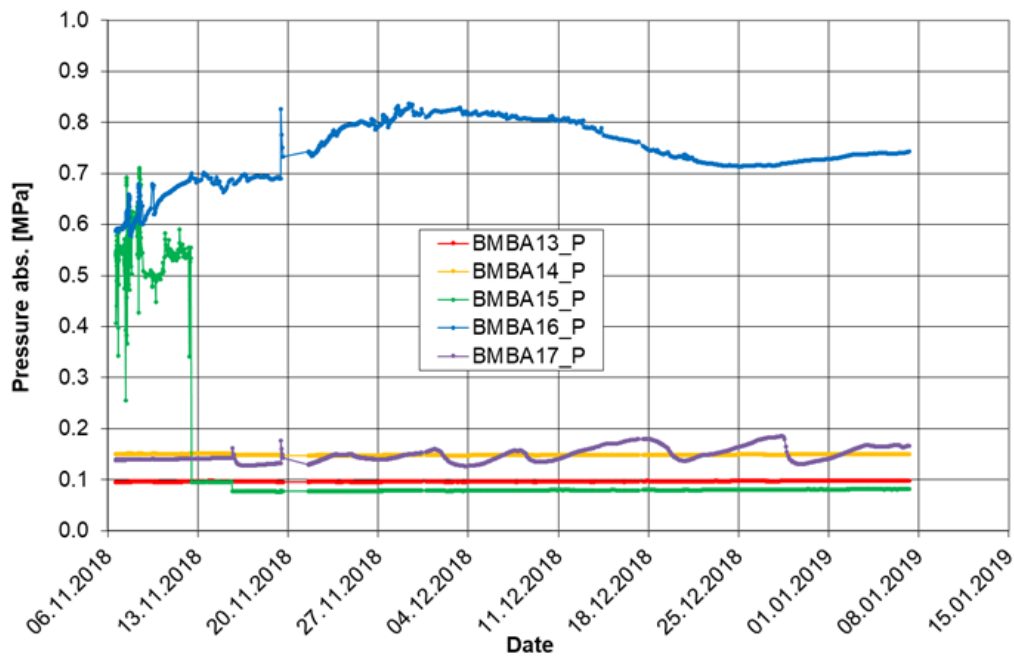


**Fig. 5.42** Plan view of the MB-A experiment area with the instrumentation boreholes /HES 18/

Drilling and instrumentation of GRS' minipiezometers had been planned for June 2018. Because of logistical problems (three drilling teams were active in the niches at the

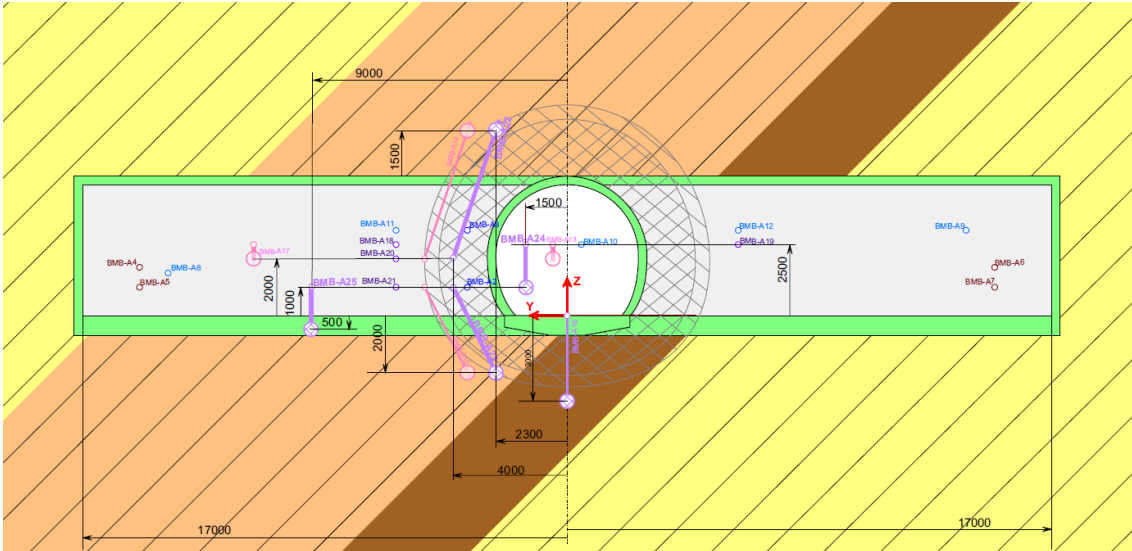
same time), only four of the five planned boreholes could be drilled, and the sealing of the boreholes with synthetic resin after minipiezometer installation had to be postponed. Drilling of the last borehole and borehole sealing was performed in September 2018.

Figure 5.43 shows the first measurement data of the five minipiezometers. One can see that only the last installed (and directly afterwards sealed) piezometer, BMB-A16, shows relevant pressure data, the others are at ambient pressure or slightly above.



**Fig. 5.43** First measurement data of the original set of piezometers

In order to resolve this issue, a set of replacement boreholes were planned and drilled in February 2019. The Figures 5.44 – 5.46 show the locations of the original and the replacement piezometer boreholes in different aspects.



**Fig. 5.44** Original and replacement piezometer boreholes – front view /HES 19/

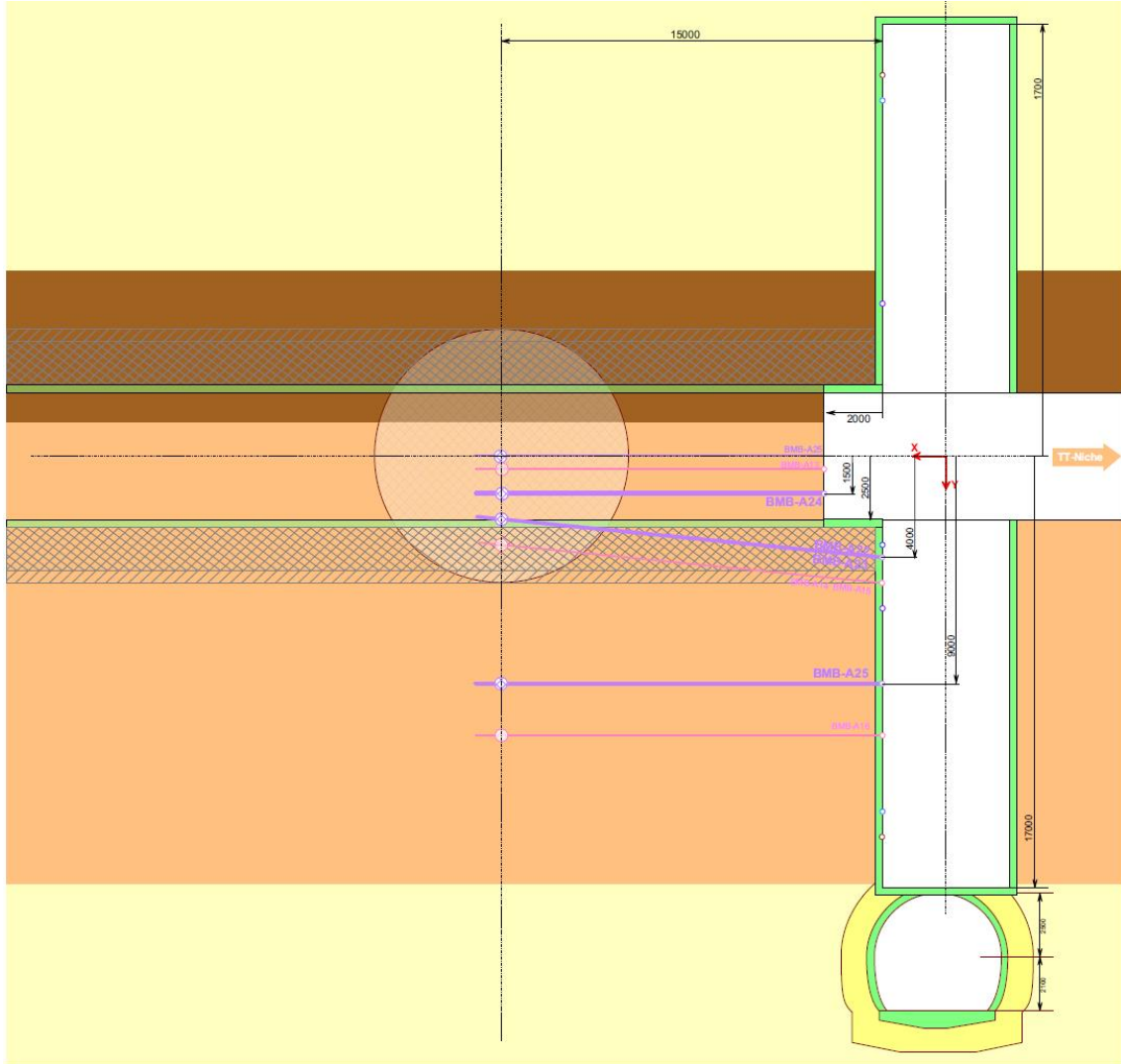


**Fig. 5.45** Original and replacement piezometer boreholes – plan view /HES 19/

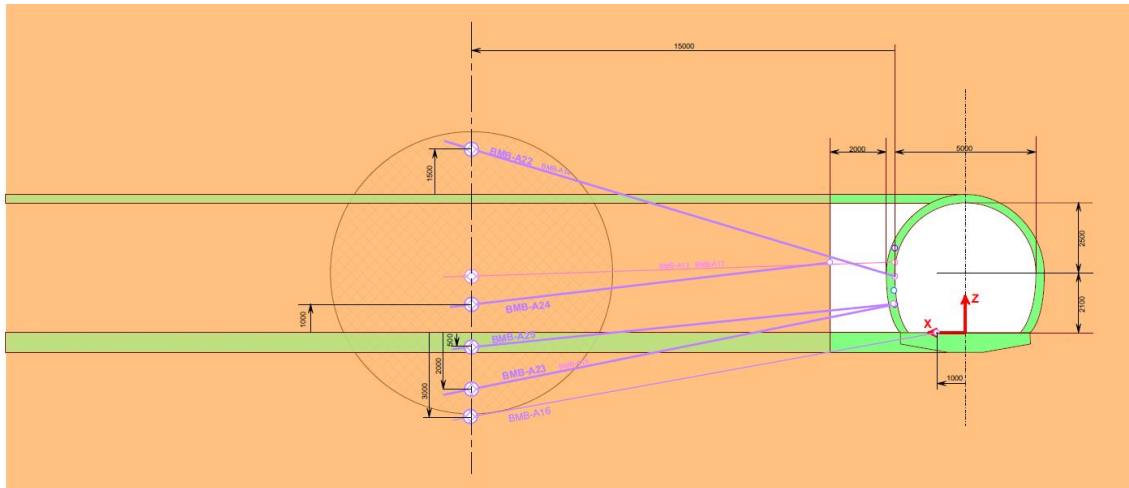


**Fig. 5.46** Original and replacement piezometer boreholes – side view /HES 19/

Three replacement boreholes were drilled (BMB-A23 – BMB-A25). The envisaged borehole BMB-A22 had to be cancelled because of problems sealing upward slanted boreholes. In the end, the following piezometers had been installed:

- BMB-A13: In the face of Gallery 18. Untight, dumped.
- BMB-A14: Slanted upward. Unreliable, very low pressure.
- BMB-A15: Slanted downward. Low pressure.
- BMB-A16: Slanted downward below Gallery 18. Plausible pressure.
- BMB-A17: Sub-horizontal, reference, 10 m from Gallery 18. Incomplete sealing, dumped.
- BMB-A23: Slanted downward, replacement for BMB-A15. Plausible pressure.
- BMB-A24: Moderately slanted downward in the face of Gallery 18, replacement for BMB-A13. Low pressure.
- BMB-A25: Moderately slanted downward, reference, 8 m from Gallery 18, replacement for BMB-A17. Plausible pressure.

All replacement boreholes were sealed directly after drilling and instrumentation. They were all tight, too, and at least two of them (BMB-A23 and BMB-A2) showed plausible pressures above 1 MPa four weeks after installation.

### 5.2.6.2 Monitoring results

In April 2019, excavation of Gallery 18 (Fig. 3.3) was stopped at a distance of the tunnel face of about 30 m to the niches CS-D and SW for four weeks, so that the measuring cross section (15 m in front of the niches) was in the middle between the niches and the tunnel face. The idea was to let all sensors equilibrate at the current situation, before the actual mine-by test was started. Then, from May 6 to May 27, 2019, the last part of Gallery 18 was excavated and the hydro-mechanical response of the rock was monitored.

Figure 5.47 shows the data measured by the minipiezometers during the excavation. At the start of the mine-by test, three of the minipiezometers show pressures of 1.5 MPa (BMB-A16 and BMB-A25) or 1 MPa (BMB-A23). When the excavation front draws near, all three react with an increase of pore pressure, which is caused by stress redistributions as a consequence of mining (after removal of part of the rock, the load on the remaining rock increases). BMB-A16 and BMB-A23, which are located close to the new-mined tunnel, react very distinctly on each excavation step. The reaction of BMB-A25 is less pronounced, since this minipiezometer is farther away (8 m) from Gallery 18.

One day after the excavation front has reached the measuring cross section 15 m from the niches, on May 17, the pressure at BMB-16 starts to decrease as a consequence of unloading and, probably, excavation damage. Unfortunately, the data acquisition system stopped working in the evening of this day due to a Microsoft Windows update problem. Data acquisition was resumed only in the morning of May 20. Therefore, the peaks of BMB-A23 and BMB-A25 could not be observed. After May 20, the pressures measured close to Gallery 18 decrease gradually to atmospheric values, while the pressure far from the Gallery decreases to the initial undisturbed value of 1.5 MPa.

The pressures measured at the minipiezometers starting at low pressure (BMB-A14, BMB-A15, and BMB-A24) are shown separately in Fig. 5.48. The minipiezometer in the upward slanted borehole BMB-A14 shows no usable signal – here, sealing of the borehole had proven very problematic.

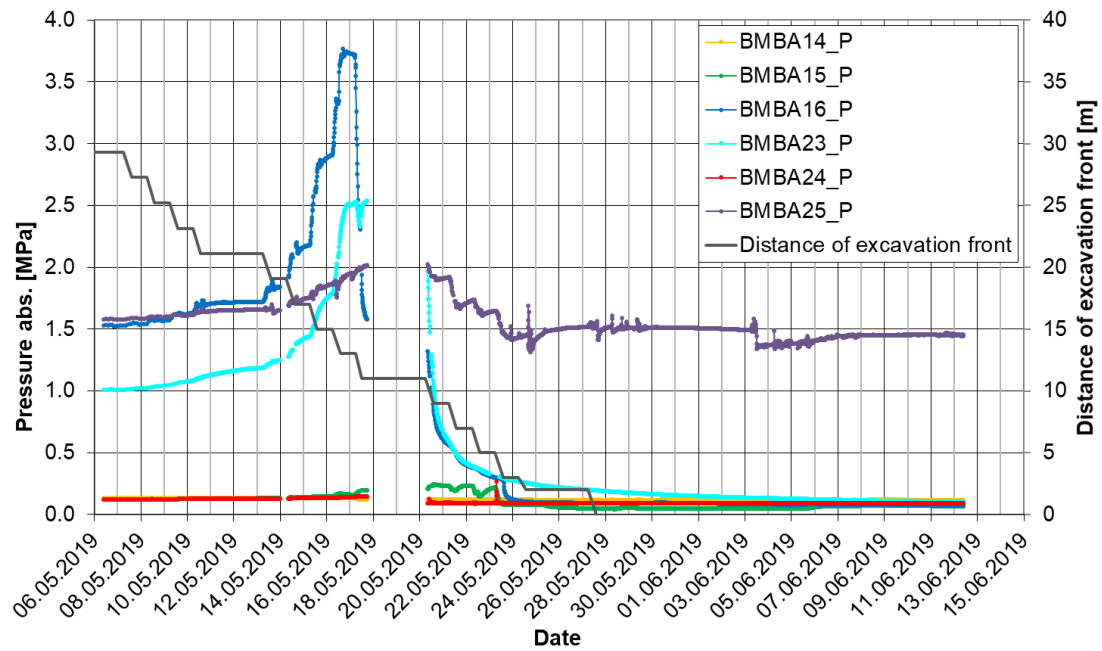


**Fig. 5.47** Pore pressure evolution as measured by the MB-A minipiezometers. Grey step curve: distance of excavation front from the niches (right scale)

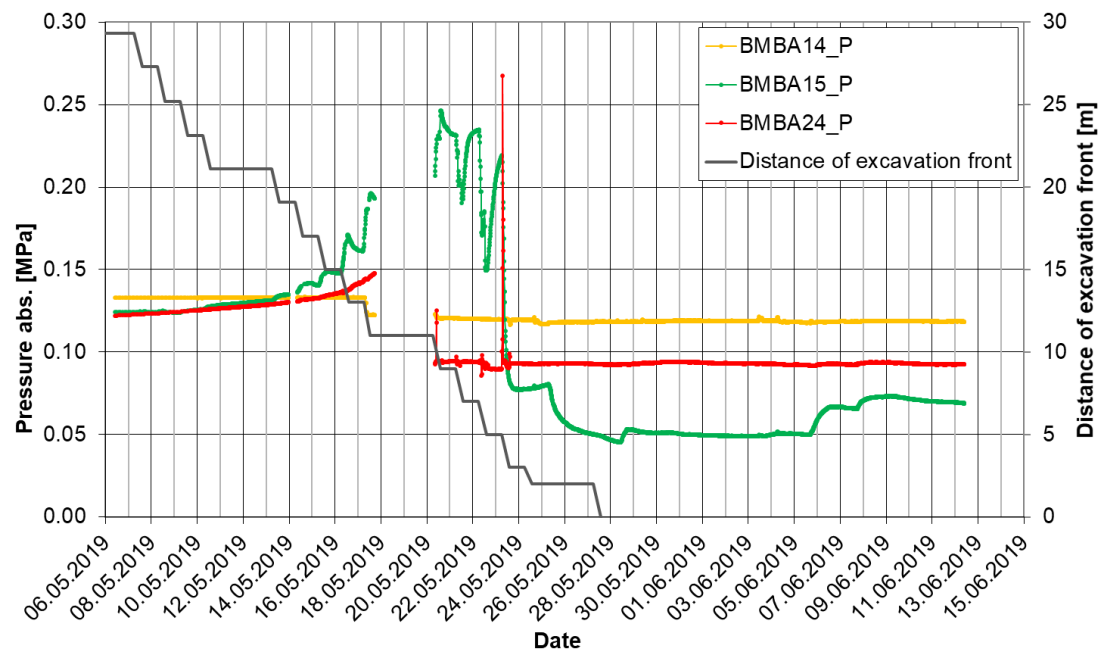


**Fig. 5.48** Pore pressure evolution as measured by BMB-A14, BMB-A15, and BMB-A24. Grey step curve: distance of excavation front from the niches (right scale)

BMB-A15 is close to BMB-A23 (which was its replacement) and shows a comparable signal at a lower scale. The pressure steps during approach of the excavation front are recognizable, the pressure peaks and the final decrease, however, come later than at BMB-A23. This may be explained by the fact that BMB-A15 is nearly 1 m farther away from Galley 18 (see Fig. 5.44). After the excavation, a pressure below ambient pressure is measured. This means there is no hydraulic shortcut to the gallery, and the piezometer is tight. Pressure goes into suction because of the mechanical unloading after excavation.

BMB-A24 is located in the tunnel face and shows a small gradual pressure increase with the approach of the excavation front. After the data loss of the weekend of May 18/19, the measurement is at ambient pressure because the minipiezometer was cut off by the excavation as planned.

Interpretation of all the data collected during the MB-A experiment needs coupled hydro-mechanical simulation of the experiment. Respective work is in preparation.

On May 27 excavation reached the niches CS-D and SW, and Gallery 18 of the MTRL was completed (Fig. 5.49).



**Fig. 5.49** Cutting through of Gallery 18, May 27, 2019



## 6 Model simulation

In this chapter, the model simulations performed for HE-E and FE are presented. In the first section the adaptation of the Virtus virtual underground laboratory to the MTRL is described. Virtus was used for setting up the HE-E and FE models.

Simulations performed for DM-A have been reported earlier /ZHA 14/. MB-A interpretative simulations are currently planned.

### 6.1 Virtus adaptation

Between 2010 and 2014, the prototype „Virtual Underground Laboratory in Rock Salt” (Virtus) was developed by a consortium of GRS, BGR, and DBE TECHNOLOGY and implemented by the subcontractor Fraunhofer IFF /WIE 14b/. The project was funded by the German Federal Ministry of Economics and Energy under contract no. 02E10890.

In combination with the specific existing simulation codes, Virtus provides a powerful tool for simulating and visualizing the coupled thermo-hydro-mechanical processes occurring in a repository or underground laboratory in the context of geology and mine structure. Additionally, it is meant to provide a tool for effectively planning and checking repository layouts within the potentially complicated geologic structures. Virtus combines a powerful visualization software for geologic models and result data from numerical simulations with functions for management of material and project data. Thus, Virtus is a software platform and data hub at the same time.

The functionality of Virtus includes /WIE 14b/

- Import and processing of geologic models, with extensive testing and repairing tools for potentially defective geometries
- Import or construction of mine structures (as independent models)
- Combination of geology and mine structure to a composite model suited as input for simulation calculations
- Creation of model sections and export to simulation codes
- Material data base

- Import and visualization of simulation results in the geologic/mine structure model

Although Virtus was developed for rock salt as the host formation, the possibility to use it with other types of rock was one of the design criteria. Because of its potential to facilitate the development of realistic geometrical models for simulating Mont Terri experiments, it was adapted for use with the MTRL. The work performed included the import of the Mont Terri geological model and the detailed laboratory structure (both provided by Swisstopo), visualization improvements and adaptations, improvements in the definition of sections for modelling, and finally the creation of model sections for the HE-E and FE experiments, including the model construction of heater, buffer, and seal structures of the two experiments. The work was performed in cooperation with the contractor Fraunhofer IFF as the Virtus implementer.

Figure 6.1 shows the MTRL laboratory structure imported into Virtus. The data delivered by Swisstopo are laser-scan data, so that a realistic and detailed representation of the geometrical structure is achieved.

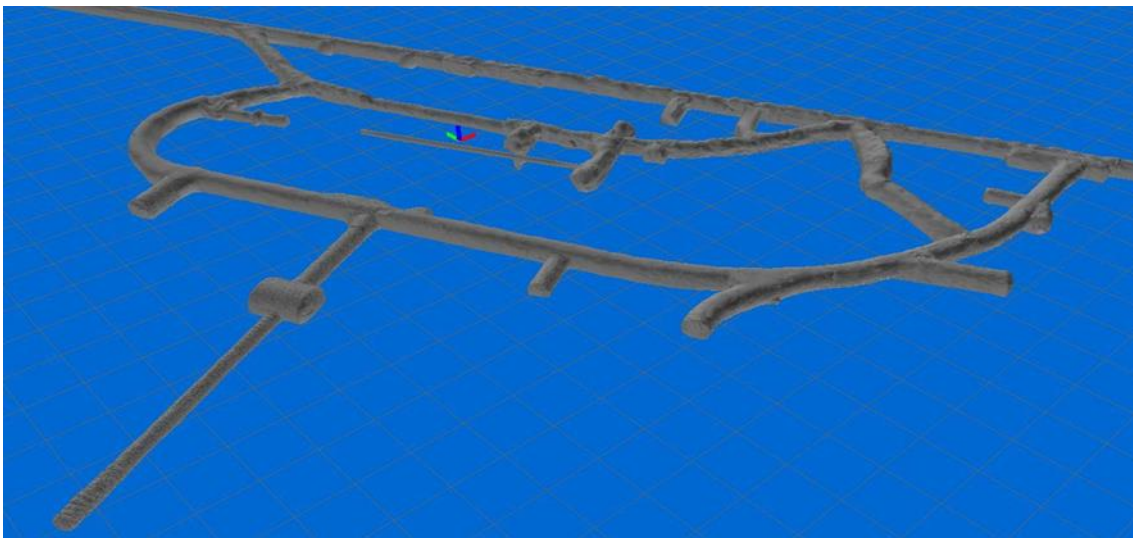


**Fig. 6.1** Geometrical structure of the MTRL (Virtus representation)

The geologic model provided by Swisstopo was an updated simplified model. The shaly facies and the sandy facies are included, but no distinction was made between the sandy facies and the carbonate-rich sandy facies. The Virtus model includes the neighbouring formations and the surface topography. Figure 6.2 shows the geologic model in Virtus (compare geologic cross section of Fig. 3.4). The geologic units

mapped on the laboratory structure are shown in Fig. 6.3. Figure 6.4 shows a part of the combined model of laboratory structure and geologic interfaces.

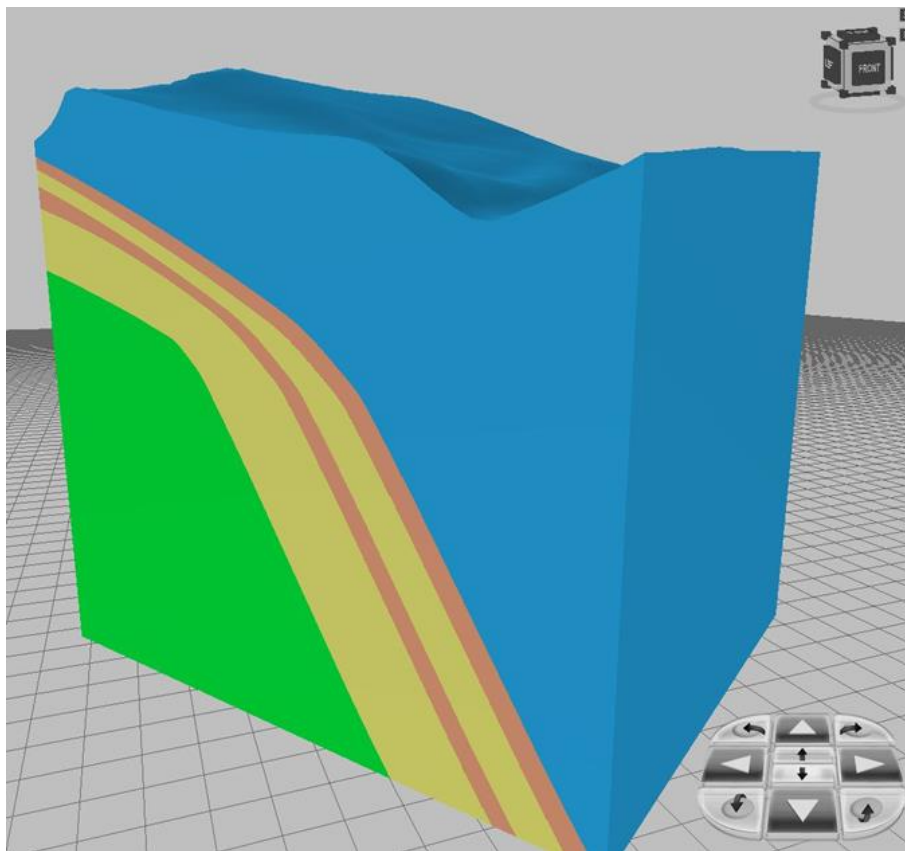


**Fig. 6.2** Simplified Mont Terri geology of Virtus (yellow: OPA shaly facies, brown: OPA sandy facies, green: Lias marl/limestone, blue: Dogger limestone)



**Fig. 6.3** Geology mapped on the laboratory structure

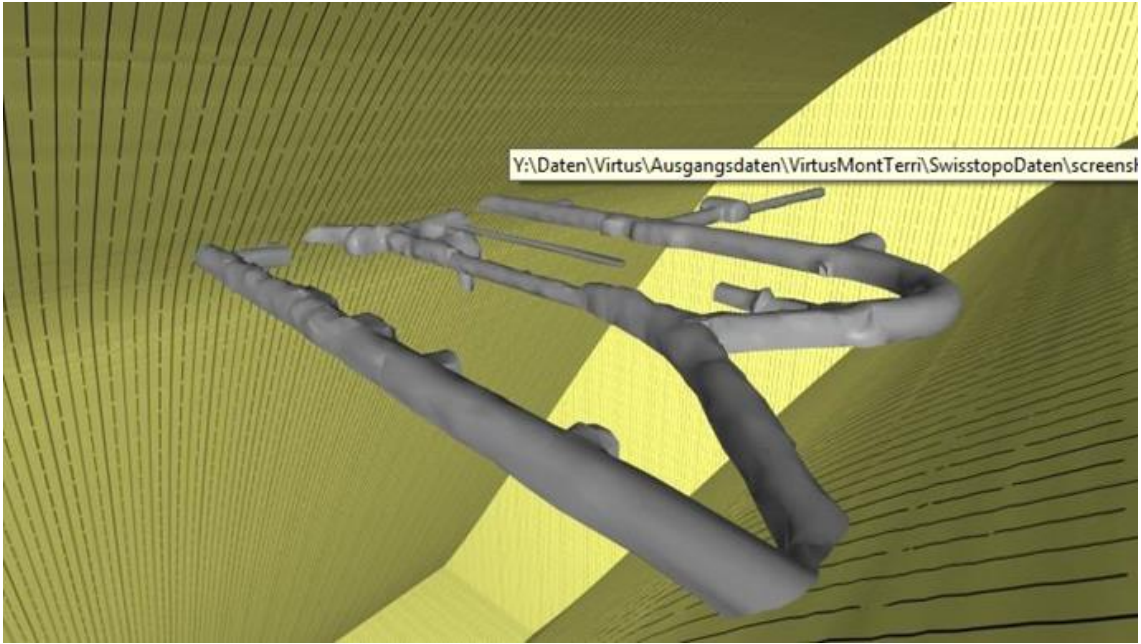


**Fig. 6.4** Combined model of laboratory structure and geologic interfaces

Virtus visualization improvements included the possibility of providing surface patterns to achieve a realistic look of the laboratory inside (Fig. 6.5).



**Fig. 6.5** View into the Virtus representation of the MTRL

To create model sections usable for simulation calculations of the HE-E and FE experiments, the heaters, buffer units (Bentonite blocks and granular buffer) and concrete seal structures were constructed in Virtus. For HE-E, a detailed representation of the heater interior proved necessary as well (see Section 6.2.1).

After this step, brick-shaped sections of the respective experiment region were defined and exported to the GiD code /GiD 18/ which is used as pre-/postprocessor for the Code\_Bright simulation tool /OLI 96, UPC 11/ used by GRS for THM calculations. In GiD, the finite element meshing of the models was performed (Fig. 6.6).

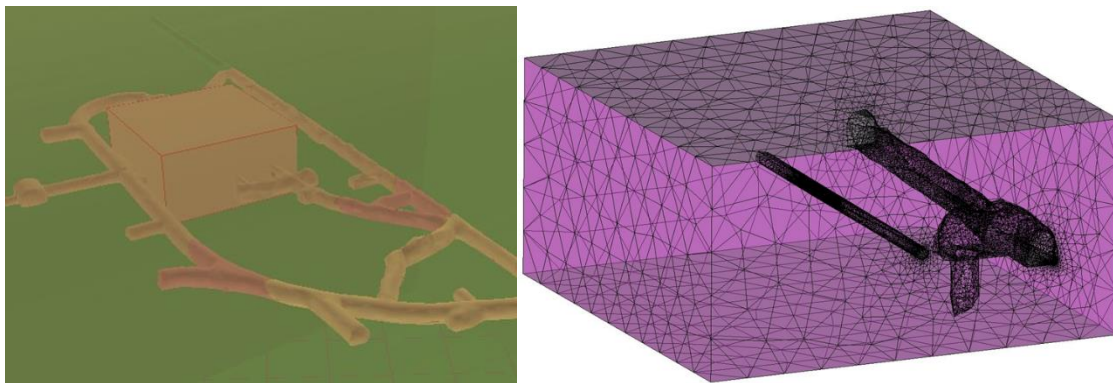


**Fig. 6.6** Definition of a brick-shaped section in Virtus for the export (left) and meshing of the section imported by GiD (right) for the example of HE-E

## 6.2 HE-E simulation

The HE-E was modelled already in the frame of PEBS, using various models /GAU 14/. In contrast to CIMNE using an axial-symmetric model, GRS used a two-dimensional plane strain model in order to be able to divide between the granular buffer and the bentonite blocks. Both approaches are problematic regarding the realistic representation of the actual geometry.

The idea of the three-dimensional HE-E simulations was to use a realistic geometry and approach the challenge by a set of calculations with increasing numerical complexity. As a first simulation step, a purely thermal calculation of the HE-E using the model shown in Fig. 6.6 was performed. The next step, a coupled thermo-hydraulic (TH) simulation with certain simplifications, is reported here in detail. For this simulation, the model had to be enlarged because of farther reaching pore pressure effects. The fol-

lowing steps, a non-simplified TH-coupled simulation and a fully coupled thermo-hydro-mechanical (THM) simulation, are still pending.

### **6.2.1 Geometrical model**

The full geometrical model used for the TH simulation is shown in Fig. 6.7. The model features the Opalinus clay shaly facies with the HE-E microtunnel and the parallel Gallery 98 including the HE-B test site with a large-scale vertical borehole, since these ventilated openings can be expected to have an influence on the pore pressure field. All openings are realistically represented using the laser-scan data included in Virtus.

Inside the microtunnel, the heater liner, bentonite blocks, granular bentonite and sand-bentonite, concrete plugs and rock wool thermal insulation between the two heaters were modelled (compare Fig. 5.3 and 5.6). It was also necessary to model the inside of the heaters (Fig. 6.8), because otherwise the effect of the higher thermal conductivity of the blocks compared to the granular buffer would not be visible – as discussed in Section 5.2.1.2, temperature on top of the liner is always higher than at the bottom. In Fig. 6.8, the heater liner is grey and the heating element is red. Inside the heating element and in the annulus between liner and heating element is air. Between the two heaters is the thermal insulation of rock wool (green).

The complete model had a size of 88 m x 48 m x 84 m (width by depth by height) and was meshed using GiD /GID 18/ with almost 42 000 nodes and 227 000 tetrahedra elements.

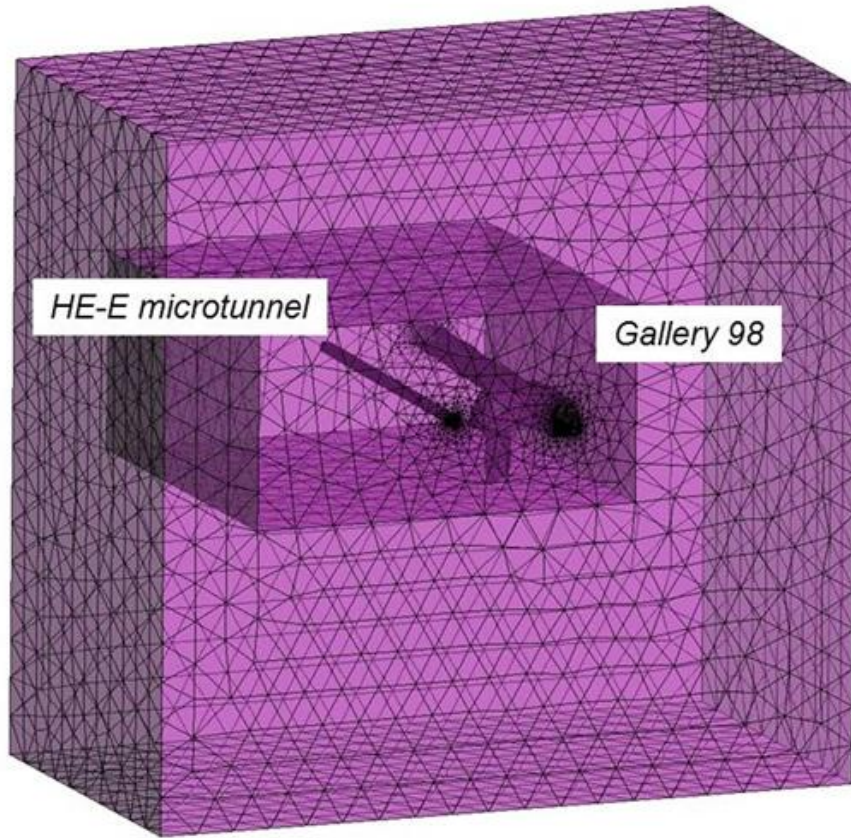


**Fig. 6.7** Geometrical model of the HE-E TH simulation

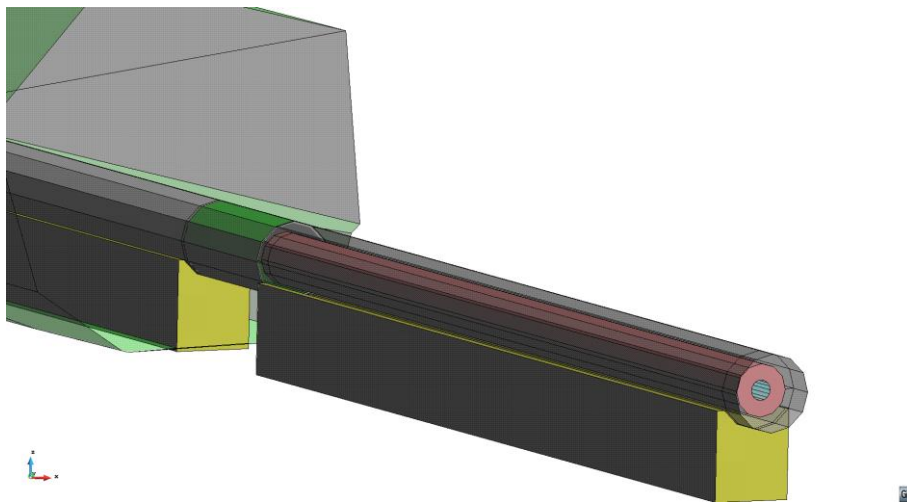


**Fig. 6.8** HE-E heater details as included in the HE-E model

## 6.2.2 Physical model

In the TH-coupled simulation, Code\_Bright /OLI 96, UPC 11/ solves the balance equations for fluid and energy, with the equilibrium restrictions of the psychrometric law for the concentration of vapour in air and Henry's law for the solubility of air in water.

The thermal part considers only conductive heat flow which is described by Fourier's law (eq. 6.1), connecting conductive heat flow  $i_c$  to the gradient of temperature  $T$  multiplied by the thermal conductivity  $\lambda$

$$i_c = -\lambda * \nabla T \quad (6.1)$$

Heat transfer through the air inside the heater (Fig. 6.8) is mainly achieved by thermal radiation. This is simulated by an increased thermal conductivity value for this air which is estimated from the geometry.

From the hydraulic point of view, it is assumed that liquid flow follows Darcy's law, with the actual effective permeability to each phase given by the product of intrinsic and relative permeability. The dependence of intrinsic permeability  $k$  on porosity  $\phi$  (eq. 6.2) is given by

$$k = k_0 * \frac{\phi^3}{(1 - \phi)^2} * \frac{(1 - \phi_0)^2}{\phi_0^3} \quad (6.2)$$

with initial values  $k_0$  and  $\phi_0$ . The relative permeability of the liquid phase is dependent on the degree of liquid saturation (eq. 6.3), where  $S_r$ ,  $S_{lr}$ ,  $S_{ls}$ ,  $S_e$  are the actual, residual, maximum, and effective saturation of liquid, respectively.  $A$  and  $\beta$  are parameters. Gas pressure is assumed to be atmospheric all the time, which means that gas is moving freely through the system.

$$S_e = \frac{S_r - S_{lr}}{S_{ls} - S_{lr}} \quad \text{with} \quad k_{rl} = A * S_e^\beta \quad (6.3)$$

It is necessary to define the retention curve of the materials that relates the degree of saturation to suction pressure (suction pressure is the independent variable in Code\_Bright; saturation is a function of suction pressure). Generally, the formulation of van Genuchten with material parameters  $\mu$ ,  $P_0$  and  $\sigma_0$  is selected (eq. 6.4).

$$S_e = \left[ 1 + \left( \frac{P_g - P_l}{P} \right)^{1/(1-\mu)} \right]^{-\mu} \quad \text{with} \quad P_g - P_l \geq 0 \quad \text{and} \quad P = P_0 * \frac{\sigma}{\sigma_0} \quad (6.4)$$

$P_0$  is the pressure measured at a certain temperature, and  $\sigma_0$  is the related surface tension.

For the sand-bentonite material, however, a square law for the retention curve of the form

$$S_e = \left[ 1 + \left( \frac{P_g - P_l}{P_0} \right) \right]^{-1/2} \quad (6.5)$$

was chosen, as it provided a better fit of data measured in the laboratory /WIE 14a/ for the relevant saturation range.

The molecular diffusion of vapour is governed by Fick's law (eq. 6.5), a constant dispersion coefficient corresponding to the molecular diffusion of vapour in air is assumed.  $P_g$  is given in MPa. For the tortuosity  $\tau$  a value of 1.0, for  $n$  a value of 2.3 and for  $D$  a value of  $5.9 \cdot 10^{-6}$  m<sup>2</sup>/s are adopted.

$$D_m^w = \tau D * \left( \frac{(273.15 + T)^n}{P_g} \right) \quad (6.6)$$

In the simulation presented here, two simplifications were introduced:

- Evaporation of water was suppressed. It is understood that near to the heaters the high temperature will lead to evaporation. This was, however, not considered at the present stage in order to reduce numerical complexity.
- The thermal conductivity is assumed constant for all materials, although it is highly dependent on saturation for the buffer materials. This is done because saturation inside the buffer body has remained very low throughout the experiment (see Section 5.2.1.2). The chosen thermal conductivities for these materials represent the "dry" low saturation values.

### 6.2.3 Material data and initial parameters

The material data of the Opalinus clay and the buffer materials are given in Table 6.1. Table 6.2 shows the data of the other materials present in the HE-E model. For all materials, the same parameters for the relation between saturation and relative permeability (eq. 6.3) were chosen as  $A = 1$  and  $\beta = 3$ .

**Tab. 6.1** Material data of Opalinus clay and buffer materials

		OPA Shaly Facies	Granular bentonite	Sand-Bentonite	Bentonite blocks	Unit
Solid Phase Density	$\rho_s$	2700	2700	2546	2700	kgm <sup>-3</sup>
Thermal Conductivity	$\lambda$	1.3	0.3	0.3	0.8	WmK <sup>-1</sup>
Solid Phase Specific Heat	c	995	893	775	1058	Jkg <sup>-1</sup> K <sup>-1</sup>
Retention Curve	$P_0$	12	10	0.7	21.9	MPa
	$\sigma_0$	0.072	0.072		0.072	Nm <sup>-1</sup>
	$\mu$	0.3	0.4		0.3	
	$S_{lr}$	0.01	0.01	0.01	0.01	
	$S_{ls}$	1.0	1.0	1.0	1.0	
	$\Phi_0$	0.137	0.45	0.47	0.33	
Intrinsic Permeability	$k_0$	2.00E-20	3.50E-20	1.20E-13	2.50E-21	m <sup>2</sup>

**Tab. 6.2** Material data of technical components

		Concrete	Steel	Rockwool	Air*	Unit
Solid Phase Density	$\rho_s$	2650	7850	70	1.293	kgm <sup>-3</sup>
Thermal Conductivity	$\lambda$	0.5	52	0.04	0.251	WmK <sup>-1</sup>
Solid Phase Specific Heat	c	1000	440	1000	1005	Jkg <sup>-1</sup> K <sup>-1</sup>
Retention Curve	$P_0$	1.5e+7	1.0e+6	1.0e+4	1.0e+6	MPa
	$\sigma_0$	0.072	0.072	0.072	0.072	Nm <sup>-1</sup>
	$\mu$	0.31	0.3	0.3	0.3	
	$S_{lr}$	0.01	0.01	0.01	0.01	
	$S_{ls}$	1.0	1.0	1.0	1.0	
	$\Phi_0$	0.15	0.001	0.5	0.001	
Intrinsic Permeability	$k_0$	1.00E-20	1.00E-25	1.00E-14	1.00E-25	m <sup>2</sup>

\* with increased thermal conductivity to account for heat radiation inside the heater liner

The material parameters for Opalinus clay, the buffer materials, concrete, and steel were taken from the PEBS material database that was generated for the simulations performed in the PEBS project /GAU 14, WIE 14a/.

Rock wool and air inside the heater liner had not been modelled in PEBS. Retention curves for these materials are not available and had to be chosen, but since both materials remain dry all the time, their hydraulic parameters are not relevant. Important are only their thermal parameters.

The initial conditions of the simulation are summarised as follows (initial porosities are included in Tab. 6.1 and Tab. 6.2):

- Initial temperature: 14 °C
- Initial pore-water pressure of the Opalinus clay (before excavation of microtunnel and Gallery 98): 1.75 MPa
- Initial suction of granular bentonite: -118 MPa (corresponding to an initial saturation of 45 %)
- Initial suction of sand-bentonite mixture: -60 MPa (corresponding to an initial saturation of 24 %)
- Initial suction of bentonite blocks: -58 MPa (corresponding to an initial saturation of 63 %)
- Initial suction of concrete: -5 MPa (almost saturated)

#### **6.2.4 Schedule and boundary conditions**

The simulation schedule is shown in Table 6.3, starting with the excavation of the microtunnel and Gallery 98 (see Fig. 6.7). Modelling of the 12 years between excavation and installation of the HE-E is needed to achieve a realistic pore pressure distribution around the microtunnel at the start of the HE-E. The very complicated ventilation history of the VE /MAY 07/ was, however, not reproduced. Instead, a constant ventilation simulated by a suction of -2 MPa on the excavated surfaces was applied for the whole time.

The open-tunnel phase was followed by installation of the HE-E and, after a short isothermal phase, applying realistic temperature boundary conditions corresponding to the actual thermal load phases (compare Section 5.2.1) on the heater surfaces. Note that the temperature boundary condition is on the heater element and not on the liner. The heater temperatures are considerably higher than the liner temperatures.

**Tab. 6.3** Schedule and conditions of the HE-E coupled TH simulation

Interval	Time [d]	Event / Conditions
1	0 – 100	<ul style="list-style-type: none"> <li>Initial conditions: <math>T = 14 \text{ }^\circ\text{C}</math>; <math>P_i = 1.75 \text{ MPa}</math></li> <li>Excavation of Gallery 98 and microtunnel</li> </ul>
2	100 – 4474	<ul style="list-style-type: none"> <li>Time between excavation and HE-E installation, including the time before, during, and after the ventilation experiment (VE)</li> <li>Simplified boundary condition: -2 MPa suction on the excavated surfaces simulating ventilation</li> </ul>
3	4474 – 4484	<ul style="list-style-type: none"> <li>Installation of the HE-E experiment</li> <li>Removal of ventilation boundary condition in the installed part of the microtunnel</li> </ul>
4	4484 – 4505	<ul style="list-style-type: none"> <li>Isothermal phase</li> </ul>
5	4505 – 4507	<ul style="list-style-type: none"> <li>Heating phase for system calibration (<math>T_{\text{start}} = 14 \text{ }^\circ\text{C}</math>, <math>\Delta T = 2 \text{ }^\circ\text{C}</math>, <math>T_{\text{end}} = 16 \text{ }^\circ\text{C}</math>)</li> </ul>
6	4507 – 4600	<ul style="list-style-type: none"> <li>First heating phase (<math>T_{\text{start}} = 16 \text{ }^\circ\text{C}</math>, <math>\Delta T = 94 \text{ }^\circ\text{C}</math>, <math>T_{\text{end}} = 110 \text{ }^\circ\text{C}</math>)</li> </ul>
7	4600 – 4869	<ul style="list-style-type: none"> <li>Second heating phase (<math>T_{\text{start}} = 110 \text{ }^\circ\text{C}</math>, <math>\Delta T_B = 80 \text{ }^\circ\text{C}</math>, <math>T_{\text{end B}} = 190 \text{ }^\circ\text{C}</math> (granular bentonite section); <math>\Delta T_{SB} = 70 \text{ }^\circ\text{C}</math>, <math>T_{\text{end SB}} = 180 \text{ }^\circ\text{C}</math> (sand-bentonite section))</li> </ul>
8	4869 – 5599	<ul style="list-style-type: none"> <li>Constant heater temperature (<math>T_{\text{Bentonite}} = 190 \text{ }^\circ\text{C}</math>; <math>T_{\text{Sand-Bentonite}} = 180 \text{ }^\circ\text{C}</math>)</li> </ul>

### 6.2.5 Results

Figure 6.9 shows the calculated steady-state temperature distribution on the heater liner in the sand-bentonite section during heating phase 3. For comparison, the measured temperature curves at the liner centre, above and below the heater, are shown, too. One can see that with the detailed model of the heater (Fig. 6.8) a realistic liner temperature distribution with higher temperatures on top of the liner is achieved. This is true for both buffer sections.

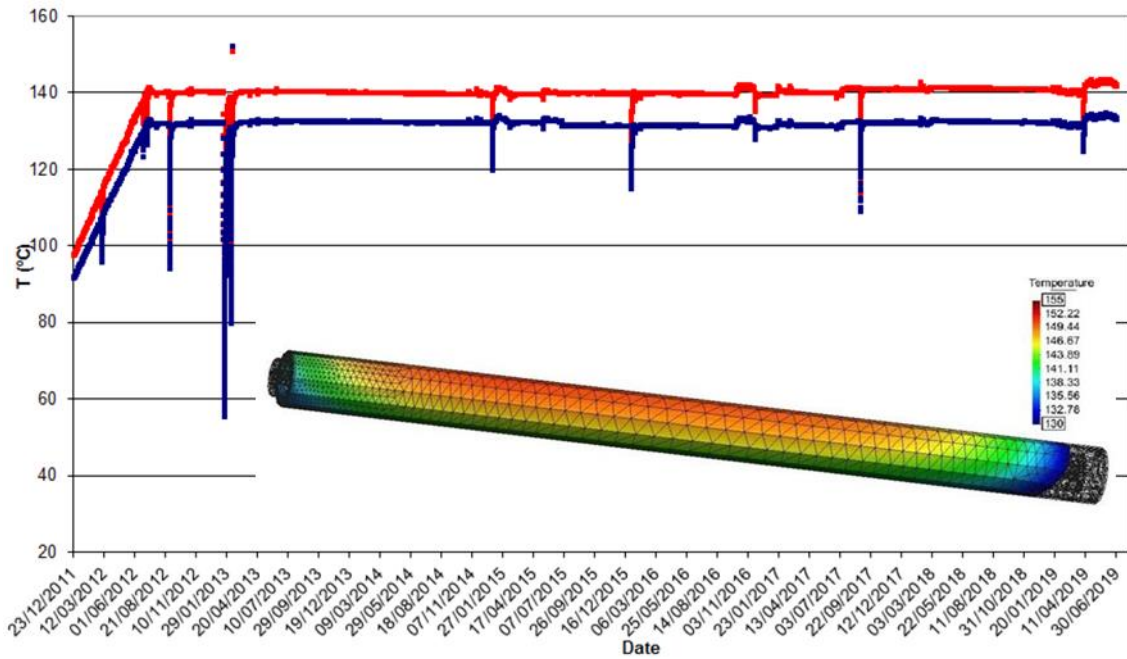


**Fig. 6.9** Liner temperature measured at the centre top and bottom of the heater (red and blue curves) and calculated liner temperature during heating phase 3 (surface plot)

Temperature results of different simulations for the granular buffer are compared in Fig. 6.10, again on the example of the sand-bentonite buffer. The symbols in Fig. 6.10 represent the measured values in the heater midplane at different distances above the heater (compare Fig. 5.10).

The continuous lines show the temperatures as calculated by the 2-dimensional plane-strain simulation performed in the PEBS project /WIE 14/. This calculation overestimated temperatures considerably – a well-known problem caused by inevitable neglect of the axial heat flow component. The dotted lines are results of a purely thermal simulation with the three-dimensional model and exhibit a significant improvement, although there are still deviations close to the heater (measurement location “Center”, pink lines). A further improvement is achieved with the coupled TH simulation using the enhanced 3D model. This is shown only for the measurement location “Center” close to the heater which perfectly fits the measured data, but it holds also for the other locations.

Temperature results for the granular bentonite section (not shown here) are comparable.

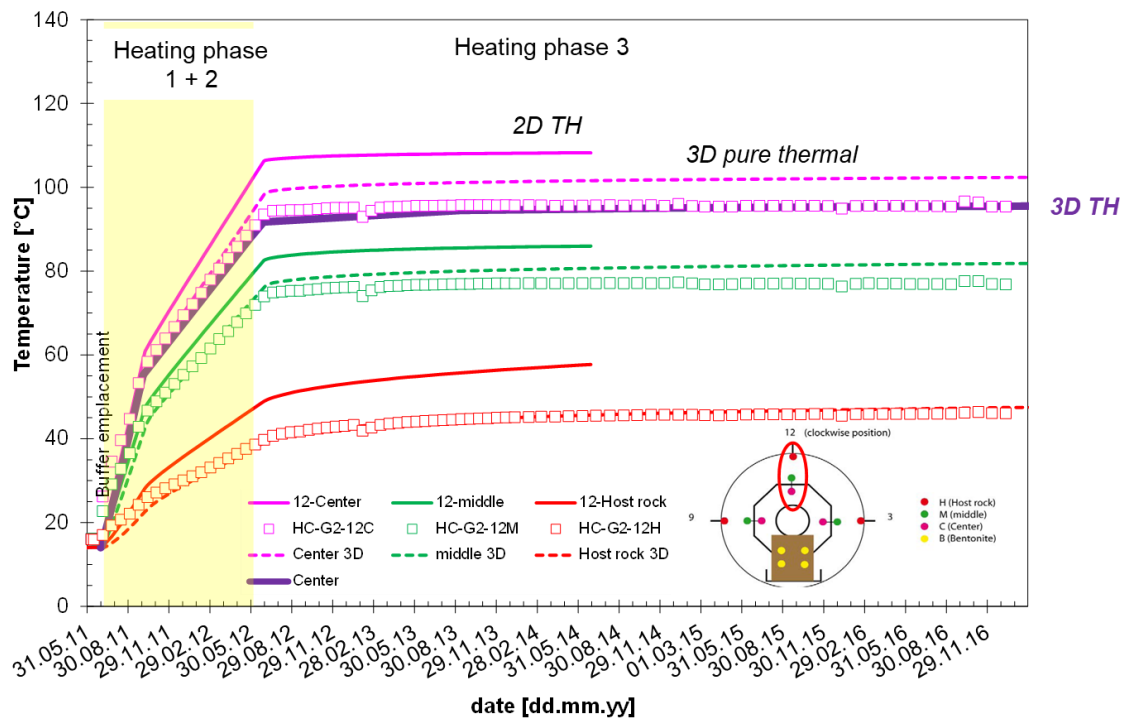


**Fig. 6.10** Temperature measured in the granular sand-bentonite buffer (symbols) and corresponding calculated temperatures (continuous lines: 2D plane strain TH simulation, dotted lines: 3D pure thermal simulation, purple line: 3D coupled TH simulation result)

While temperature data are perfectly simulated by the coupled TH simulation, this is not the case for the buffer saturation evolution (Fig. 6.11). In the model, saturation is increasing steadily with time in both sections. Saturation is higher in the granular bentonite section due to a higher initial saturation (see Section 6.2.3), and it increases faster due to the different retention curve (higher suction). The buffer drying observed in both sections (see Figs. 5.12 and 5.13) is not reproduced at all.

The reason for this deviation from the observed behaviour is the simplification of suppressing evaporation of water. Thus, all water remains in the liquid phase and there is no driving force that moves water away from the heaters. This flaw does not affect the temperature distribution because a thermal conductivity increase with increasing saturation was also neglected.

The next simulation step should therefore be to include evaporation in the model. First respective tests have resulted in numerical convergence problems. Once these are overcome, more realistic results on buffer re-saturation can be expected.

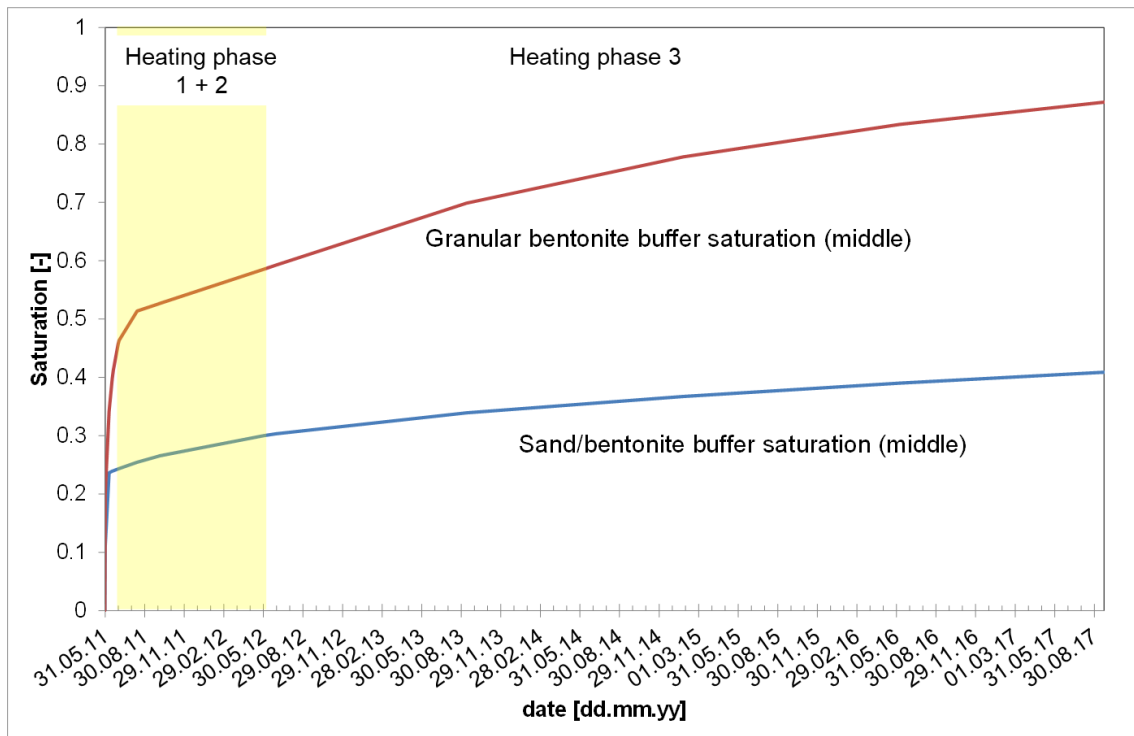


**Fig. 6.11** Simulation results for saturation evolution in the centre of the granular bentonite buffer and the sand-bentonite buffer

An enhanced TH simulation will still neglect important features of the buffer materials, since mechanical effects, especially swelling of the bentonite materials with re-saturation, cannot be reproduced. Therefore, the last simulation step envisaged is a THM coupled simulation. Since this will increase the number of degrees of freedom significantly – from two (temperature and liquid pressure) in the TH simulation to five (T, p plus three displacement directions) – the numerical effort will be considerable, and tests with less complex models are indispensable.

### 6.3 FE-M modelling

In analogy to the procedure for HE-E simulation, the geometrical model of the FE experiment was constructed in Virtus and exported to GiD. The model includes the FE cavern and tunnel as given by laser-scan data, the concrete invert, bentonite block pedestals, heated containers, granular buffer, and concrete plug, but not yet the concrete lining of the walls and roof. The full model is a cube of 50 m side length (Fig. 6.12) and was meshed with about 37 800 nodes and 210 000 tetrahedra elements. Figure 6.13 shows the FE cavern and the FE tunnel with the containers on the pedestals.

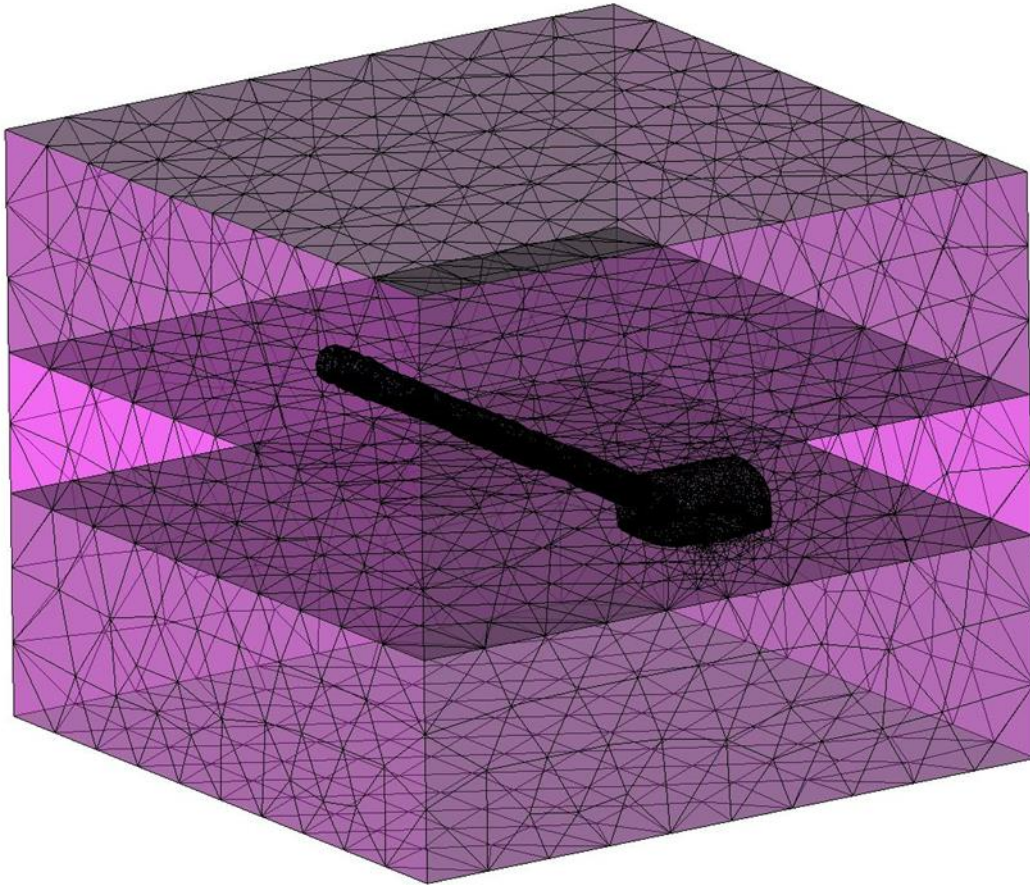


**Fig. 6.12** Geometrical model of the FE-M (complete mesh)

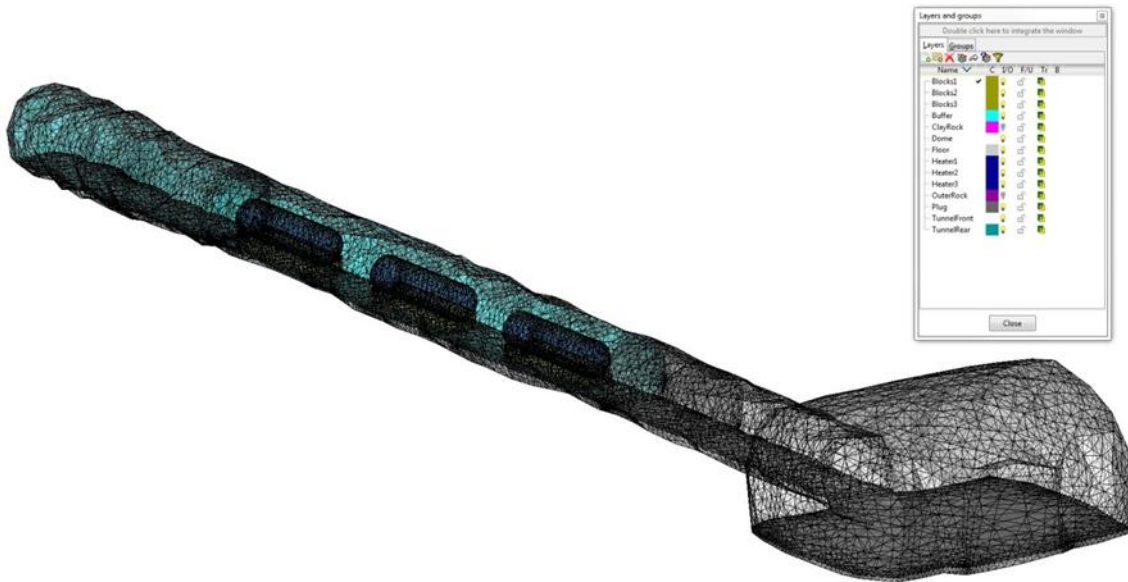


**Fig. 6.13** Geometrical model of the FE-M: Detail showing the FE cavern, FE tunnel, and heated containers on bentonite blocks

For now, only an orientating thermal simulation has been performed. For this task, the material data and heating schedule of HE-E were used with a temperature boundary condition of 140 °C on the containers' surfaces – although this is not entirely realistic, it is sufficient for finding out flaws in the geometry and meshing. As an exemplary result, the temperature distributions after 10 years of heating near the containers and in the tunnel floor are shown in Fig. 6.14.

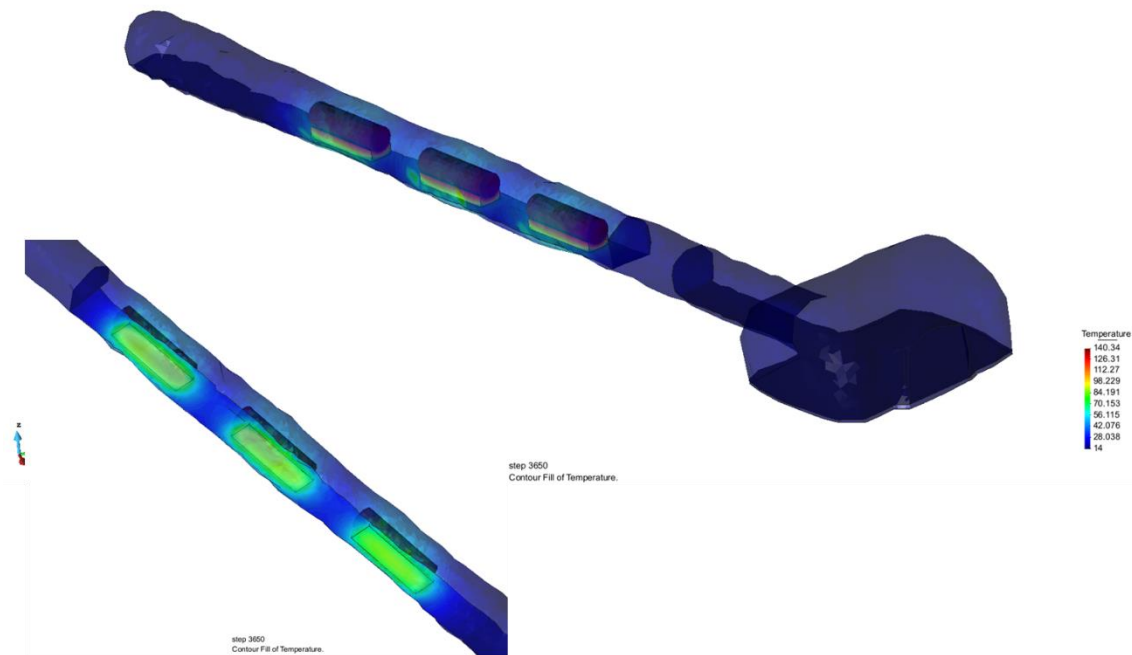


**Fig. 6.14** Simulated temperature distributions near the containers and in the tunnel floor after 10 years of heating

For further coupled simulations which are planned in the frame of a Decovalex modeling task, some modifications of the current model are needed:

- The model of the tunnel has to be divided into different sections to enable a sequential tunnel excavation.
- The shotcrete lining of the tunnel has to be added.



## 7 Conclusions and future work

In this report, GRS' in-situ research work at the MTRL and related model calculations between 2014 and 2019 are presented. The work performed includes participation in large-scale repository simulation experiments (HE-E, FE) as well as investigation of Opalinus clay hydro-mechanical behaviour (DM-A, SB-A, MB-A) and characteristics (DB).

Both the HE-E and FE experiments have been started before the reporting period and have already produced a huge amount of reliable data. They continue to run without major problems, and in spite of their long duration, loss of sensors is limited.

A problem regarding the HE-E is the very low pore-water pressure in the surrounding rock, which has the effect that no significant re-saturation inside the buffer can be observed up to now – instead, the inner buffer has dried because of evaporation. Since the pore pressure situation will not change, a change in the buffer status cannot be expected in the coming years. Therefore, the experiment partners will have to decide whether to shut down the experiment, and if so, what post-test investigations should be performed with which objectives. This decision needs some preparation and is planned to be taken in 2020.

The FE experiment was constructed in a newly excavated tunnel in an undisturbed part of the Opalinus clay with the original pore pressure field. Due to its realistic scale, however, re-saturation of the buffer is also slow. Pore pressure measurements in the surrounding rock show, depending on the measurement location, the nearly undisturbed pressure far from the experiment tunnel, the moderately affected pressure around the shotcrete-lined tunnel, or the strongly disturbed pressure where steel set support without shotcrete allowed more damage evolution.

Both large-scale experiments need model simulations for their interpretation, and for both of them calculations have already been performed by various groups. What is missing, however, is a realistic simulation taking into account the actual complicated geometry. GRS is approaching this task with the help of Virtus, the virtual underground laboratory. First orientating simulations have been performed, and while numerical challenges exist, further progress is expected. The FE experiment is planned to be simulated in a Decovalex task which GRS will work on.

The DB experiment has provided a large amount of data on the undisturbed Opalinus clay which is useful both in itself and for providing initial and boundary conditions for modelling. Representative petrophysical data for the different facies of the Opalinus clay were collected, and profiles of the temperature and pressure distributions of the whole formation were obtained, supporting and detailing previous assumptions.

Hydro-mechanical behaviour of the Opalinus clay has been investigated in the DM-A, SB, and MB-A experiments. DM-A addresses the long-term deformation behaviour and has shown that pore pressure changes play only a minor role for long-term deformation behaviour. Whether actual creep, i.e. viscous behaviour, is relevant is not clear yet.

MB-A was a mine-by experiment that has delivered a valuable dataset on the hydro-mechanical behaviour of the sandy facies, including data on the evolution of stress, deformation, and pore pressure. For the interpretation of these data, model calculations are necessary again. A respective experiment, modelling of the MB-A, is planned by the MB-A partners to start in 2020.

## **8 Acknowledgements**

The work presented here was funded by the Bundesministerium für Wirtschaft und Energie (BMWi) under contract no. 02E11304. The authors are grateful for the support.

Thanks go to the Mont Terri partners for the very successful and enjoyable cooperation and especially to Swisstopo as the lead organisation of the Mont Terri project.



## References

- /AMB 19/ Amberg (2019): HE-E Experiment: Data Trend Report phase 24 (SSENSORS DATA REPORT No. 20), TN2019-04, Mont Terri Technical Note.
- /BMU 10/ BMU (2010): Safety Requirements Governing the Final Disposal of Heat-Generating Waste. Federal Ministry for the Environment, Nature Conservation, Building and Nuclear Safety, September 30, 2010.
- /BOS 17/ Bossart, P., Bernier, F., Birkholzer, J., Bruggeman, C., Connolli, P., De-wonck, S., Fukaya, M., Herfort, M., Jensen, M., Matray, J-M., Mayor, J. C., Moeri, A., Oyama, T., Schuster, K., Shigeta, N., Vietor, T., & Wieczorek, K. (2017) Mont Terri rock laboratory, 20 years of research: introduction, site characteristics and overview of experiments. Swiss J Geosci (2017) 110:3-22 DOI 10.1007/s00015-016-0236-1.
- /CZA 12/ Czaikowski, O., Garitte, B., Gaus, I., Gens, A., Kuhlmann, U., Wieczorek, K. (2012): Design and predictive modelling of the HE-E test. PEBS Deliverable D3.2-1.  
[http://www.pebs-eu.de/PEBS/EN/Downloads/downloads\\_node\\_en.html](http://www.pebs-eu.de/PEBS/EN/Downloads/downloads_node_en.html)
- /FIR 19/ Firat Lüthi, B. (2019): FE Experiment: Data Trend Report – Data from excavation and during 3 first years of heating (01.01.2012 – 31.12.2018), Technical Note 2018-92, February 2019.
- /GAU 14/ Gaus, I., Garitte, B., Senger, R., Gens, A., Vasconcelos, R., Garcia-Siñeriz, J.-L., Trick, T., Wieczorek, K., Czaikowski, O., Schuster, K., Mayor, J.C., Velasco, M., Kuhlmann, U., Villar, M.V. (2014): The HE-E Experiment: Layout, Interpretation and THM Modelling, Combining D2.2-11 and D3.2-2 of the PEBS Project. Nagra Arbeitsbericht NAB 14-53, Nagra, Wetingen, Switzerland. [www.nagra.ch](http://www.nagra.ch)

- /GID 18/ GiD – The universal, adaptative and user friendly pre and postprocessing system for computer analysis in science and engineering, User Manual, Version 12, 2018.  
[https://www.gidhome.com/archive/GiD\\_Documentation/Docs/GiD12/GiD\\_12\\_User\\_Manual.pdf](https://www.gidhome.com/archive/GiD_Documentation/Docs/GiD12/GiD_12_User_Manual.pdf)
- /HES 16/ Hesser, J. (2016): Personal communication.
- /HES 18/ Hesser, J. (2018): Personal communication.
- /HES 19/ Hesser, J. (2019): Personal communication.
- /HOT 07/ Hoth, P., H. Wirth, K. Reinhold, V. Bräuer, P. Krull, H. Feldrappe: Endlagerung radioaktiver Abfälle in tiefen geologischen Formationen Deutschlands – Untersuchung und Bewertung von Tongesteinsformationen, Bundesanstalt für Geowissenschaften und Rohstoffe, Berlin/Hannover, April 2007.
- /JAE 11/ Jaeggi, David (2011): Long-term reliability, accuracy and power supply, FMGM Berlin, pre-conference workshop “Instrumentation in underground laboratories and geological repositories”. September 12, 2011.
- /KUL 02/ Kull, H., Hartwig, L., Schwarzianeck, P. (2002): Application of GRS-MINIPACKER to determine hydraulic properties of argillaceous formation, Technical Note, Gesellschaft für Anlagen- und Reaktorsicherheit (GRS) mbH, Braunschweig, November 2002.
- /MAY 07/ Mayor, J. C., García-Siñeriz, J. L., Velasco, M., Gómez- Hernández, J., Lloret, A., Matray, J.-M., Coste, F., Giraud, A., Rothfuchs, T., Marshall, P., Roesli, U. & Mayer, G. (2007): Ventilation Experiment in Opalinus Clay for the disposal of radioactive waste in underground repositories. - In: Bossart, P. & Nussbaum, C. (Eds.): Mont Terri Project - Heater Experiment, Engineered Barrier Emplacement and Ventilation Experiment (p.182 - 240). - Rep. Swiss Geol. Surv. 1.

- /MIE 10/ Mieke, R., Czaikowski, O., Wieczorek, K. (2010): BET – Barrier Integrity of the Isolating Rock Zone in Clay Formations, Final Report. GRS-261, Gesellschaft für Anlagen- und Reaktorsicherheit (GRS) mbH, August 2010.
- /MON 20/ <https://www.mont-terri.ch/>
- /MUE 15/ Müller, H.R., Garitte, B., Köhler, S., Vogt, T., Sakaki, T., Weber, H., Vietor, T. (2017): FE/LUCOEX: Final Report, Arbeitsbericht NAB 15-28 National Cooperative for the Disposal of Radioactive Waste.
- /MUE 17/ Müller, H.R., Garitte, B., Vogt, T., Köhler, S., Sakaki, T., Weber, H., Spillmann, T., Hertrich, M., Becker, J., Giroud, N., Cloet, V., Diomidis, N., Vietor, T. (2017): Implementation of the full-scale emplacement (FE) experiment at the Mont Terri rock laboratory. Swiss J Geosci (2017) 110:287-306 DOI 10.1007/s00015-016-0251-2.
- /OEC 01/ OECD-NEA (2001): The role of Underground Laboratories in Nuclear Waste Disposal Programmes. OECD-Nuclear Energy Agency, Paris (2001).
- /OEC 08/ OECD-NEA (2008): Moving Forward with Geological Disposal of Radioactive waste – a collective Statement by the OECD/NEA Radioactive Waste Management Committee (RWMC). NEA No. 6433, Paris (2008).
- /OLI 96/ Olivella, S., Gens, A., Carrera, J., Alonso, E.E. (1996): Numerical Formulation for a Simulator (CODE\_BRIGHT) for the Coupled Analysis of Saline Media. Engineering Computations, 1996, Vol. 13, No 7, pp 87-112.
- /ROT 12/ Rothfuchs, T., Czaikowski, O., Hartwig, L., Hellwald, K., Komischke, M., Mieke, R., Zhang, C.-L. (2012): Self-sealing Barriers of sand/bentonite-mixtures in a clay repository - SB-Experiment in the Mont Terri Rock Laboratory, Final Report, GRS-302, Gesellschaft für Anlagen- und Reaktorsicherheit (GRS) mbH.

- /RUE 14/ Rübel, A. & A. Meleshyn (2014): Methodik und Anwendungsbezug eines Sicherheits- und Nachweiskonzeptes für ein HAW-Endlager im Tonstein – Sicherheitskonzept und Nachweisstrategie. GRS-338, Gesellschaft für Anlagen- und Reaktorsicherheit gGmbH, August 2014.
- /SCH 14/ Schäfers, A., Gaus, I., Johnson, L., Liu, Y., Mayor, J. C., Sellin, P. & Wieczorek, K. (2014). PEBS Final Scientific Report, Deliverable D5-16 of the PEBS project.  
[http://www.pebs-eu.de/PEBS/EN/Downloads/downloads\\_node\\_en.html](http://www.pebs-eu.de/PEBS/EN/Downloads/downloads_node_en.html)
- /TEO 12/ Teodori, S.-P., Gaus, I. (Ed.) (2012): Report of the construction of the HE-E experiment. PEBS Deliverable D2.2-3, 176 pp.  
[http://www.pebs-eu.de/PEBS/EN/Downloads/downloads\\_node\\_en.html](http://www.pebs-eu.de/PEBS/EN/Downloads/downloads_node_en.html)
- /WIE 13/ Wieczorek, K., Miehe, R. (2013): Thermal Characterisation of HE-E Buffer. Deliverable D2.2-9, 41 pp.  
[http://www.pebs-eu.de/PEBS/EN/Downloads/downloads\\_node\\_en.html](http://www.pebs-eu.de/PEBS/EN/Downloads/downloads_node_en.html)
- /WIE 14a/ Wieczorek, K., O. Czaikowski, R. Miehe (2014): Long-Term Performance of Engineered Barrier Systems (PEBS) – GRS Participation, GRS-353, Gesellschaft für Anlagen- und Reaktorsicherheit (GRS) mbH, December 2014.
- /WIE 14b/ Wieczorek, K., Behlau, J., Heemann, U., Masik, S., Müller, C., Raab, M., Kuate Simo, E. (2014): VIRTUS – Virtuelles Untertagelabor im Steinsalz, Abschlussbericht, GRS-354, Gesellschaft für Anlagen- und Reaktorsicherheit (GRS) mbH, Dezember 2014.
- /UPC 11/ Code\_Bright User's Guide, Version 4, Universitat Politècnica de Catalunya - BarcelonaTech, May 2011.
- /VIL 14/ Villar, M. V., Martín, P. L., & Romero, F. J. (2014): Long-term THM test reports: THM cells for the HE-E test: update of results until February 2014. PEBS Deliverable D2.2-7.3, 26 pp.  
[http://www.pebs-eu.de/PEBS/EN/Downloads/downloads\\_node\\_en.html](http://www.pebs-eu.de/PEBS/EN/Downloads/downloads_node_en.html)

- /YUC 15/ Yu, C. (2015): Comparative study of convective and diffusive transport phenomena within the Opalinus Clay of Mont Terri, First Year PhD Progress Report, PRP – DGE/SRTG/2015-00030, Institut de Radioprotection et de Sûreté Nucléaire (IRSN), November 2015.
- /YUC 16/ Yu, C. (2016): Comparative study of convective and diffusive transport phenomena within the Opalinus Clay of Mont Terri, Second Year PhD Progress Report, PRP – DGE/SRTG/2015-00030, Institut de Radioprotection et de Sûreté Nucléaire (IRSN), November 2016.
- /YUC 17/ Yu, C., Matray, J.-M., Gonçalves, J., Jaeggi, D., Gräsle, W., Wieczorek, K., Vogt, T., Sykes, E. (2017): Comparative study of methods to estimate hydraulic parameters in the hydraulic undisturbed Opalinus Clay (Switzerland). *Swiss J Geosci* (2017) 110:85-104 DOI 10.1007/s00015-016-0257-9.
- /ZHA 07/ Zhang, C.-L., Rothfuchs, T., Jockwer, N., Wieczorek, K., Dittrich, J., Müller, J., Hartwig, L., Komischke, M.: Thermal Effects on the Opalinus Clay – A Joint Heating Experiment of ANDRA and GRS at the Mont Terri URL (HE-D Project). Final Report, GRS-224, Gesellschaft für Anlagen- und Reaktorsicherheit (GRS) mbH, Braunschweig, March 2007.
- /ZHA 14/ Zhang, C.-L., Czaikowski, O., Komischke, M., Wieczorek, K. (2014): Thermo-Hydro-Mechanical Processes in the Nearfield around a HLW Repository in Argillaceous Formations – Volume II: In-situ-Investigations and Interpretative Modelling, May 2007 to May 2013, GRS-313, Gesellschaft für Anlagen- und Reaktorsicherheit (GRS) mbH, June 2014.
- /ZHA 19/ Zhang, C.-L., Komischke, M., Kröhn, M., Rogalski, A., Zehle, B. (2019): Experimental Study of the Mechanical Behaviour of the Sandy Facies of Opalinus Clay at Mont Terri – LT-A Programme within the Mont Terri Project, GRS-555, Gesellschaft für Anlagen- und Reaktorsicherheit (GRS) mbH, December 2019.



## List of figures

Fig. 2.1	The Swiss repository concept for clay rock /JAE 11/.....	3
Fig. 2.2	Processes in a repository in clay (red: thermal, blue: hydraulic, grey: mechanical, yellow: chemical/biological). DB, HE-E, DM-A, FE: selected Mont Terri experiments addressing different processes.....	4
Fig. 3.1	The Mont Terri Rock Laboratory in the Swiss Jura.....	7
Fig. 3.2	The MTRL tunnel system. Different colours of the tunnel system mark the respective year of excavation.....	8
Fig. 3.3	Plan view of the Mont Terri rock laboratory showing the geology (green: recently excavated lab extension with the locations of new experiments).....	8
Fig. 3.4	Geological section along the Mont Terri motorway tunnel showing the location of the rock laboratory (DB borehole: see Section 5.2.5).....	9
Fig. 4.1	Experiment locations HE-E, FE-M, DM-A, SB-A, DB, and MB-A.....	11
Fig. 5.1	GRS minipiezometer – photo (left) and sketch (right).....	14
Fig. 5.2	Coaxial tubing (left) and transducer rack (right) .....	14
Fig. 5.3	Overview of the HE-E experiment layout /TEO 12/ .....	17
Fig. 5.4	Longitudinal section of the microtunnel showing the instrumentation cross sections /GAU 14/. Sections SA, SB, SD denote rock instrumentation, sections N1–N3 and G1–G3 denote buffer instrumentation .....	18
Fig. 5.5	Integrated buffer installation and instrumentation. Left: design of a buffer instrumentation module, right: complete bentonite block/liner/sensor carrier module before insertion into the microtunnel /GAU 14/.....	19

Fig. 5.6	Position of sensors in the buffer and on the microtunnel wall /GAU 14/ ...	19
Fig. 5.7	Left: Granular buffer emplacement using an auger system, right: 3D image of the microtunnel test section before installation for volume calculation /GAU 14/ .....	20
Fig. 5.8	Heater liner temperature in the central part of the sand-bentonite section. Red: top of liner, blue: bottom of liner /AMB 19/ .....	22
Fig. 5.9	Heater liner temperature in the central part of the bentonite section. Red: top of liner, blue: bottom of liner /AMB 19/ .....	23
Fig. 5.10	Temperature evolution at selected points in the central part of the sand-bentonite section.....	24
Fig. 5.11	Temperature evolution at selected points in the central part of the pure bentonite section.....	24
Fig. 5.12	Relative humidity evolution at selected points in the central part of the sand-bentonite section.....	25
Fig. 5.13	Relative humidity evolution at selected points in the central part of the pure bentonite section .....	26
Fig. 5.14	General experiment layout of the Full-scale Emplacement (FE) experiment at MTRL; sensors and granular backfill are not displayed /MUE 15/ .....	27
Fig. 5.15	Sketch of the FE monitoring boreholes (red lines). GRS minipiezometers are located around the plug (blue area on the left) and at the tunnel rear end (blue area on the right) .....	28
Fig. 5.16	Drilling of the minipiezometer boreholes: tunnel front (left), radial borehole at the tunnel rear (right).....	29
Fig. 5.17	Installation of the transducer racks in the rear part of the tunnel .....	29
Fig. 5.18	Location of minipiezometers 6 m from the tunnel front.....	29

Fig. 5.19	Location of minipiezometers close to the rear part of the tunnel.....	30
Fig. 5.20	Sketch of the emplacement and backfilling sequence in the FE tunnel at Mont Terri /MUE 15/.....	30
Fig. 5.21	FE central heater temperature evolution at different locations on the container /FIR 19/ .....	31
Fig. 5.22	Temperature measured at the minipiezometers located 6 m from the tunnel front.....	32
Fig. 5.23	Pore-water pressure measured at the minipiezometers located 6 m from the tunnel front.....	32
Fig. 5.24	Temperature measured at the minipiezometers located in the rear part of the tunnel.....	33
Fig. 5.25	Pore-water pressure measured at the minipiezometers located in the rear part of the tunnel (BFEB048: scale on the right) .....	34
Fig. 5.26	Dilatometer probe for borehole deformation monitoring (sensor 1 – 3: temperature/relative humidity sensors) .....	35
Fig. 5.27	Deformation sensor readings of the dilatometer probe.....	36
Fig. 5.28	Air and rock temperature measured in the SB niche, about 20 m from the dilatometer borehole .....	37
Fig. 5.29	Location of minipiezometer boreholes near the dilatometer probe .....	38
Fig. 5.30	Measured pore-water pressure at the minipiezometers in the vicinity of the dilatometer probe.....	38
Fig. 5.31	SB-A experiment location and boreholes /HES 16/ .....	40
Fig. 5.32	Location of minipiezometer boreholes (SB-A6 and SB-A7) in relation to the experiment borehole SB-A3 (left), piezometer borehole drilling (right).....	41

Fig. 5.33	Pore-water pressure measured at minipiezometers SB-A6 and SB-A7....	41
Fig. 5.34	Geological cross section of the Mont Terri anticline, showing the location of the MTRL (white line) and of the borehole BDB-1 (heavy black line), crossing the lower part of the Dogger aquifer, the entire Opalinus clay formation and the upper part of the Liassic marls /YUC 17/.....	42
Fig. 5.35	Drilling of the 250-m-borehole BDB-1 .....	43
Fig. 5.36	a) Stratigraphic sequence along the BDB-1 borehole, b) borehole configuration with packer intervals, c) packer interval detail /YUC 17/.....	44
Fig. 5.37	DB first year monitoring results: temperature /YUC 15/.....	45
Fig. 5.38	DB first year monitoring results: pore-water pressure /YUC 15/ .....	45
Fig. 5.39	Depth profiles of temperature (left) and pore pressure (right) /YUC 15/ ...	46
Fig. 5.40	Profiles of petrophysical parameters (water loss porosity, degree of saturation, dry mass based water content, bulk density, specific surface area, grain density), determined on BDB-1 core samples /YUC 15/.....	47
Fig. 5.41	Sketch of the MB-A experiment area. Excavation stopped at the red dashed line, and instrumentation boreholes were drilled from the two niches CS-D and SW.....	48
Fig. 5.42	Plan view of the MB-A experiment area with the instrumentation boreholes /HES 18/.....	49
Fig. 5.43	First measurement data of the original set of piezometers .....	50
Fig. 5.44	Original and replacement piezometer boreholes – front view /HES 19/....	51
Fig. 5.45	Original and replacement piezometer boreholes – plan view /HES 19/ ....	51
Fig. 5.46	Original and replacement piezometer boreholes – side view /HES 19/ ....	52

Fig. 5.47	Pore pressure evolution as measured by the MB-A minipiezometers. Grey step curve: distance of excavation front from the niches (right scale).....	54
Fig. 5.48	Pore pressure evolution as measured by BMB-A14, BMB-A15, and BMB-A24. Grey step curve: distance of excavation front from the niches (right scale).....	54
Fig. 5.49	Cutting through of Gallery 18, May 27, 2019.....	55
Fig. 6.1	Geometrical structure of the MTRL (Virtus representation) .....	58
Fig. 6.2	Simplified Mont Terri geology of Virtus (yellow: OPA shaly facies, brown: OPA sandy facies, green: Lias marl/limestone, blue: Dogger limestone).....	59
Fig. 6.3	Geology mapped on the laboratory structure .....	59
Fig. 6.4	Combined model of laboratory structure and geologic interfaces .....	60
Fig. 6.5	View into the Virtus representation of the MTRL .....	60
Fig. 6.6	Definition of a brick-shaped section in Virtus for the export (left) and meshing of the section imported by GiD (right) for the example of HE-E..	61
Fig. 6.7	Geometrical model of the HE-E TH simulation.....	63
Fig. 6.8	HE-E heater details as included in the HE-E model .....	63
Fig. 6.9	Liner temperature measured at the centre top and bottom of the heater (red and blue curves) and calculated liner temperature during heating phase 3 (surface plot) .....	69
Fig. 6.10	Temperature measured in the granular sand-bentonite buffer (symbols) and corresponding calculated temperatures (continuous lines: 2D plane strain TH simulation, dotted lines: 3D pure thermal simulation, purple line: 3D coupled TH simulation result).....	70

Fig. 6.11	Simulation results for saturation evolution in the centre of the granular bentonite buffer and the sand-bentonite buffer.....	71
Fig. 6.12	Geometrical model of the FE-M (complete mesh) .....	72
Fig. 6.13	Geometrical model of the FE-M: Detail showing the FE cavern, FE tunnel, and heated containers on bentonite blocks .....	72
Fig. 6.14	Simulated temperature distributions near the containers and in the tunnel floor after 10 years of heating.....	73

## List of tables

Tab. 6.1	Material data of Opalinus clay and buffer materials.....	66
Tab. 6.2	Material data of technical components.....	66
Tab. 6.3	Schedule and conditions of the HE-E coupled TH simulation.....	68

**Gesellschaft für Anlagen-  
und Reaktorsicherheit  
(GRS) gGmbH**

Schwertnergasse 1  
**50667 Köln**  
Telefon +49 221 2068-0  
Telefax +49 221 2068-888

Boltzmannstraße 14  
**85748 Garching b. München**  
Telefon +49 89 32004-0  
Telefax +49 89 32004-300

Kurfürstendamm 200  
**10719 Berlin**  
Telefon +49 30 88589-0  
Telefax +49 30 88589-111

Theodor-Heuss-Straße 4  
**38122 Braunschweig**  
Telefon +49 531 8012-0  
Telefax +49 531 8012-200

[www.grs.de](http://www.grs.de)